Fall 2019

Development of A Robotized Laser Directed Energy Deposition System and Process Challenges

Meysam Akbari
Southern Methodist University, makbari@smu.edu

DEVELOPMENT OF A ROBOTIZED LASER DIRECTED ENERGY DEPOSITION SYSTEM AND PROCESS CHALLENGES

Approved by:

_____
Dr. Radovan Kovacevic

_____
Dr. Xin-lin Gao

_____
Dr. Wei Tong

_____
Dr. Xu Nie

_____
Dr. Fanrong Kong

DEVELOPMENT OF A ROBOTIZED LASER DIRECTED ENERGY DEPOSITION SYSTEM AND PROCESS CHALLENGES

A Dissertation Presented to the Graduate Faculty of

Bobby B. Lyle School of Engineering

Southern Methodist University

in

Partial Fulfillment of the Requirements

for the degree of

Doctor of Philosophy

with a

Major in Mechanical Engineering

by

Meysam Akbari

(B.S., Amirkabir University of Technology, Iran, 2006)

(M.S., Amirkabir University of Technology, Iran, 2009)

Dec 21, 2019

ACKNOWLEDGMENTS

I would like to express my sincere gratitude to my advisor, Professor Radovan Kovacevic, whose support and advice were invaluable throughout my PhD program. This work could not have been accomplished without his wisdom and precious guidance.

Thanks to my committee members, Dr. Xin-lin Gao, Dr. Wei Tong, Dr. Xu Nie, and Dr. Fanrong Kong for their time spent on reviewing my dissertation and providing insightful comments.

I would also like to thank Mr. Andrew Socha, research engineer at RCAM, for his assistance in conducting the experiments. Many thanks go to my colleagues in RCAM, Yaoyu Ding, Zhe Zhang, Nima Yazdian, Guang Yang, Ehsan Dezhparvarderakhshan, Masoud Mohammadpour, and Yang Baixuan for their useful suggestions and comments on my research projects.

Finally, I am very grateful to my family for their support and unyielding love.

DEDICATION

I WOULD LIKE TO DEDICATE THIS THESIS TO MY LOVELY WIFE (FARNAZ NOURBAKHSH), MY FATHER (AMIRHOSSEIN AKBARI) AND MY MOTHER (AKRAM MOUSAVI) FOR THEIR UNCONDITIONAL AND ENDLESS LOVE, SUPPORT AND ENCOURAGEMENT.

Akbari, Meysam B.S., Amirkabir University of Technology, Iran, 2006
M.S., Amirkabir University of Technology, Iran, 2009

Development of a robotized laser directed energy

deposition system and process challenges

Advisor: Professor Radovan Kovacevic

Doctor of Philosophy conferred Dec 21, 2019

Dissertation completed Sep 24, 2019

Metal additive manufacturing (AM) is a disruptive technology, enabling fabrication of complex and near net shaped parts by adding material in a layer-wise fashion. It offers reduced lead production time, decreased buy-to-fly ratio, and repair and remanufacturing of high value components. AM processes are finding applications in many industrial sectors such as aerospace, automotive, biomedical and mold tooling. However, beside tremendous advantages of AM, there are still some challenges that prevent the adoption of this technology into high standard applications. Anisotropy and inhomogeneity in mechanical properties of the as-built parts and existence of pores and lack-of-fusion defects are considered as the main issues in directed energy deposition (DED) parts. Process planning and the utilization of methods that can increase the flexibility of design of DED parts with overhang sections is also of great importance. A robotized laser powder and/or wire directed energy deposition system has been developed at Research Center for Advanced Manufacturing (RCAM) at Southern Methodist University (SMU) in order to address the mentioned issue and eventually to make the robotized DED process more practical for abroad range of industrial applications.

The mechanical and microstructural properties of 316LSi parts were studied. In this regard, two types of coupons, thin-walled and block, of short and long inter-layer time intervals were considered. It was found that different thermal histories caused by different inter-layer time intervals have significant impact on mechanical and microstructural properties. The thin-walled samples with lower cooling rates showed coarser columnar grains, lower ultimate tensile strength, and lower hardness compared to the block samples. The melt pool was monitored in real-time. An empirical correlation between the melt pool area and cooling rate was achieved that could enable control of scale of the final solidification structure by maintaining the melt pool size in real-time. Further, to study the anisotropic behavior, tensile samples were loaded in parallel and perpendicular directions with respect to the deposition direction. The results indicated that samples in the perpendicular direction had lower UTS and elongation for both coupon types, revealing a weaker bonding at inter-layer/bead interface due to the existence of lack-of-fusion pores.

As mentioned earlier, the robotized laser wire directed energy deposition (RLW-DED) has limitations in printing certain complex shape parts. Fabricating parts with overhang sections, depending on the geometry, might cause a collision between the laser head and the buildup. Part segmentation and joining the elements back together has been presented to overcome those limitation. In this study, the welding of additively-manufactured parts by RLW-DED has been proposed. Autogenous laser welding, performed at the same setup used for RLW-DED, was utilized to join the thin-walled 316LSi DED parts. Mechanical and microstructural testing were then performed on the welded samples. The results showed that the mechanical properties of welded DED parts are comparable with those of DED parts. Furthermore, a component of complex shape was

fabricated to show the capability of the developed process. Therefore, the welding of RLW-DED parts can expand the application of 3D-printed parts in industry.

Robotized laser powder directed energy deposition is a non-linear process, and the dynamic response of the system varies layer by layer. An adaptable PI-controller with layer-dependent control gains was developed to ensure a constant melt pool width through the entire build. The laser power was selected as the control output variable, and the melt pool width was chosen as the control input variable. The performance of the controller was evaluated through deposition of thin wall samples. The results showed that the controller, by adjusting the laser power in real time, could successfully maintain the melt pool width and produce a more uniform and finer microstructure as compared to the sample with a constant laser power.

Keywords: additive manufacturing; robotized laser directed energy deposition; microstructural and mechanical properties; closed loop control; melt pool monitoring; joining; welding

Table of Contents

1.INTRODUCTION 1

1.1 Metal additive manufacturing 1

1.2 Laser directed energy deposition (Laser DED) 5

1.3 Challenges in laser DED process 9

1.3.1 Microstructural and mechanical properties 9

1.3.2 Process monitoring and control 15

1.3.3 Process path planning 15

1.4 Research objectives 16

REFERENCES 17

2.AN INVESTIGATION ON MECHANICAL AND MICROSTRUCTURAL PROPERTIES OF 316LSI PARTS FABRICATED BY A ROBOTIZED LASER/WIRE DIRECT METAL DEPOSITION SYSTEM 24

2.1 Introduction 24

2.2 Experimental procedure 29

2.2.1 Materials 29

2.2.2 System overview and procedure 29

2.3 Experimental results and discussion 35

2.3.1 Microstructural analysis 35
2.3.2 Tensile properties 45
2.3.3 Microstructure-tensile properties relation 50
2.3.4 Microhardness 51
2.3.5 Porosity 53
2.4 Conclusions 55
REFERENCES 57
3.JOINING OF ELEMENTS FABRICATED BY A ROBOTIZED LASER/WIRE DIRECTED ENERGY DEPOSITION PROCESS BY USING AN AUTOGENOUS LASER WELDING 65
3.1 Introduction 65
3.2 Experimental procedure 68
3.2.1 Materials 68
3.2.2 Methodology 68
3.3 Experimental results and discussion 74
3.3.1 Microstructural analysis 74
3.3.2 Tensile properties 77
3.3.3 Microhardness 80
3.3.4 Porosity 81
3.4 A case of fabricating a part with overhang surface 82

3.5 Conclusions 84

REFERENCES 86

4.CLOSED LOOP CONTROL OF MELT POOL WIDTH IN ROBOTIZED LASER POWDER DIRECTED ENERGY DEPOSITION PROCESS 90

4.1 Introduction 90

4.2 Experimental procedure 93

4.3 Closed loop control system 96

4.3.1 Image acquisition and processing 96

4.3.2 System identification 98

4.3.3 Controller design 101

4.4 Experimental results and discussion 104

4.4.1 Performance verification of controller 104

4.4.2 Deposition of thin wall structures with and without control 105

4.4.3 Microstructural analysis 108

4.5 Conclusions 114

REFERENCES 115

5.SUMMARY AND FUTURE WORK 119

5.1 Summary 119

5.2 Future work 122

5.3 Publications 123

LIST OF FIGURES

Figure 1.1 Metal AM classification [2]..... 2

Figure 1.2 Schematic illustration of (a) PBF [4] (b) wire-fed DED and (c) powder-fed DED [5]..... 3

Figure 1.3 Metal 3D printed components. (a) Gas turbine blade built by PBF system [7] (b) A metamaterial structure with negative Poisson's ratio printed by robotized DED system at RCAM [8]. (c) A ship propeller with 1.35 m diameter fabricated by wire arc additive manufacturing [9]..... 5

Figure 1.4 A four-nozzle powder delivery system [11]..... 6

Figure 1.5 Wire feeding setup (a) wire tip with respect to melt pool and nozzle (b) wire feeding directions [15]..... 8

Figure 1.6 Different transfer mode between wire and melt pool (a) droplet-like mode (b) smooth (c) smooth plunging (d) damaged bead due to high wire feed-rate [15]..... 9

Figure 1.7 3D composite view showing the cellular morphologies of samples with condition of (a) small-size LCD (b) meddle-size LCD and (c) large-size LCD [30]..... 11

Figure 1.8 Effect of specific energy (E) on (a) tensile properties (b) microhardness of 316L as-deposited samples [30]..... 11

Figure 1.9 Schematic of fabricated cylindrical rods (a) one cylindrical rod built at a time, i.e. single-built, and (b) nine samples built at a time, i.e. nine-built [32]..... 12

Figure 1.10 EBSD inverse pole map for (a) single-built (c) nine-built. Misorientation angle distribution of austenite phase for (b) single-built (d) nine-built (red: [001]; blue:[111]; green:[101]) [32]. 13

Figure 1.11 (a) optical micrograph (b) schematic showing the equiaxed-to-columnar transition in Ti-6Al-4V alloy due to fast heat sink in initial layers [36]..... 14

Figure 2.1 (a) A robotized laser/wire direct metal deposition system; (b)-(e) photographs of a few as-built parts fabricated by this system. 31

Figure 2.2 Photographs of the as-built 316LSi coupons along with their dimensions. (a) Block coupon; (b) thin-walled coupon. 34

Figure 2.3 Thin-walled coupon. (a) Real-time isotherm images of melt pool in different layers along with melt pool boundary; (b) and (e) micrographs of the top and bottom layers in low magnification; (c),(d),(f) and (g) higher magnifications of microstructure showing the elongated columnar grains; (h) SEM image indicating the dendritic structure along with EDS measured points. 35

Figure 2.4 Block coupon. (a) Real-time isotherm images of melt pool in different layers along with melt pool boundary; (b) and (e) micrographs of the top and bottom layers in low magnification; (c),(d),(f) and (g) higher magnification of microstructure showing the elongated columnar grains; (h) SEM image indicating the dendritic structure along with EDS measured points. 36

Figure 2.5 Solidification map showing the effect of temperature gradient G and growth rate R on morphology and size of the solidification microstructure [31]. 38

Figure 2.6 Captured top-view images of melt pool under the same scanning condition. (a) Original infrared image; (b) ordinary image; (c) binary image showing the boundary of melt pool. 41

Figure 2.7 Variation of melt pool size as a function of number of layers. (a) thin-walled coupon; (b) block coupon. 42

Figure 2.8 The variations of cooling rate vs melt pool area during the process; (b) PDAS as a function of number of layers..... 42

Figure 2.9 EDS spectrum. (a) First point in Fig. 3(h); and (b) the variation of main elements of all spots. 44

Figure 2.10 X-ray diffraction patterns of the as-built 316LSi parts. (a) Thin-walled coupon; (b) block coupon. 45

Figure 2.11 (a) Stress-strain curves of SS316LSi specimens fabricated by laser wire direct metal deposition; (b) configuration of tensile samples showing their orientations; (c) standard ASTM E8 tensile sample; (d) broken tensile specimens after testing. 46

Figure 2.12 Tensile fracture surfaces. (a) in high magnification show ductile fracture mode with dimples for thin-walled; (b) in high magnification show ductile fracture mode with dimples for block; (c) and existence of inter-layer pores caused by lack-of-fusion for specimen in the perpendicular directionfrom block coupon. 50

Figure 2.13 (a) Hardness distribution along height direction for both thin-walled and block samples; (b) optical micrograph of block sample showing the location of some of indentations. 53

Figure 2.14 SEM micrographs showing porosity distribution across the coupons. (a) Top and (b) lower part of the block coupon; (c) top; (d) middle and (e) lower part of the thin-walled coupon. 55

Figure 3.1 A robotized laser/wire directed energy deposition system used for DED and welding processes. 69

Figure 3.2 (a) As-built coupon used for welding (b) Weld DED-P sample: tensile specimens parallel to the deposition direction (c) Weld DED-N sample: tensile specimens normal to the deposition direction (d and e) welded DED parts..... 72

Figure 3.3 (a) As-built coupon for preparing tensile specimens without weld (b) orientation of tensile specimens in the normal direction (DED-N) (c) orientation of tensile specimens in the parallel direction (DED-P) (d) the dimensions of the standard tensile specimen per ASTM E8 [17]. 72

Figure 3.4 The transverse-section images of Weld DED-N sample (a) optical micrograph showing the weld zone and DED plates (b) distribution of grains around weld centerline (c) fusion boundary (d) DED microstructure (e) SEM image of the weld zone indicating the columnar dendrites (f) SEM image of the DED indicating the columnar dendrites... 75

Figure 3.5 The transverse-section optical images of Weld DED-P sample (a) optical micrograph showing the weld zone and DED plates (b) SEM image of the weld zone indicating the columnar dendrites (c) fusion boundary. 76

Figure 3.6 EDS line profiles of Cr and Ni elements across the phase boundaries for (a) Weld DED-N and (b) Weld DED-P coupons. The scanning lines are shown in Fig. 4(e) and 5(b). 77

Figure 3.7 Tensile test results for DED and welded DED specimens (a) typical stress-strain curves of different specimens along with broken tensile specimens (b) the average UTS and elongation values of all tested specimens. 79

Figure 3.8 Typical tensile fracture surfaces (a) Weld DED-N specimen (b) Weld DED-P specimen (c and d) dimples in the fracture surfaces showing the ductile fracture. 80

Figure 3.9 Microhardness profiles along the cross-sections of the joints. 81

Figure 3.10 Porosity obsereved in (a) Weld DED-N and (b) Weld DED-P coupons. 82

Figure 3.11 (a) A part with overhang sections (b) illustration of kinematic system when the lower cone was printed (c) the occurrence of collision between laser head and lower cone at the instance when the upper cone started to be printed. 83

Figure 3.12 (a and b) The lower and upper cones fabricated by RLW-DED (c) the final part after autogenous laser welding of two cones (d) the cross-section of the joint. 84

Figure 4.1 Schematic overview of robotized laser powder directed energy deposition equipped with closed loop control system. 94

Figure 4.2 Image processing steps to obtain the melt pool width (see text for details). ... 97

Figure 4.3 The results of step response tests in different layers of a thin wall deposition. 99

Figure 4.4 Schematic illustration of parameters for first order transfer function. 100

Figure 4.5 The block diagram of the closed loop control system used for RLP-DED process..... 101

Figure 4.6 Response of the closed loop system to disturbances. 105

Figure 4.7 The deposited samples along with their micrographs. (a) Sample with constant laser power (b) Sample with controlled laser power. 106

Figure 4.8 Melt pool width as a function of layer numbers for the sample with constant laser power. 107

Figure 4.9 (a) The variation of melt pol width and (b) laser power for the controlled sample. 108

Figure 4.10 Microstructure of 316L sample with constant laser power (a) low magnification of micrograph at middle of sample (b) typical fine cellular structure at bottom layers (c) cellular and columnar morphology at middle and (d) columnar dendritic structure at top layers. 109

Figure 4.11 Microstructure of 316L sample with controlled laser power (a) low magnification of micrograph at middle of sample. Cellular structures at (b) bottom layers (c) middle and (d) top layers. The method of grain size measurement is shown in (c) .. 110

Figure 4.12 Solidification map showing the effect of temperature gradient, G, and growth rate, R, on the morphology and size of solidification microstructure [22]. 111

Figure 4.13 The variations in (a) grain size and (b) cooling rate as a function of layer number 113

LIST OF TABLES

Table 1.1 Comparison of two categories of metal AM processes: DED and PBF [6] 4

Table 1.2 Process parameters and experimental design level used for experimentations [30]. 10

Table 2.1 Chemical compositions of wire and substrate. 29

Table 2.2 Optimized process parameters used for fabricating samples. 32

Table 2.3 Mechanical tensile test results for as-built SS316LSi parts by LW-DMD, wrought material [38] and L-DMD parts [39]. 47

Table 3.1 Chemical compositions of wire and substrate. 68

Table 3.2 Processing parameters for DED and welding. 73

Table 3.3 EDS chemical composition of different points across the weld zone and DED parts. 77

Table 4.1 Process parameters used in this study 95

Table 4.2 Chemical composition of powder and substrate 95

Table 4.3 Transfer function parameters and controller gains for different layers 103

Chapter 1

INTRODUCTION

1.1 Metal additive manufacturing

Metal additive manufacturing (AM) or commonly known as metal 3D printing, is a technique of building parts by progressively adding thin layers of material. This technology has disrupted the manufacturing industry in recent years and has successfully attracted the researchers where it can offer the fabrication of freeform and complex components directly from 3D digital CAD file, reduction in production time and eliminating the need for tooling and fixturing. According to American Society for Testing and Materials (ASTM) International Committee F42 on AM technologies, the metal AM processes are classified into three categories, namely, directed energy deposition (DED), powder bed fusion (PBF), and sheet lamination (SL) [1]. Fig. 1.1 shows the summary of most common AM methods.

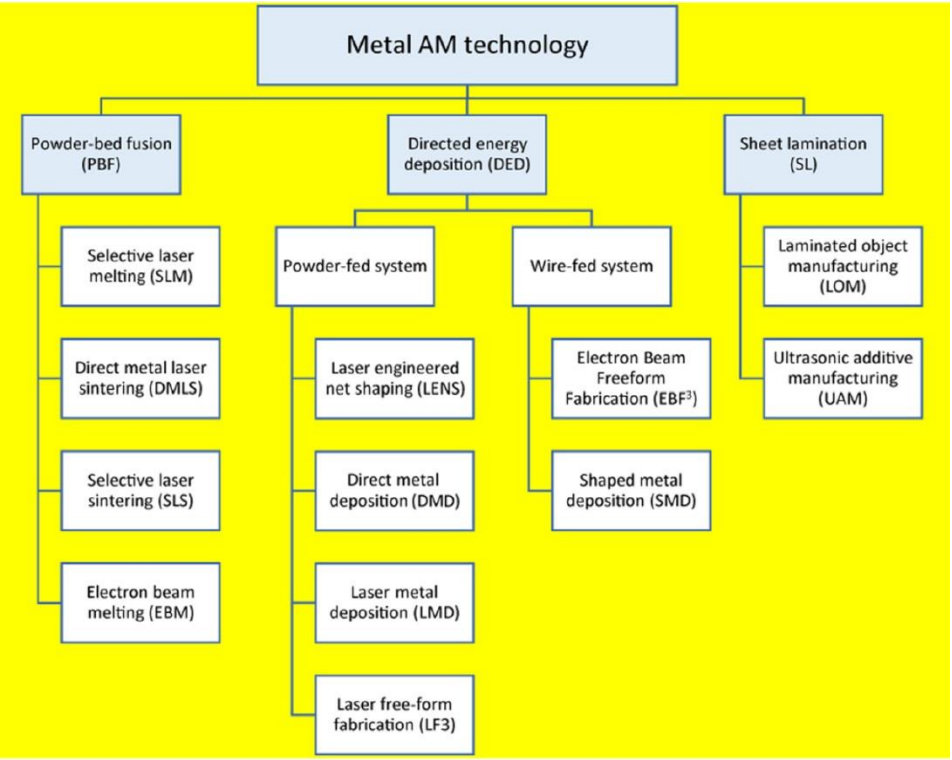

Figure 1.1 Metal AM classification [2].

Fig. 1.2 illustrates schematically a PBF system, a DED system based on powder feedstock and a DED system based on wire feedstock, respectively. In PBF process, a laser or electron beam is delivered to a bed of powder where metallic powders are sintered or melted selectively [3]. First, a layer of powders is distributed uniformly by a roller and then melted by a high density energy beam such as laser or electron beam. After a layer is finished, the build platform is lowered down and this cycle repeats until the entire component is fabricated.

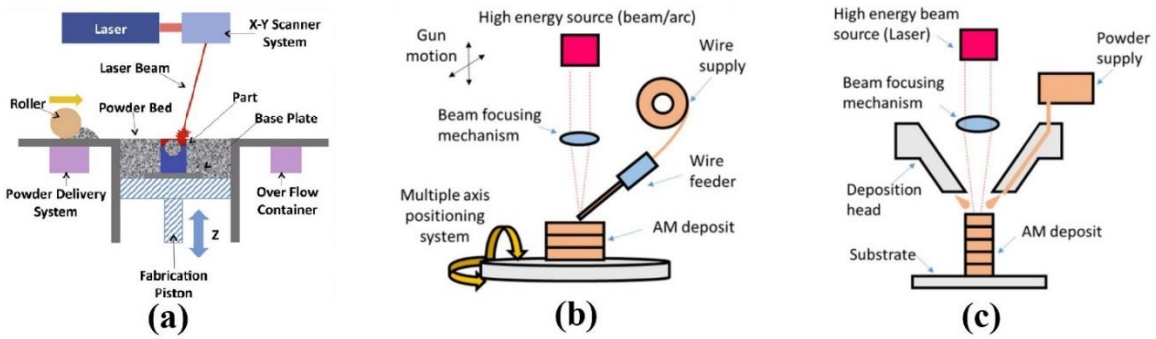

Figure 1.2 Schematic illustration of (a) PBF [4] (b) wire-fed DED and (c) powder-fed DED [5].

Table 1.1 compares the DED and PBF processes in terms of their specifications. Each of these processes has their own advantages and drawbacks and their selection depends on the specific applications. For instance, PBF process is capable of printing intricate geometries and features with small resolutions. In contrast, DED is less flexible to fabrication of highly complex parts, however it can offer larger build size, higher deposition rate, ability to make functionally graded composition materials, repair worn out and damaged high value components, and print lattice structures with auxetic behaviors.

Table 1.1 Comparison of two categories of metal AM processes: DED and PBF [6]

Process	**DED**			**PBF**	
Feedstock	**Powder**	**Wire**		**Powder**	
Heat source	Laser	E-beam	Electric arc	Laser	E-beam
Nomenclature	DED-L	DED-EB	DED-PA/DED-GMA	PBF-L	PBF-EB
Power (W)	100-3000	500-2000		50-1000	
Speed (mm/s)	5-20	1-10	1000-3000	10-1000	
Max. feed rate (g/s)	0.1-1.0	0.1-2.0	5-15	0.2-2.8	
Max. build size (mm x mm x mm)	2000x1500x750	2000x1500x750	5000x3000x1000	500x280x320	
Production time	High	Medium	Low	High	
Dimensional accuracy (mm)	0.5-1.0	1.0-1.5	Intricate features are not possible	0.04-0.2	
Surface roughness	4-10 μm	8-15 μm	Needs machining	7-20 μm	
Post processing	HIP and surface grinding are seldom required	Surface grinding and machining is required to achieve better finish	Machining is essential to produce final parts	HIP is rarely required to reduce porosity	

Fig. 1.3 depicts a few components built by different metal AM processes, showing the capability of each process.

Figure 1.3 Metal 3D printed components. (a) Gas turbine blade built by PBF system [7] (b) A metamaterial structure with negative Poisson's ratio printed by robotized DED system at RCAM [8]. (c) A ship propeller with 1.35 m diameter fabricated by wire arc additive manufacturing [9].

1.2 Laser directed energy deposition (Laser DED)

DED is defined as "an additive manufacturing process in which focused thermal energy is used to fuse materials by melting as they are being deposited" according to ISO/ASTM 52900:2015 [10]. DED has been recognized with different terminologies in literature such as Laser Engineered Net Shaping (LENS®), laser metal deposition (LMD), direct metal deposition (DMD), and shaped metal deposition (SMD). A DED system can be further categorized based on the feedstock material, namely, wire-fed DED (Fig. 1.2(b)) and powder-fed DED (Fig. 1.2(c)).

In metal deposition process, a heat source is used to melt the material. Different types of heat sources have been utilized in DED processes, including laser, electron beam, and arc. Among these heat sources, laser beam has been extensively applied because: it shows more flexibility in focusing on small or large areas, it has high energy density and

low heat input that leads to a small heat affected zone and also because the laser power is easy to control.

In laser DED, the material in the form of powder or wire is fed into the melt pool. The powder is usually blown coaxially from either a conical nozzle or a multi-nozzle powder delivery system into the processing zone. Fig. 1.4 illustrates a typical four-nozzle powder delivery system. In laser DED based on wire feeding, the wire metal is usually fed from one side (mostly from leading edge of melt pool). With the advancement of this technology, a few companies such as Fraunhofer and Precitec developed the new laser heads that are capable of feeding wire from center that is being exposed to the coaxially split laser beams.

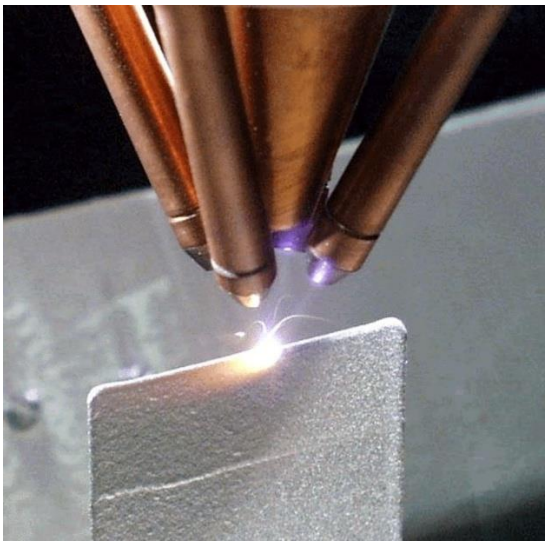

Figure 1.4 A four-nozzle powder delivery system [11].

Laser wire DED offers several advantages over powder based DED system: material usage is almost 100%, it is cleaner and it can achieve higher deposition rates, and it is a lower cost process since the wire feedstock is cheaper than metal powder. The laser DED process is influenced by several processing variables such as laser power, laser beam

size, travel speed, material delivery method and material feed-rate, shielding gas and material properties (e.g. thermal conductivity, absorptivity). Among all these factors, the laser power, travel speed and material feed-rate have been researched mostly in literature. In laser powder DED, as the laser power increases the powder capture efficiency increases and thereby the track width will be increased [12]. Therefore, the laser power is the main adjusting factor when the track width is used as control variable in closed loop control system. In laser wire DED, laser power plays a similar role; the melt pool width becomes larger as the laser power increases [13]. Travel speed has direct impact on the track height. The track height is decreased when the travel speed is increased [12]. The material feed-rate (wire or powder) also influences the track height such that by increasing the material feed-rate the height of the bead becomes larger [14].

As mentioned earlier, laser wire DED has some unique advantages. However, there exists some process-related factors that affect the quality of deposition and stability of the process. Wire feeding direction, feeding angle, wire tip position, and wire stick-out from the wire feeding nozzle are the variables that must be tuned accurately before the process starts [15]. These parameters are shown schematically in Fig. 1.5.

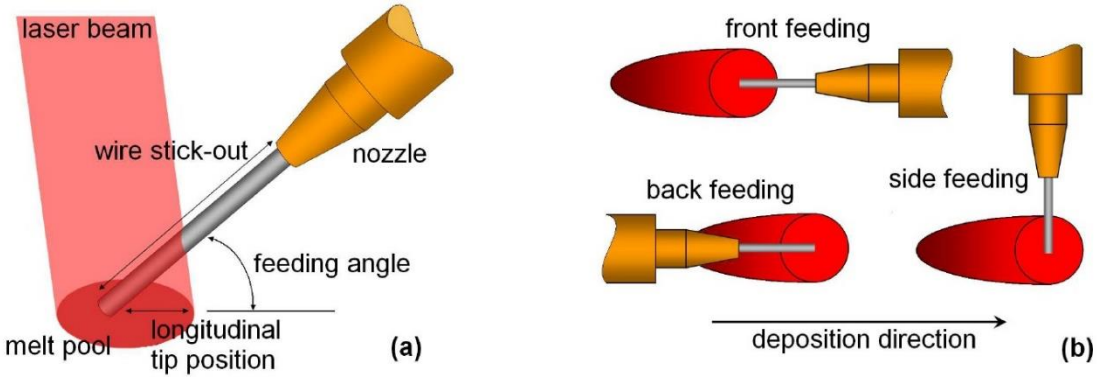

Figure 1.5 Wire feeding setup (a) wire tip with respect to melt pool and nozzle (b) wire feeding directions [15].

It was verified by Mok et al. [16] that front wire feeding with 45° angle is the best orientation that could achieve the maximum deposition rate. Syed et al. [17] revealed that the best quality of beads was achieved when the wire was placed at the leading edge of the melt pool with the angle of 20°-60°. Based on the wire setup parameters (see Fig. 1.5), there are three modes of metal transfer: droplet-like transfer, smooth transfer, and plunging [15] as depicted in Fig. 1.6. Droplet is usually formed when the wire tip is exposed to laser beam for longer time (e.g. when the distance between wire tip and substrate is large). Therefore, the temperature at wire tip exceed the melting point and droplet starts to form. Ultimately, the droplet will be detached from wire due to gravitational force, leading to an irregular bead shape (Fig. 1.6 (a)). In contrast, if wire feeder is appropriately set up so that the wire is melted "close to the intersection with melt pool" [15], the resulting beads will have smooth surface and good metallurgical bonding. In plunging mode, the wire is not melted by laser power and instead, it is melted by the heat conduction from the melt pool (see Fig. 1.6 (c)). However, this mode is very sensitive to the wire feeding rate. High wire feeding rates could cause the lack of energy to the melt pool (wire is partially melted by the high

temperature of melt pool), resulting in lack-of-fusion defects [15]. Fig. 1.6 (d) shows the damaged deposition due to high wire feed rate.

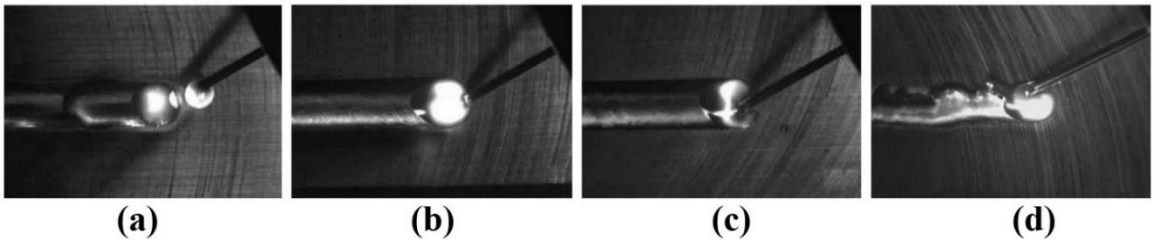

Figure 1.6 Different transfer mode between wire and melt pool (a) droplet-like mode (b) smooth (c) smooth plunging (d) damaged bead due to high wire feed-rate [15].

1.3 Challenges in laser DED process

While there are numerous benefits of DED technology, some issues still exist that make this process very challenging to be accepted by the high standard industries such as medical or aerospace. Some of the main challenges include optimization and prediction of microstructure and mechanical properties [18-19], part quality and process monitoring [20-24], and process path planning [25-26]. The aim of this section is to address several important challenges in DED parts that prevent the industrial adoption of this technology.

1.3.1 Microstructure and mechanical properties

Complex microstructure usually exists in laser DED parts. DED parts normally undergo complicated thermal history during building process. Fast heat extraction, partially re-melting of previously deposited layers and rapid solidification make the dynamic of the process unpredictable [27]. A large number of studies have focused on effects of thermal cycles on microstructural evolution and mechanical properties of DED parts. There is a large number of processing parameters involved in DED process such as laser power, travel speed, material feed-rate and layer thickness. These parameters affect directly the

mechanical properties, thermal gradient, and final solidification structure and therefore, they must be optimized and tuned accurately to achieve high quality parts [28]. The specific energy (E) is a key factor in laser DED process since it specifies the amount of input energy to the melt pool. The specific energy is a function of laser power, P, laser beam diameter, d, and travel speed, TS, which is defined by the equation $E = \frac{P}{TS \times d}$ [29]. Ma et al. [30], studied the effect of specific energy on the 316L SS as-deposited samples in laser cladding deposition (LCD) process. They considered three sets of parameters to achieve three processing techniques, namely, small-size LCD, middle-size LCD and large-size LCD, as can be seen in Table 1.2.

Table 1.2 Process parameters and experimental design level used for experimentations [30].

Processing technique	P (W)	TS (mm/s)	d (mm)	E (J/mm2)
Small-size LCD	1400	28	1.0	50
	1600	28	1.1	51.9
	1800	28	1.2	53.6
	2000	28	1.3	55
Middle-size LCD	3200	10	5.0	64
	3400	10	5.2	65.4
	3600	10	5.4	66.7
	3800	10	5.6	67.9
Large-size LCD	4400	5	11.2	78.6
	4600	5	11.4	80.7
	4800	5	11.6	82.8
	5000	5	11.8	84.7

The results of the microstructural analysis are shown in Fig. 1.7. The primary cellular arm spacing increases from the order of 5µm to 15µm as the specific energy increases from 50J/mm to 80 J/mm. Therefore, the cooling rate of melt pool, which is a function of cell size, decreases as the specific energy increases [30]. The effect of specific energy on microhardness and tensile properties of the samples shown in Fig. 1.8. (a) reveals

that UTS (ultimate tensile strength) and yield strength decreased while elasticity increased as the E increases. There is also obvious impact on microhardness as seen in Fig. 1.8. (b).

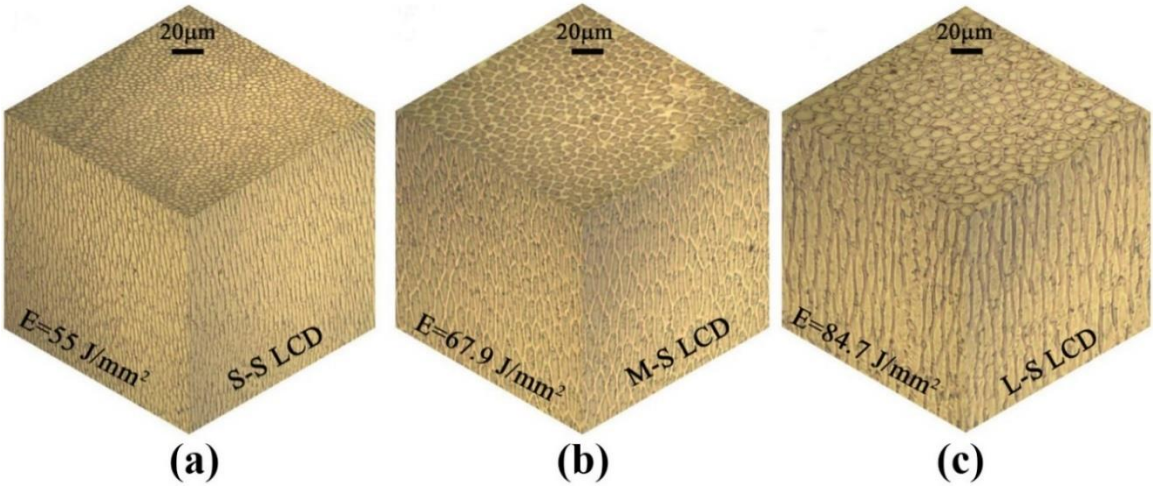

Figure 1.7 3D composite view showing the cellular morphologies of samples with condition of (a) small-size LCD (b) meddle-size LCD and (c) large-size LCD [30].

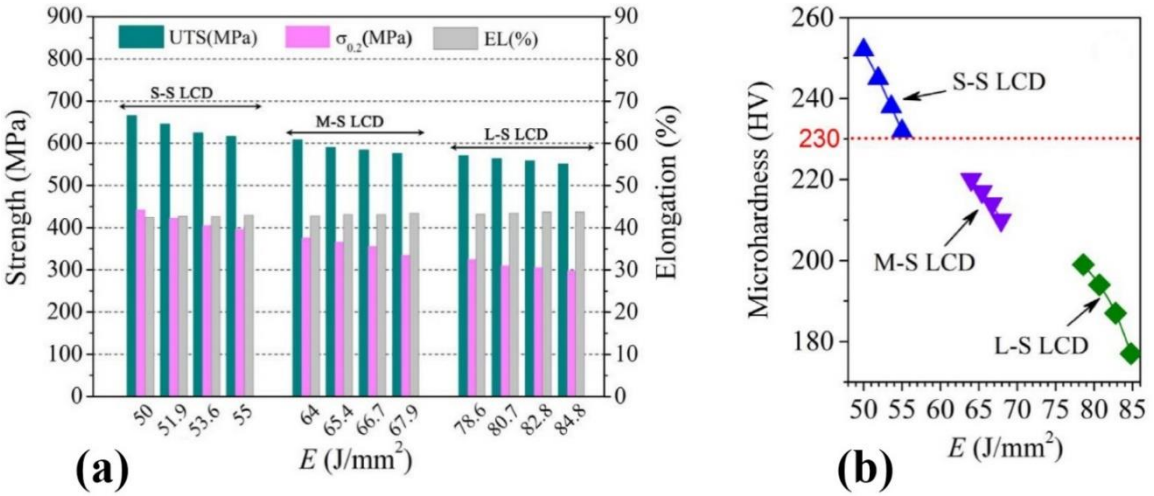

Figure 1.8 Effect of specific energy (E) on (a) tensile properties (b) microhardness of 316L as-deposited samples [30].

Another important factor in laser DED that has impact on thermal history, and thereby on microstructure of final buildup is inter-layer time interval. This is the time required for the laser to return to the identical bead in the next layer. Foster et al. [31], studied the effect of inter-layer time on the deposition of Inconel 625 and Ti-6Al-4V alloys.

They found that a finer microstructure, a higher UTS and yield strength and higher microhardness levels could be achieved when the inter-layer time were increased from 0 to 40 sec. Yadollahi at al. [32], also revealed that the mechanical and microstructural properties of 316L SS laser DED parts are dependent on the inter-layer time interval. They fabricated two types of samples: single-built and nine-built, with identical process parameters as can be seen schematically in Fig. 1.9. The single-built part was built continuously layer by layer with a short inter-layer time interval whereas in nine-built part, one layer of all nine cylinders were deposited before the next layer is started, producing a long inter-layer time interval [32].

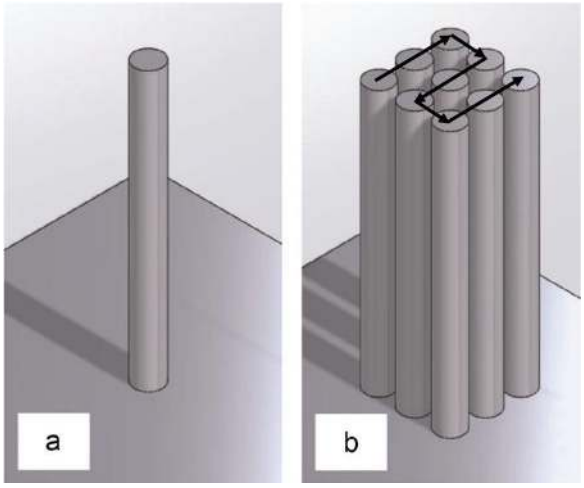

Figure 1.9 Schematic of fabricated cylindrical rods (a) one cylindrical rod built at a time, i.e. single-built, and (b) nine samples built at a time, i.e. nine-built [32].

The EBSD (electron backscattered diffraction) analysis (Fig. 1.10) revealed that while both samples had very low misorientation angles (average ≈15°), indicating a near-mono crystalline texture, the average grain size was 45μm for nine-built whereas it was 60μm for single-built part [32]. This is attributed to the increased inter-layer time interval and thereby higher cooling rates in nine-built sample.

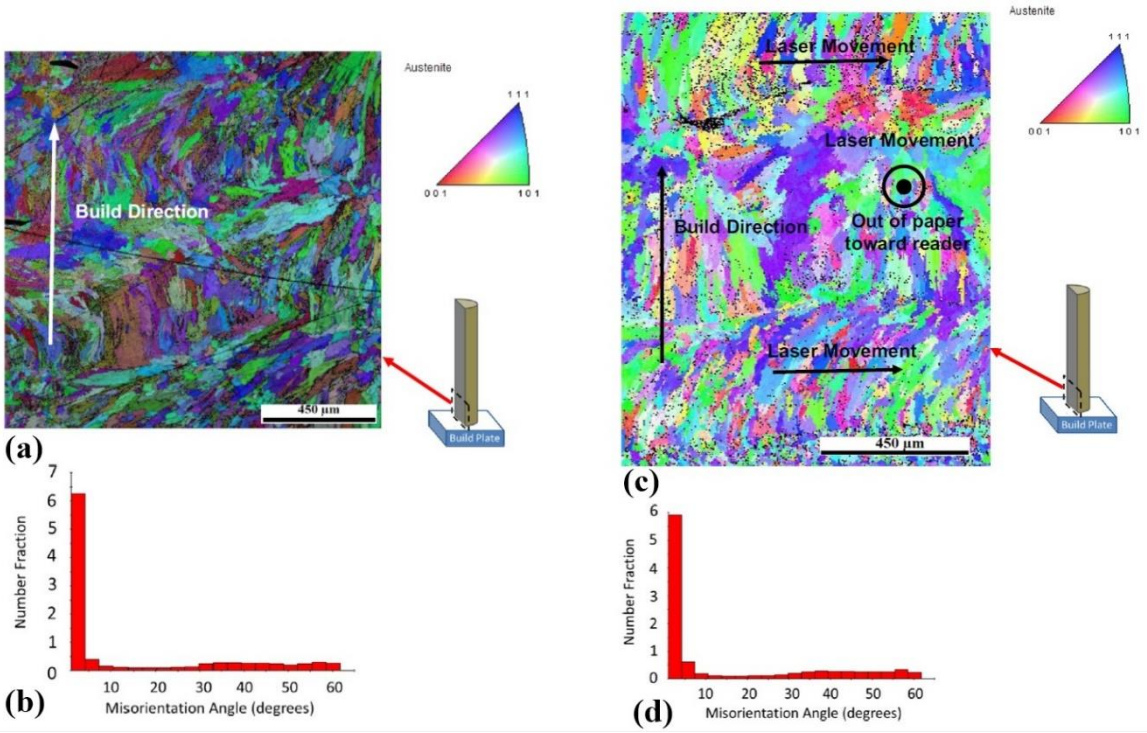

Figure 1.10 EBSD inverse pole map for (a) single-built (c) nine-built. Misorientation angle distribution of austenite phase for (b) single-built (d) nine-built (red: [001]; blue:[111]; green:[101]) [32].

Another challenge in laser DED process is inherent anisotropy and heterogeneity of microstructure and mechanical properties of the as-fabricated parts. Epitaxial columnar grain morphology is the most common feature of laser DED microstructure [33]. Such columnar morphology of grains which are usually elongated in the build direction has been recognized as the main source of anisotropy of mechanical properties [34]. Heterogeneity also exists in metal laser DED parts, which arises from variations in grain morphology, size and chemical composition. Heterogeneity could be a result of change in thermal condition of part being fabricated [35]. Cyclic thermal history caused by successive layer deposition leads to variations in microstructure. For instance, an equiaxed-to-columnar transition of prior β grains in Ti-6Al-4V alloy, was observed at the beginning of EBM

(electron beam melting) deposited part [36] (see Fig.1.11). This transition is mainly attributed to the fast heat dissipation in the first several layers which caused a higher degree of super cooling and thereby an equiaxed-to-columnar transition [36].

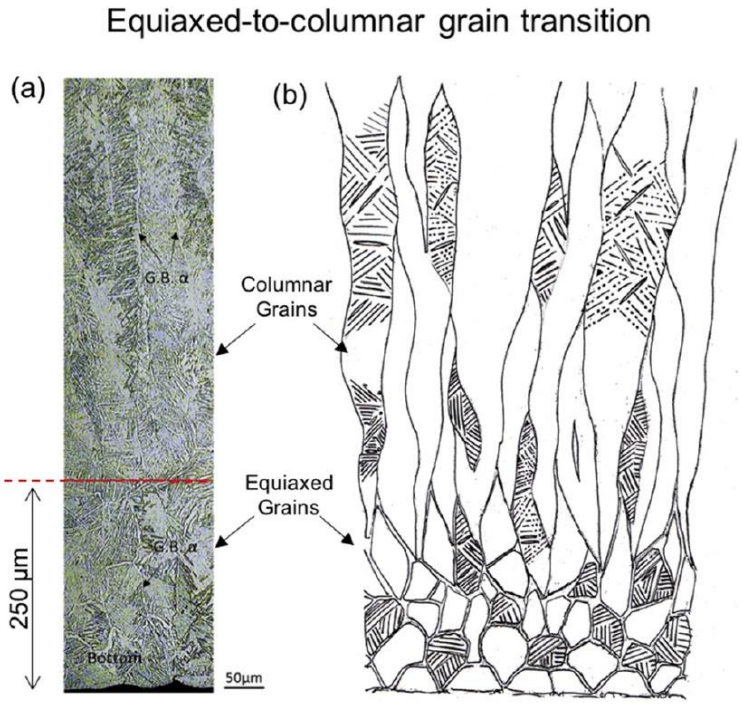

Figure 1.11 (a) optical micrograph (b) schematic showing the equiaxed-to-columnar transition in Ti-6Al-4V alloy due to fast heat sink in initial layers [36].

The processing parameters also influence the dynamics of the melt pool that could eventually cause the formation of defects [32]. Process induced defects such as pores, rough surfaces and lack-of-fusion between layers could also lead to anisotropy and heterogeneity in mechanical properties of metal AM parts [37-38]. Despite all efforts made to understand the microstructural and mechanical behavior of DED parts, more focused research still required to thoroughly optimize all factors affecting the properties of as-built parts.

1.3.2 Process monitoring and control

Numerous studies have focused on implementation of process monitoring and feedback control in order to improve the quality of parts and to increase the stability and repeatability of the process [39-41]. Process monitoring and control is necessary in DED because usually the existence of process disturbances and fluctuations in process parameters (e.g. laser power, travel speed or material feed-rate) could deviate the process from pre-optimized condition, leading to instability or producing defects in part. The change in thermal condition of the buildup, i.e. the transition from 3D conduction mode to 2D during the process is an example of process disturbance. Process monitoring of DED in literature mostly focused on monitoring of either melt pool size or melt pool temperature [42-46]. Different types of sensors such as vision sensors (e.g. CCD camera or CMOS camera) or thermal sensors (e.g. IR camera or pyrometer) could be utilized to monitor the melt pool. Then, the signal from sensor is compared with pre-set value and the resulting error will be used as an input of controller. Eventually, the controller sends a signal to adjust the control variable (e.g. laser power or travel speed) in order to maintain the melt pool size or temperature constant over the process. Most of the studies in literature relied on the fixed controller parameters. Given the non-linear dynamic of the DED process, there is a need for adaptable controller that can correspond to non-linear behavior of process.

1.3.3 Process path planning

Process path planning is also one of the challenges in robotized DED, especially when it comes to fabrication of complex freeform parts. In DED, there is no support material, therefore the kinematics of robot should prevent the melt pool from collapse. This issue is more pronounced when wire is used as material feedstock. This is mainly because

the best quality of deposition is achieved when the wire is fed from leading edge of melt pool [17]. Thus, the part with overhang section could be difficult to build. One solution is to use adaptive slicing algorithm to build non-uniform thickness layers due to variations in build orientation [47]. There are also other methods to deal with overhang parts, however, these techniques could make the path planning even more complicated. Therefore, there still exists a lack of techniques that can increase the flexibility of DED process in terms of building overhangs, while simplifying the process planning.

1.4 Research objectives

The aforementioned issues have been addressed in the developed robotized laser directed energy deposition system at RCAM at SMU. The main objectives can be categorized as follows:

- To investigate the mechanical and microstructural properties of the as-built parts.
- To develop method to join the as-fabricated parts by using autogenous laser welding.
- To develop a closed-loop controller to control the width of melt pool in a laser-based directed energy deposition system.

REFERENCES

[1] ASTM, Standard Terminology for Additive Manufacturing Technologies, ASTM F2792-12a ASTM International, West Conshohocken, PA (2010)

[2] Kok, Yihong, et al. "Anisotropy and heterogeneity of microstructure and mechanical properties in metal additive manufacturing: A critical review." Materials & Design 139 (2018): 565-586.

[3] Bikas, H., Panagiotis Stavropoulos, and George Chryssolouris. "Additive manufacturing methods and modelling approaches: a critical review." The International Journal of Advanced Manufacturing Technology 83.1-4 (2016): 389-405.

[4] Thompson, Scott M., et al. "An overview of Direct Laser Deposition for additive manufacturing; Part I: Transport phenomena, modeling and diagnostics." Additive Manufacturing 8 (2015): 36-62.

[5] Frazier, William E. "Metal additive manufacturing: a review." Journal of Materials Engineering and Performance 23.6 (2014): 1917-1928.

[6] DebRoy, Tarasankar, et al. "Additive manufacturing of metallic components–process, structure and properties." Progress in Materials Science 92 (2018): 112-224.

[7] Retrieved from: https://www.siemens.com/innovation/en/home/pictures-of-the-future/industry-and-automation/additive-manufacturing-3d-printed-gas-turbine-blades.html

[8] Ding, Yaoyu, et al. "3 Use of Powder-Feed Metal Additive Manufacturing System for Fabricating Metallic Metamaterials." Manufacturing Techniques for Materials: Engineering and Engineered. CRC Press, 2018. 51-65.

[9] Retrieved from: https://ramlab.com/

[10] Additive Manufacturing—General Principles—Terminology; ISO/ASTM 52900; International Organization for Standardization: Geneva, Switzerland, 2015.

[11] Hofmeister, William, et al. "Investigating solidification with the laser-engineered net shaping (LENSTM) process." Jom 51.7 (1999): 1-6.

[12] Qi, Huan, Magdi Azer, and John Deaton. "Development of transfer functions for controlling fabrication of components by laser net shape deposition (LNSM)." International Congress on Applications of Lasers & Electro-Optics. Vol. 2005. No. 1. LIA, 2005.

[13] Heralić, Almir, et al. "Increased stability in laser metal wire deposition through feedback from optical measurements." Optics and Lasers in Engineering 48.4 (2010): 478-485.

[14] Heralić, Almir, Anna-Karin Christiansson, and Bengt Lennartson. "Height control of laser metal-wire deposition based on iterative learning control and 3D scanning." Optics and lasers in engineering 50.9 (2012): 1230-1241.

[15] Heralic, Almir. Towards full automation of robotized laser metal-wire deposition. Diss. 2009.

[16] Mok, Sui Him, et al. "Deposition of Ti–6Al–4V using a high power diode laser and wire, Part I: Investigation on the process characteristics." Surface and Coatings Technology 202.16 (2008): 3933-3939.

[17] Syed, Waheed Ul Haq, and Lin Li. "Effects of wire feeding direction and location in multiple layer diode laser direct metal deposition." Applied Surface Science 248.1-4 (2005): 518-524.

[18] Fu, Youheng, et al. "Investigation of mechanical properties for hybrid deposition and micro-rolling of bainite steel." Journal of materials processing technology 250 (2017): 220-227.

[19] Wang, Xiaoqing, Tahmina Keya, and Kevin Chou. "Build height effect on the Inconel 718 parts fabricated by selective laser melting." Procedia Manufacturing 5 (2016): 1006-1017.

[20] Kriczky, Dennis A., et al. "3D spatial reconstruction of thermal characteristics in directed energy deposition through optical thermal imaging." Journal of Materials Processing Technology 221 (2015): 172-186.

[21] Bi, Guijun, et al. "Characterization of the process control for the direct laser metallic powder deposition." Surface and Coatings Technology 201.6 (2006): 2676-2683.

[22] Nassar, Abdalla R., et al. "Intra-layer closed-loop control of build plan during directed energy additive manufacturing of Ti–6Al–4V." Additive Manufacturing 6 (2015): 39-52.

[23] Bi, Guijun, et al. "Investigation on the direct laser metallic powder deposition process via temperature measurement." Applied Surface Science 253.3 (2006): 1411-1416.

[24] Rodríguez-Araújo, Jorge, and Antón García-Díaz. "OpenLMD, multimodal monitoring and control of LMD processing." High-Power Laser Materials Processing: Applications, Diagnostics, and Systems VI. Vol. 10097. International Society for Optics and Photonics, 2017.

[25] Dwivedi, R., and R. Kovacevic. "Process planning for multi-directional laser-based direct metal deposition." Proceedings of the Institution of Mechanical Engineers, Part C: Journal of Mechanical Engineering Science 219.7 (2005): 695-707.

[26] Pinilla, J. Miguel, Ju-Hsien Kao, and Fritz B. Prinz. "Process planning and automation for additive-subtractive solid freeform fabrication." Proceedings of the Solid Freeform Fabrication Symposium. 1998.

[27] Kelly, S. M., and S. L. Kampe. "Microstructural evolution in laser-deposited multilayer Ti-6Al-4V builds: Part II. Thermal modeling." Metallurgical and Materials Transactions A 35.6 (2004): 1869-1879.

[28] Fayazfar, Haniyeh, et al. "A critical review of powder-based additive manufacturing of ferrous alloys: Process parameters, microstructure and mechanical properties." Materials & Design 144 (2018): 98-128.

[29] Mazumder, Jyoti, A. Schifferer, and J. Choi. "Direct materials deposition: designed macro and microstructure." Material Research Innovations 3.3 (1999): 118-131.

[30] Ma, Mingming, Zemin Wang, and Xiaoyan Zeng. "A comparison on metallurgical behaviors of 316L stainless steel by selective laser melting and laser cladding deposition." Materials Science and Engineering: A 685 (2017): 265-273.

[31] Foster, B. K., et al. "Impact of interlayer dwell time on microstructure and mechanical properties of nickel and titanium alloys." Metallurgical and Materials Transactions A 48.9 (2017): 4411-4422.

[32] Yadollahi, Aref, et al. "Effects of process time interval and heat treatment on the mechanical and microstructural properties of direct laser deposited 316L stainless steel." Materials Science and Engineering: A 644 (2015): 171-183.

[33] Wang, Pan, et al. "Spatial and geometrical-based characterization of microstructure and microhardness for an electron beam melted Ti–6Al–4V component." Materials & Design 95 (2016): 287-295.

[34] Carroll, Beth E., Todd A. Palmer, and Allison M. Beese. "Anisotropic tensile behavior of Ti–6Al–4V components fabricated with directed energy deposition additive manufacturing." Acta Materialia 87 (2015): 309-320.

[35] Kelly, S. M., and S. L. Kampe. "Microstructural evolution in laser-deposited multilayer Ti-6Al-4V builds: Part II. Thermal modeling." Metallurgical and Materials Transactions A 35.6 (2004): 1869-1879.

[36] Tan, Xipeng, et al. "Graded microstructure and mechanical properties of additive manufactured Ti–6Al–4V via electron beam melting." Acta Materialia 97 (2015): 1-16.

[37] Wu, Ming-Wei, Pang-Hsin Lai, and Jhewn-Kuang Chen. "Anisotropy in the impact toughness of selective laser melted Ti–6Al–4V alloy." Materials Science and Engineering: A 650 (2016): 295-299.

[38] Baicheng, Zhang, et al. "Study of selective laser melting (SLM) Inconel 718 part surface improvement by electrochemical polishing." Materials & Design 116 (2017): 531-537.

[39] Hu, Dongming, and Radovan Kovacevic. "Sensing, modeling and control for laser-based additive manufacturing." International Journal of Machine Tools and Manufacture 43.1 (2003): 51-60.

[40] Toyserkani, Ehsan, and Amir Khajepour. "A mechatronics approach to laser powder deposition process." Mechatronics 16.10 (2006): 631-641.

[41] Salehi, Dariush, and Milan Brandt. "Melt pool temperature control using LabVIEW in Nd: YAG laser blown powder cladding process." The international journal of advanced manufacturing technology 29.3-4 (2006): 273-278.

[42] Bi, Guijun, et al. "Characterization of the process control for the direct laser metallic powder deposition." Surface and Coatings Technology 201.6 (2006): 2676-2683.

[43] Song, Lijun, et al. "Control of melt pool temperature and deposition height during direct metal deposition process." The International Journal of Advanced Manufacturing Technology 58.1-4 (2012): 247-256.

[44] Hofman, J. T., et al. "A camera based feedback control strategy for the laser cladding process." Journal of Materials Processing Technology 212.11 (2012): 2455-2462.

[45] Heralić, Almir, et al. "Increased stability in laser metal wire deposition through feedback from optical measurements." Optics and Lasers in Engineering 48.4 (2010): 478-485.

[46] Ding, Yaoyu, James Warton, and Radovan Kovacevic. "Development of sensing and control system for robotized laser-based direct metal addition system." Additive Manufacturing 10 (2016): 24-35.

[47] Zhang, Jun, and Frank Liou. "Adaptive slicing for a multi-axis laser aided manufacturing process." Journal of Mechanical Design 126.2 (2004): 254-261.

Chapter 2

AN INVESTIGATION ON MECHANICAL AND MICROSTRUCTURAL PROPERTIES OF 316LSI PARTS FABRICATED BY A ROBOTIZED LASER/WIRE DIRECT METAL DEPOSITION SYSTEM

2.1 Introduction

Additive Manufacturing (AM) processes are finding application in many sectors of industries from healthcare, automotive, and mold tooling to aerospace. The rapid development of AM is due to its capability of fabricating complex geometries, reducing production time, and eliminating the need for expensive tooling and fixtures. It is becoming an economic and efficient method in the low volume production of high value parts. There is a wide variety of metal AM processes. Most of them are classified into two broad categories: Powder Bed Fusion (PBF) systems and Directed Energy Deposition (DED) systems [1]. According to ISO/ASTM 52900:2015 [2], DED is defined as "an additive manufacturing process in which focused thermal energy is used to fuse materials by melting as they are being deposited." In powder bed fusion processes, a bed of powder is selectively sintered or melted via laser or electron beam heat source. In contrast, DED is accomplished by continuous feeding of metallic powder or wire into the melt pool formed by a highly focused energy source such as laser, electron beam, or arc. Relative motion of

the heat source to the substrate will generate the pre-defined pattern. This process repeats until a solid free form part is constructed.

Laser direct metal deposition (L-DMD), as a DED process, has been recognized with different terminologies in literature such as 3D laser cladding, shaped metal deposition (SMD), laser metal deposition (LMD), direct metal deposition (DMD), and direct laser deposition (DLD). It has been increasingly utilized in many applications. L-DMD provides unique advantages, including the ability to print the functionally-graded materials (FGM) [3,4], repair of high valuable components [5], and surface cladding of parts exposed to heavy loadings (die and mold) or harsh conditions (corrosive, erosive, or wear). Printing the metamaterial (exotic) with unusual behavior such as large Poisson's ratio, negative Poisson's ratio, or negative coefficient of thermal expansion is also one of the application of L-DMD systems [6].

Laser wire direct metal deposition (LW-DMD), a L-DMD process which uses wire as a feedstock, has recently gained more attention. LW-DMD has a low cost of feedstock (it uses commercial welding wire), higher deposition rate (up to 40 lb/hr for titanium alloy, compared to the powder-fed deposition system with 1.6 lb/hr [7]), maximum material efficiency, and cleaner environment. Thus, many leading companies in the metal AM industry (e.g. GKN aerospace in collaboration with the National Oak Ridge Laboratory) use LW-DMD to fabricate large structures that would be almost impossible to build using the other AM techniques. Aside from the tremendous advantages of this process, experiments have shown that LW-DMD is a demanding and difficult-to-control process. Main process parameters such as laser power, wire feed speed, scanning speed, overlap factor and height-increment must be tuned accurately to achieve a stable and repeatable

process and avoid common issues like droplet formation and wire dripping [8]. Experiments show that due to the change in heat transfer mode during the process (usually from 3D to 2D conduction) and also because of complexity in predicting the physical phenomena (melt pool dynamics), it is necessary to implement an online monitoring and control system. In addition, there exist small variations in some process variables such as material feed rate, laser power, and thermal conductivity (a temperature-dependent variable). These alterations require the use of a control system in order to achieve material integrity [9]. Heralic, et al. [10, 11] in an attempt to apply the feedback control system in LW-DMD process, were able to keep the width and height of the melt pool constant and ensure the maximum stability. Yaoyu et al. [12] utilized a coaxial camera on the laser head to monitor the melt pool and by applying a PID controller they successfully adjusted the laser power in real-time in order to keep the melt pool size constant during the laser/powder direct metal deposition process. The sensing and control of the wire direct metal deposition system is of great importance, although it is out of the scope of the current study.

In LW-DMD, the wire is fed usually from one side, although there exits new commercial laser cladding heads, e.g. from Fraunhofer IWS, in which the wire is fed coaxially and laser beam is split into several separate beams that subsequently focused onto a circular focal point. That is, an omni-directional deposition is feasible. However, side-feeding of wire makes the path planning more difficult since the wire should be always fed at the leading edge of the melt pool in order to obtain the best results in terms of surface roughness and porosity [13]. Yaoyu et al. [14], developed a Matlab-based offline path planning software to be used for printing the complex geometries by an 8-axis robotized laser/wire direct metal deposition system.

It has been shown that the mechanical properties of the metal AM parts are comparable to the conventionally manufactured parts [15]. However, mechanical and microstructural properties of the AM parts have been a major concern because of the complicated thermal history that the part experiencing during the building process [15]. Hederick [16] in a review of the metal additive manufacturing processes, mentioned that there is a need to study the relation between thermal history and evolution of material microstructure. Much research has focused on perceiving the effects of thermal cycles on microstructure evolution and mechanical properties of L-DMD parts. Thermal history during L-DMD, comprises the fast heating/cooling rates and considerable temperature gradients. It plays a significant role on microstructural characteristics and eventually determines the mechanical properties of the final part [17]. Yadollahi et al. [18] reported that the process parameters could influence the dynamics of the molten pool and accordingly the thermal history will be affected. Thus the process parameters might have caused the formation of defects. They also studied the effects of time interval between successive layers of deposition on mechanical and microstructural properties of buildups. The results showed that longer time intervals resulted in higher cooling rates, leading to finer microstructure. Su et al. [19], investigated the effects of structure types, namely two commonly-used structures: block and thin wall, on the microstructural evolution of deposited parts. The thin wall samples showed columnar grains that were parallel to the building direction, whereas the block coupons revealed multi-directional grain growth. In literature, the mechanical and microstructural properties of DMD parts have been compared to wrought or conventionally as-fabricated parts. In some cases the orientation-dependent properties are also reported. In a review by Lewandowski et al. [20], mechanical

properties of metal parts fabricated by a wide variety of AM processes were reviewed. Carrol et al. [21] in an investigation on anisotropic tensile properties of Ti-6Al-4V parts fabricated by DMD showed an improvement in mechanical properties of AM parts compared to wrought parts. They also studied the orientation-dependent, location-dependent, and oxygen-dependent material properties of the as-built parts. Similarly, Zheng et al. [22] demonstrated the notable enhancement in strength and ductility of the parts manufactured by Laser Engineered Net Shaping (LENS®) process for 316L SS. Furthermore, Zhang et al. [23], studied the effects of travel speed on tensile properties and hardness. They found that by increasing the travel speed these properties were improved. To show the orientation-dependent tensile properties of LW-DMD parts, Xu et al. [24] revealed that the strength of sample parallel to the deposition direction is higher than the one normal to deposition. Despite all efforts made to study the mechanical and microstructural properties of L-DMD process (using mostly powder as feedstock), less attention has been given to a laser-wire direct metal deposition process.

The current study focused on the characterization of mechanical and microstructural properties of 316LSi stainless steel parts fabricated by a robotized laser-wire direct metal deposition system developed in RCAM (Research Center for Advanced Manufacturing) at Southern Methodist University (SMU), Dallas, TX. The developed system is based on the robotized highly flexible kinematic motion system capable of fabricating complex and overhang geometries without requiring support structure with tolerances mostly within ±0.5 mm [8]. Two distinct geometries, namely thin-walled and block, were considered to study the effects of inter-layer time interval as well as part orientation on the evolution of microstructure and mechanical properties of the buildups.

2.2 Experimental procedure

2.2.1 Materials

An austenitic stainless steel (316LSi) was used as a feedstock material in a LW-DMD process. This material has a similar properties of 316L SS but with slightly higher content of silicon that improves the wetting behavior of the metal during welding. 316L SS material with an excellent corrosion resistance is widely used in applications where superior corrosion resistance or high elevated temperature strength is needed [25]. Typical parts made of 316L SS and welded with 316LSi are finding applications in jet engine, chemical and food processing, oil and gas industry, and biomaterials processing systems.

The feedstock wire was OK Autorod 316LSi from ESAB with a diameter of 1.2mm. A commercially available 304L plate with thickness of 6 mm was used as a substrate. The chemical compositions of wire and substrate are provided in Table 2.1.

Table 2.1 Chemical compositions of wire and substrate.

Element (wt.%)	C	Mn	Si	Ni	Mo	Cr	Cu	P	S	Fe
Wire (316LSi)	0.01	1.8	0.9	12.2	2.60	18.4	0.12	0.03	0.03	Bal.
Substrate (304L)	0.03	2	-	8	-	18	-	0.045	0.03	Bal.

2.2.2 System overview and procedure

A robotized laser/wire direct metal deposition system was used to perform the experimentations. Fig. 2.1 demonstrates the experimental setup along with a few parts fabricated by this system. As a motion system, a 6-axis KUKA robot (KR-60) with a 2-axis rotary table that were spatially coupled was used to provide the kinematics of the laser processing head. As a heat source, an IPG 4 kW fiber laser with 1070 nm wavelength was utilized to melt the material. A Precitec YW50 laser welding head was mounted on the

robot arm. The laser beam was defocused at 10mm below the focal point, resulting in 1.6mm beam spot diameter. The wire material is continuously fed to the processing zone by means of a Binzel wire feeding system. The system has two synchronized motors (push/pull) enabling an accurate and consistent wire feed speed. In addition, an image monitoring system was installed at the laser head to capture the images from melt pool in real-time. The setup included a CMOS camera (Prosilica GC640) that was installed coaxially in the laser head, an infrared filter (>700nm), an iris, a set of optical mirrors and an infrared notch-filter (1070nm). The camera had a monochrome mode with 640x480 pixels resolution and a maximum rate of 200 frames per second. The infrared filter was used to reduce the high intensity light from the melt pool and was installed in front of the camera chip. The iris was used to adjust the brightness of the light received by the camera to prohibit the over-exposure. Optical mirrors inside the laser head guided the light from melt pool towards the CMOS chip of the camera. The infrared notch-filter was utilized to block the laser light with wavelength of 1070nm to protect the camera from laser damage.

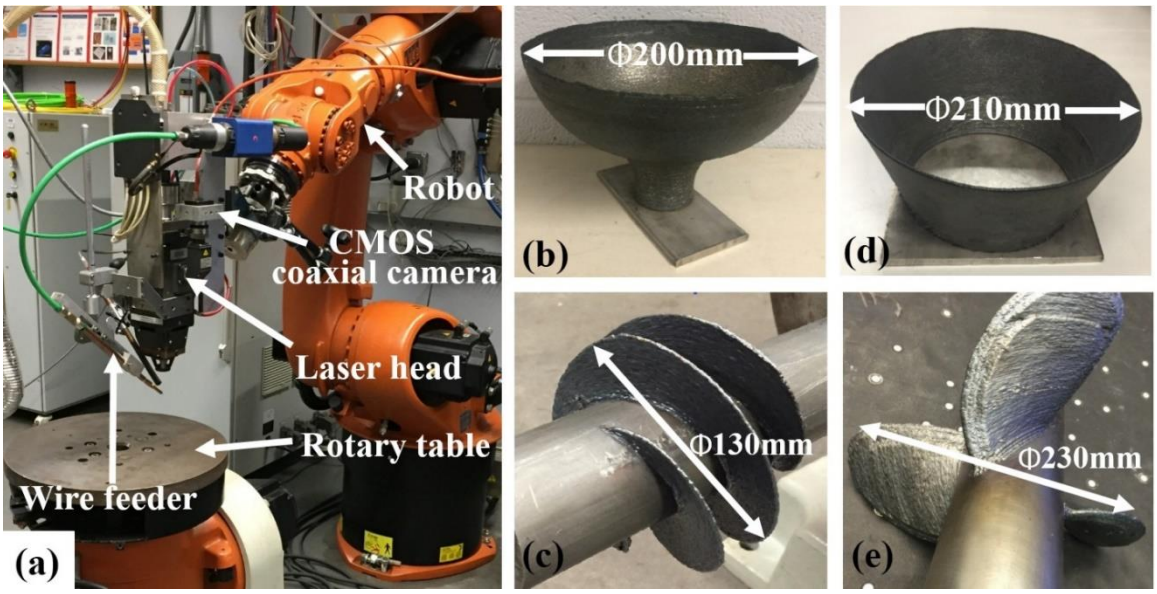

Figure 2.1 (a) A robotized laser/wire direct metal deposition system; (b)-(e) photographs of a few as-built parts fabricated by this system.

Similar to all AM processes, in the first step the 3D CAD model of the desired object was created and then converted to a file format that needs to be sliced. Different file formats can be utilized, depending on the technique and manufacturer, however STL (Standard Tessellation Language) file is the most common format in AM industry. The STL file, a 3D representation of the CAD model, contains a set of mesh triangles and has been commonly utilized in AM industry. Since the AM part is constructed in a layer-wise fashion, the STL file needs to be sliced into a number of 2D planes. For each plane (slice) a toolpath strategy is required. The slicing and generating toolpath are accomplished through either a commercial offline programming software called SKM DCAM or RCAM-developed Matlab-based software. After the program was prepared, the substrate was placed at the rotary table. The tool center point (TCP) and rotary table are synchronously moving with respect to each other in space based on the offline program, and once the laser

and wire feeder are turned on, the material started to be deposited bead by bead and layer by layer.

All samples for characterizing the mechanical and microstructural properties were built by using the robotized LW-DMD system at RCAM with the optimized parameters listed in Table 2.2.

Table 2.2 Optimized process parameters used for fabricating samples.

Process Parameters	Laser Power (W)	Wire Feed Speed (mm/s)	Z-increment (mm)	Overalap increment (mm)	Travel speed (mm/s)	Shielding gas flow rate (l/min)
Value	1000	12	0.85	1.35	8	15 (Argon)

Process parameters influencing cooling rates also affect quality, microstructure and mechanical properties of the fabricated parts. Therefore, it is necessary to determine the optimal process parameters. Accordingly, a set of experiments were implemented, in earlier study [8], to realize the issues and challenges and eventually overcome them. The effects of main parameters such as laser power, travel speed, wire feed speed, overlap factor and height-increment on bead geometry of single-bead and multi-bead deposition were studied. Finally, a proper window for selecting the process parameters for building the specific part was found. The process parameters in Table 2.2 are based on the experiments performed in [8].

In order to investigate the mechanical and microstructural properties of the fabricated parts, two coupon types, block and thin-walled, were considered as shown in the Fig. 2.2. The purpose of selecting these two types of coupons was to study the effect of different inter-layer time intervals on the thermal history and on the final microstructure

and mechanical properties of the buildups. The inter-layer time interval is defined as a time taken by robot to move from end of a track to start of the identical track in the next layer. Obviously, the number of tracks in each layer and idle time (the time when laser is off and robot gets position) mainly determine the inter-layer time. Therefore, depending on the geometry (e.g. thin-walled or bulky), the part might have different inter-layer time. The inter-layer time significantly affects the initial temperature of previously-deposited layer, and accordingly the cooling and solidification rates are influenced. The changes on solidification rate will, in turn, affect the microstructural and mechanical properties of the part [24]. Some researchers also numerically studied the impacts of idle time either between two successive layers or two successive beads on temperature rise in buildup, melt pool dimension and cooling rate [26-28]. In the present study, the inter-layer time interval for block and thin-walled structures was measured, by a set timer, to be 420 s and 25 s, respectively. It should be noted that the amount of time that it took the robot to get into position for the next bead (while the laser was off) affected the inter-layer time. Therefore, to reduce this time, the repositioning of the laser deposition head was done at a higher speed (250 mm/s).

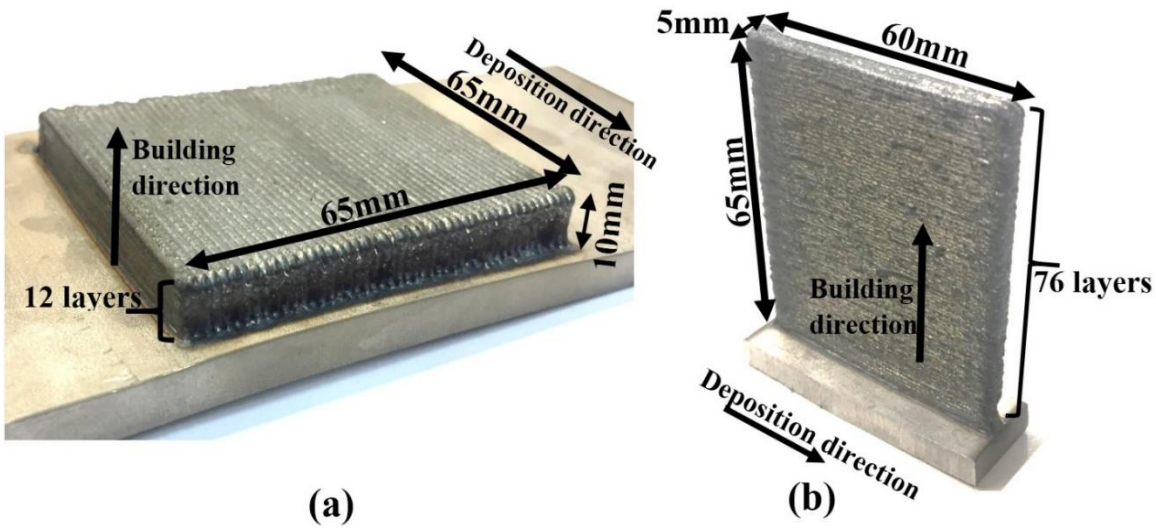

Figure 2.2 Photographs of the as-built 316LSi coupons along with their dimensions. (a) Block coupon; (b) thin-walled coupon.

In each coupon type, tensile samples in parallel and perpendicular directions relative to the deposition direction (beads axis) were prepared to further study the anisotropic behavior of the as-built coupons. Subsequently, a set of samples for microstructural analysis, tensile testing and microhardness were prepared. Tensile tests were performed on an Instron 5582 tensile testing machine with 1 mm/min strain rate at room temperature. Moreover, two sets of samples were heat treated for 2 hours at 1120°C in a furnace and then air cooled to homogenize the microstructure. The procedure was based on the standard annealing of austenitic stainless steel [29]. One specimen from each set was mounted, sanded, and polished using a diamond polishing pad. The specimens were chemically etched in a solution of (HCL: HNO3=3:1) for 40 sec. The microstructure of the buildups was examined by using an optical microscope (Olympus DP72) and scanning electron microscope (FEI Nova NanoSEM 230) equipped with energy dispersive spectroscopy (EDS). Hardness testing was also conducted via a Vickers microhardness tester (Clark-CM700). A fracture surface analysis was also conducted by SEM.

2.3 Experimental results and discussion

2.3.1 Microstructural analysis

In the current study, microstructural analysis was performed in various locations of the thin-walled and block buildups in normal cross sections. Figs. 2.3(a) and 2.4(a) depict the typical real-time grayscale images of the melt pool from the top-view in different layers of deposition. The corresponding microstructures from the 2nd and 70th layers of the thin-walled coupon are also shown in Fig. 2.3(b-h). The microstructure of block coupon from 2nd and 10th layers are displayed in Fig. 2.4(b-h). Real-time images of melt pool were taken during the process in order to find out the correlation between melt pool size and cooling rate, which will be discussed later in this section.

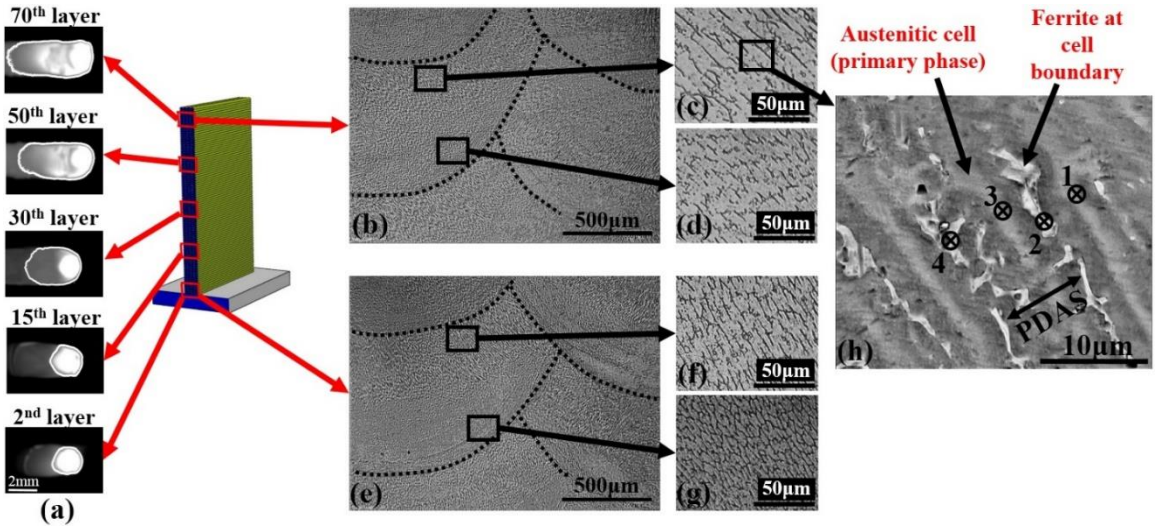

Figure 2.3 Thin-walled coupon. (a) Real-time isotherm images of melt pool in different layers along with melt pool boundary; (b) and (e) micrographs of the top and bottom layers in low magnification; (c),(d),(f) and (g) higher magnifications of

microstructure showing the elongated columnar grains; (h) SEM image indicating the dendritic structure along with EDS measured points.

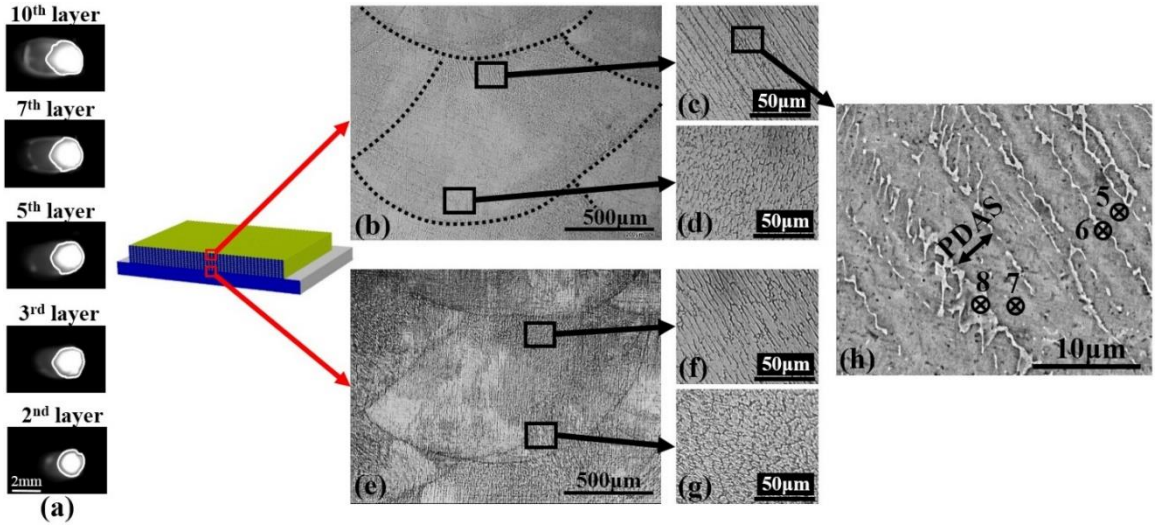

Figure 2.4 Block coupon. (a) Real-time isotherm images of melt pool in different layers along with melt pool boundary; (b) and (e) micrographs of the top and bottom layers in low magnification; (c),(d),(f) and (g) higher magnification of microstructure showing the elongated columnar grains; (h) SEM image indicating the dendritic structure along with EDS measured points.

As can be seen from Figs. 2.3 and 2.4, columnar grain structure was dominant as it is common for as-built AM parts. However, the size of the grains varied significantly in different locations. In general, more elongated, continuous and coarser columnar grains were observed in thin-walled coupons compared to block samples. This result indicated that the thin-walled sample owing to the shorter inter-layer time interval had lower cooling rates, which in turn, caused the formation of coarser grains.

It was also found that the size of the grains was changed from bottom to top in each layer. This phenomena was common in all layers of deposition for both coupon types. In some locations, the secondary dendritic features were observed. However, they were not pronounced at all regions. Therefore, primary dendritic arm spacing (PDAS) was used as a measure of the microstructural length scale. The mean intercept length method was used to calculate the PDAS. This method calculates the average grain size by dividing the length of randomly drawn lines (on the optical photographs) by the number of intersected grain boundaries. Each PDAS value (or inter-dendritic distance) was obtained as an average value of at least 5 measurements. The bottom section of each layer consisted mostly of fine columnar grains whereas there existed longer and coarser columnar grains in top sections. As for the block coupon, the average PDAS was increased from 3.5 µm to 4.5 µm and from 5.5 µm to 7 µm, in the first layer and 10^{th} layer, respectively (Figs. 2.4(c), (d), (f) and (g)). Similarly, in the first layers of the thin-walled coupon, the average PDAS was varied from 5 µm to 6 µm and it increased from 9.5 µm to 12 µm in the 70^{th} layer. The increase in size of the columnar grains in each layer from bottom to top could be explained by the higher cooling rates and solidification rates at the lower part of the melt pool. In contrast, the top portion of the melt pool experienced lower cooling rates, especially because the top section was exposed to re-melting. As a result, larger dendrites and even in some locations the secondary arms were observed. The effect of cooling rate on the size of microstructure could be described by the solidification map as shown in Fig. 2.5. That is, while the ratio of temperature gradient and solidification rate, G/R, is a critical factor in determining the morphology preference of solidification microstructure (planar, cellular, columnar dendritic or equiaxed dendritic), the product, GR, which is defined as cooling rate, controls

the size of the microstructure [30]. Therefore, due to the reduction in cooling rate (GR) from bottom to top section of the melt pool, a slight increase in the grain length scale was observed. Figs. 2.3(h) and 2.4(h) show the SEM microstructure in the top section of the buildups. By comparing the SEM image of the block with the thin-walled coupon, it could be clearly seen that inter-dendritic spacing or PDAS was larger in the case of thin-walled samples. This result demonstrated the lower cooling rate in the upper layers of this buildup.

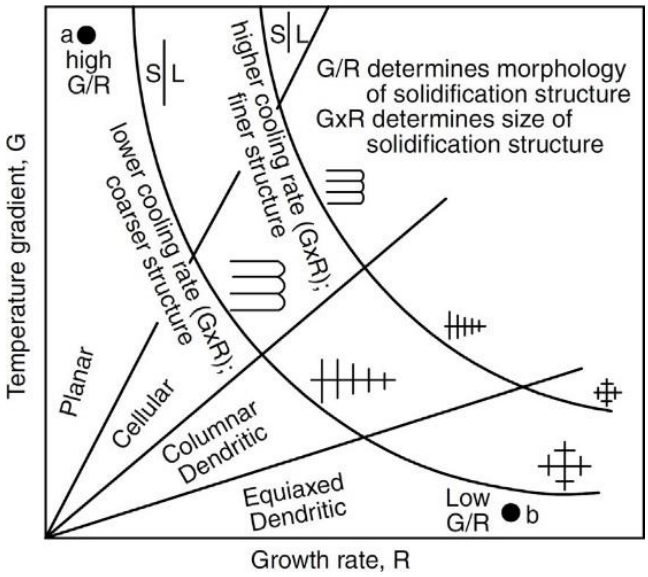

Figure 2.5 Solidification map showing the effect of temperature gradient G and growth rate R on morphology and size of the solidification microstructure [31].

Real-time grayscale images of melt pool were captured. A few of them in different layers were selected to be shown in Figs. 2.3(a) and 2.4(a). Based on the experimental observations, it was found that the shape of melt pool (from top-view) in laser wire metal deposition is not always in a regular oval shape. Depending on the local cooling rate, it could be irregular circular, oval or elongated oval shapes. In the first layers of deposition, where there exists a higher cooling rates, the length of melt pool is small and melt pool tends to form in an irregular circular shape. It should be noted that circular shape of melt

pool could be changed to more elongated oval shapes, even in the first layers, as the scanning speed increases. Studying the effect of scanning speed on melt pool shape is out of scope of this paper. Due to higher cooling rates throughout fabricating block sample, melt pools mostly appear in shortened oval shapes (Fig. 2.4(a)). However, as for the thin-walled sample, after several layers the melt pool appears to be in an elongated oval shape (Fig. 2.3(a)). The purpose of taking real-time images was to correlate the melt pool size with the corresponding microstructural length scale. The real-time information of the melt pool geometry could then be used to control and thereby tailor the microstructural and mechanical properties of the buildup. A CMOS camera (Prosilica GC640M) was coaxially mounted in the laser head to capture the infrared grayscale images of the melt pool from the top-view. Upon calibrating the infrared images of melt pool and obtaining the appropriate threshold for the melt pool boundary, the infrared image could represent the isotherm of the pool in real-time. The traditionally used method of calibrating the infrared image is to use a black body as detailed in [32]. In this method, the infrared image of the heated black body is captured simultaneously with the temperature measured by a thermocouple. Then, the relationship between the gray level of the infrared image and black body temperature is obtained. Based on the Planks's law and Wien's law, the radiance could represent the temperature of a target with different emissivities. By knowing the emissivity of melt pool and melting point of material, the corresponding infrared gray level of melt pool could be achieved. However, Hu et al. [32] and Ding et al. [12] indicated that use of a vision system for calibration of infrared image of the melt pool is more direct and reliable than using a black body. This method was also utilized for calibration of melt pool boundary in this study. In this method, both ordinary and infrared images of a referenced

melt pool (without feeding wire in order to capture clear images of melt pool) under the same travel speed (8mm/s) and laser power (1000W) acquired coaxially. In order to capture the ordinary image, the infrared filter in front of the camera chip was replaced with a bandpass optical filter (532nm). In addition, a green laser (532nm) with a power of 5W was used to illuminate the melt pool and surrounding area. Figs. 2.6 (a) and (b) show the infrared and ordinary images of the melt pool, respectively. The boundary of melt pool is obvious in Fig. 2.6(b). These two images were then overlapped and it was found that the gray level of 104 corresponded to contour of melt pool (the gray level range is 0-255). Fig. 2.6(c) illustrates the binarized image of the melt pool processed by the Vision Development Module of Labview software. The outlines of melt pools shown in Figs. 2.3(a) and 2.4(a) were obtained from the binary images of the corresponding melt pools. Therefore, the area inside the boundary represents the liquid state (melt pool) and the less bright area outside the contour is in the solid-liquid phase (mushy zone).The melt pool size, in terms of number of pixels inside the binary image, was recorded during the entire process. Then, the number of pixels were converted to the actual size of the melt pool. The values of melt pool area for all layers of both coupons are represented in Fig. 2.7. The melt pool areas of only one bead in each layer was shown in this Figure, since all beads in a same layer had similar melt pool size.

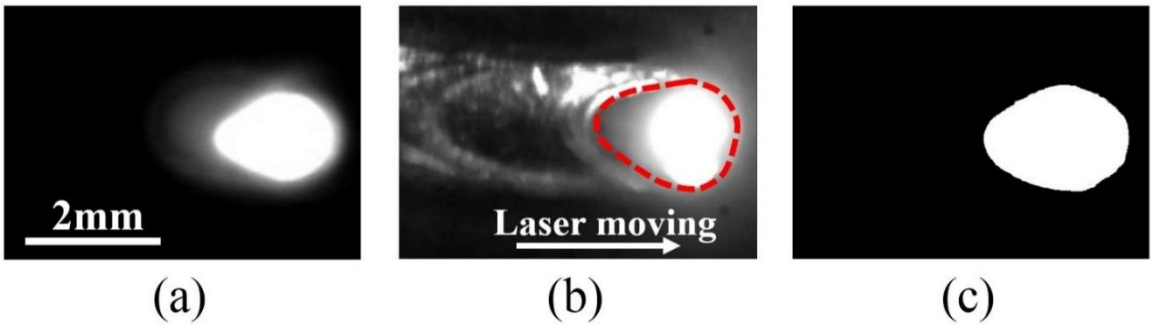

Figure 2.6 Captured top-view images of melt pool under the same scanning condition. (a) Original infrared image; (b) ordinary image; (c) binary image showing the boundary of melt pool.

The value of melt pool area, achieved by averaging 5 random images in each layer, was calculated for 10 different layers. In addition, the mean value of PDAS in the 10 selected layers was obtained. The PDAS value for each layer was considered as the average of PDAS values from bottom to top of that layer. The commonly-used empirical equation relating the cooling rate ($\dot{T}$) and primary dendrite arm spacing for SS 316L material was applied [22, 33]:

$$PDAS = 80\,\dot{T}^{-0.33} \tag{2.1}$$

By using Equation (2.1), a rough estimation of the cooling rates at the desired location of the buildup was achieved, and the results are plotted in Fig. 2.8(a). The images of the melt pool in the first layer of deposition were not considered since the process was not stable. Fig. 2.8(b) shows the variation of PDAS as the layer number was increased. A typical micrograph of the deposition that illustrates the intercepted grain boundaries are also shown in Fig. 2.8(b). The distance between the circular points on the lines determine the inter-dendritic distances. The average of these distances on each line gives the PDAS value. It can be seen that PDAS became larger as the number of layers increased, especially

after the 40th layer in thin-walled coupons. This could be due to the change in the heat conduction mode from 3D to 2D that caused a lower cooling rates at top layers of thin-walled coupon.

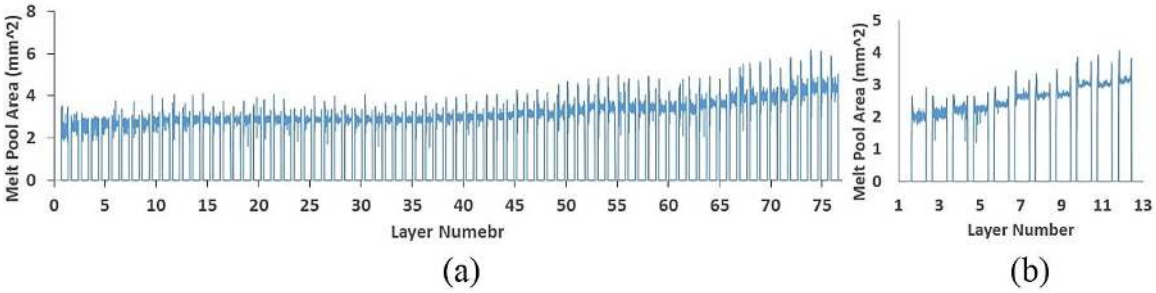

Figure 2.7 Variation of melt pool size as a function of number of layers. (a) thin-walled coupon; (b) block coupon.

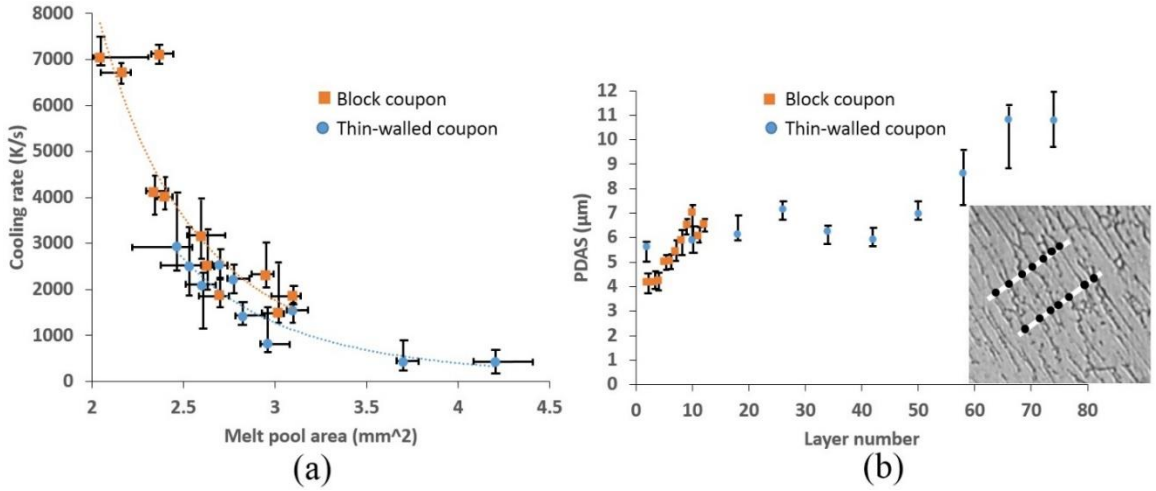

Figure 2.8 The variations of cooling rate vs melt pool area during the process; (b) PDAS as a function of number of layers.

The results show that as the melt pool became larger by increasing the number of layers, the cooling rate slowed down in both coupon types (Fig. 2.8(a)). The block coupon experienced higher cooling rates (approx. 1500 K/s to 7000 K/s), corresponding to the melt pool areas ranging from 2 mm^2 to 3 mm^2. As for the thin-walled case, lower cooling rates (approx. 400 K/s to 3000 K/s) caused relatively larger melt pool areas (ranging from about

2.5 mm^2 to 4.5 mm^2). The calculated cooling rates was in agreement with the reported range of cooling rates for the laser metal deposited parts, which is 10-10^5 K/s, according to Wang et al. [34]. A curve was also best fit to the scattered data of each coupon (see graph in Fig. 2.8(a)). The Equations of the both curves showed that the cooling rate scales inversely with the power of approximately 4 of the melt pool area as follows:

$$\dot{T} = \frac{K}{(A_{mp})^4} \tag{2.2}$$

where A_{mp} is the melt pool area (mm^2) and K is a constant to be calibrated based on the process parameters, part geometry, and the process conditions. This relation suggests that by controlling the melt pool size in real-time, one can determine the cooling rate and; thereby, the final microstructural scale of the material. This method evidently allows the laser/wire direct metal deposition system to build the parts with a uniform and very fine microstructure over the entire build.

This method is also similar to the work implemented by Homeister et al. [35].They found that in the LENS® process, the cooling rate at the solidifying surface of melt pool has a reverse relation to the square of pool length regardless of travel speed and laser power. Therefore, the measurement of melt pool length can be applied to adjust the laser power in real-time to achieve a desirable cooling rate and solidification structure.

The analysis on the chemical composition of the LW-DMD samples was also performed by using SEM-energy dispersive spectroscopy (EDS). The analysis was carried out on 4 points at each sample that are displayed in Figs. 2.3(h) and 2.4(h) and the corresponding EDS results are illustrated in Fig. 2.9.

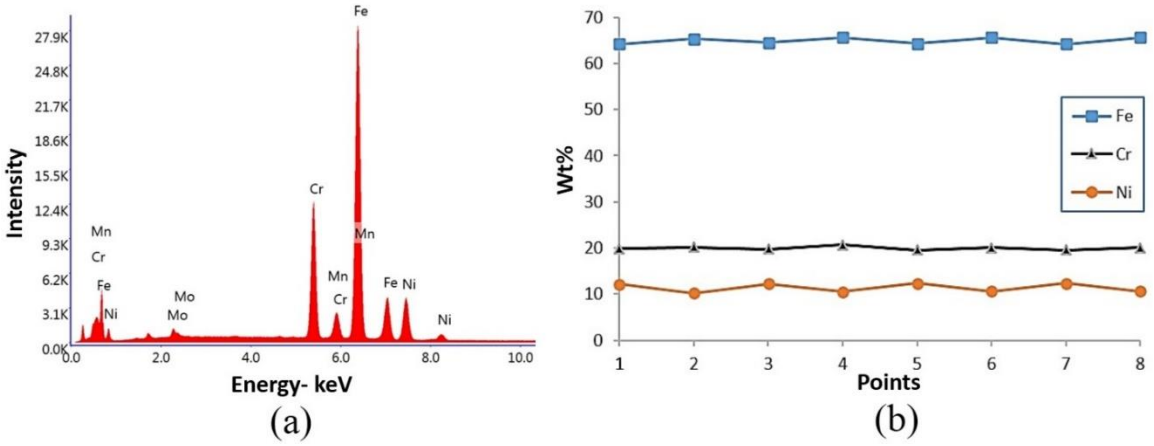

Figure 2.9 EDS spectrum. (a) First point in Fig. 3(h); and (b) the variation of main elements of all spots.

Fig. 2.9(a) indicates the EDS spectrum of the point 1 in Fig. 2.3(h). For all measured points, the discrepancies in the content of primary elements Ni, Cr, and Fe are plotted in Fig. 2.9(b) in order to study the microsegregation in the solidification process. It can be seen from Fig. 2.9(b) that there is a slight variation in element composition of different points, especially in Ni content. The Ni content at points 1, 3, 5 and 7 that were located at inter-dendritic locations was about 2% more than at points 2, 4, 6 and 8 that were located at the dendritic features. These data justified the existence of austenite as the primary phase at the inter-dendritic areas as well as ferrite at dendritic locations.

Fig. 2.10 shows the X-ray diffraction data of both block and thin-walled samples. It is clear from the graphs that both coupon types had very similar XRD pattern, consisting of δ ferrite and γ austenite phases. Zhang et al. [23] observed fully austenitic 316 stainless steel parts fabricated by laser metal deposition. Also, Elmer et al. [36] proved that for the ratio of Cr/Ni less than 1.5, the single-phase austenite is achievable at high cooling rates when the diffusibility of the solutes lowers. In this study, the Cr/Ni ratio was more than

1.5; therefore, a ferritic-austenitic microstructure achieved from X-ray diffraction was confirmed.

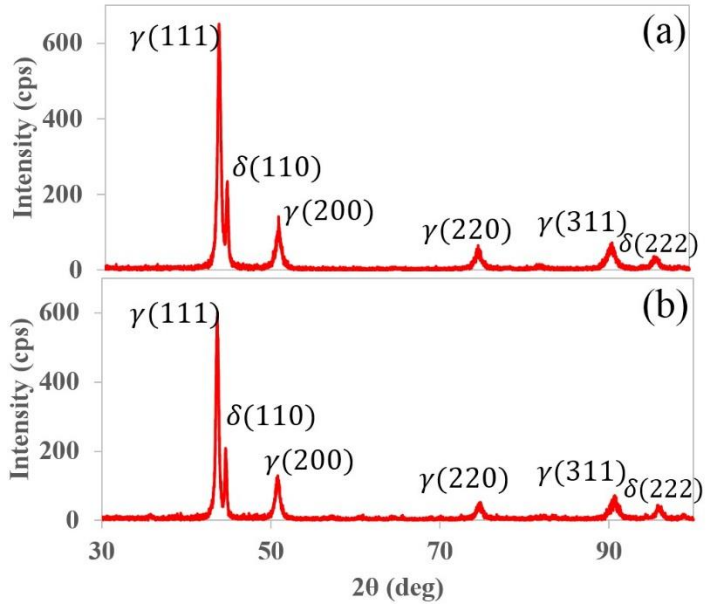

Figure 2.10 X-ray diffraction patterns of the as-built 316LSi parts. (a) Thin-walled coupon; (b) block coupon.

2.3.2 Tensile properties

The tensile properties of SS316LSi fabricated by a robotized laser/wire direct metal deposition system were evaluated. Tension tests were conducted on the standard ASTM E8 [37] samples that were taken out from thin-walled and block coupons. In each coupon type, two sets of tensile samples were prepared, one set in the direction of deposition and the other normal to the deposition direction. Fig. 2.11 (a) depicts the stress-strain curves for different conditions. The error bars represent the ranges of the UTS and elongation to failure for each sample set. The direction of tensile samples, their dimensions and the broken samples are also shown in the Fig. 2.11.

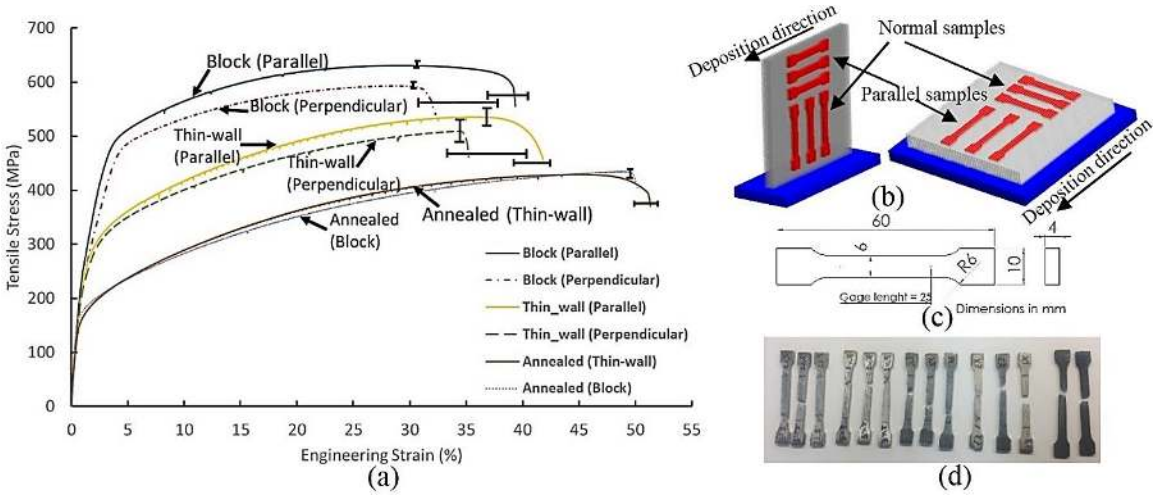

Figure 2.11 (a) Stress-strain curves of SS316LSi specimens fabricated by laser wire direct metal deposition; (b) configuration of tensile samples showing their orientations; (c) standard ASTM E8 tensile sample; (d) broken tensile specimens after testing.

The yield strength (YS), ultimate tensile strength (UTS) and elongation to failure are also listed in Table 2.3. These parameters are compared with the wrought material [38] and L-DMD buildup of SS316L parts [39].

Table 2.3 Mechanical tensile test results for as-built SS316LSi parts by LW-DMD, wrought material [38] and L-DMD parts [39].

Process	Material	Specimen orientation	Inter-layer time interval (s)	Yield strength (MPa)	Ultimate tensile strength (MPa)	Elongation (%)
LW-DMD	SS 316LSi	B*-Parallel	420s	430-440	629-635	36-40
LW-DMD	SS 316LSi	B-Perp.	420s	415-425	593-600	30-37
LW-DMD	SS 316LSi	TW*-Parallel	25s	260-300	516-546	39-42
LW-DMD	SS 316LSi	TW-Perp.	25s	220-270	484-522	32-40
LW-DMD	SS 316LSi-Annealed	B/TW-Perp./Parallel	420s/25s	160-170	430-435	50-52
Wrought-cold finished[38]	SS 316L	N/A	N/A	255-310	525-623	30
Laser consolidation [39]	SS 316L	N/A	N/A	330-365	540-560	35-43

**** B and TW represent block and thin-walled coupons, respectively.***

As declared in stress-strain curve diagram, the tensile specimens taken from the block structures (regardless of orientation: parallel or perpendicular) showed higher ultimate strength (UTS) and yield strength in comparison with those taken from thin-walled buildups. This result could obviously reveal the effect of the thermal history being experienced by parts over the process. Under the same process variables such as laser power, travel speed, and similar part geometry, it could be said that the inter-layer time interval is a decisive factor on the thermal history. It should be noted that the inter-layer time interval for block was 420 s; whereas, for the thin-walled it was 25 s. In the blocks with higher inter-layer times, the initial temperatures of the previously-deposited layers are considerably lower than those of the thin-walled coupons. In fact, colder layers are indicators of higher cooling rates resulting in finer microstructures that eventually contributed to the higher UTS and YS. Moreover, a smaller range of UTS and YS for

specimens from the block structure (see Table 2.3) might be attributed to its more uniform and consistent microstructure (approx. 1-2% change in YS and UTS for block and about 10-20% change for thin-walled). In contrast, the wider range of UTS and YS for the thin-walled structure may be related to the fact that the saturated heat and re-melting of the significant portion of the previous layer made the thermal cycles and melt pool dynamics more complicated. An inconsistent microstructure and mechanical properties were produced throughout the buildup. However, no significant changes were seen in the values of elongation between block-parallel and thin wall-parallel samples as well as between the block-perpendicular and thin wall-perpendicular samples. This revealed the higher impact of thermal history on UTS and yield strength rather than elongation. The tensile behavior of LW-DMD parts was also ascertained under different orientations with respect to the deposition direction. Two sets of specimens, one parallel to the deposition direction and the other perpendicular to the deposition direction were tested. As illustrated in Fig. 2.11(a) in the block coupon, the samples in the parallel direction exhibited a higher value of UTS and YS compared to the perpendicular samples. Similarly, in the thin-walled structure, the samples in the parallel orientation indicated higher UTS than those in perpendicular direction. It is also clear from Fig. 2.11(a) that samples in the perpendicular direction tend to behave less ductile in comparison with parallel specimens. Lower values of elongations and UTS for samples in perpendicular direction is mainly attributed to the weaker metallurgical bonding and existence of defects such as inter-layers/beads pores caused by lack of fusion [24]. This type of porosity could limit the ductility. The porosity existed mostly in thin flat shapes perpendicular to the building direction. Also, the sharp angle in the lack-of-fusion pores caused local stress concentrations under tensile loading. Therefore,

these types of defects have been proven to be the major sources of early fracture especially in samples perpendicular to the deposition direction, as reported similarly in [40]. It has also been reported that the improved tensile properties in the parallel direction is due to the fact that beads act as a reinforced fibers [41].

The heat-treated samples under annealed conditions were also tested and the tensile test results can be seen in Fig. 2.11(a). As expected, the annealing process completely altered the behavior of material and made it softer and more ductile. At annealing temperatures, the secondary phases are completely dissolved and homogenized. The residual stress is reduced to an acceptable level. Moreover, high temperature during the annealing process increased the grain size, leading to fewer grain boundaries. Grain boundaries are barriers to slip deformation because of the dislocations providing resistance to plastic deformation. Fewer grain boundaries resulted in decreasing the strength of the structure. The mechanical properties of heat-treated samples in this study are very close to the UTS and YS of 316L provided by ASM standard which is 480 MPa and 170 MPa, respectively [38]. Therefore, the annealing procedure of converting the grains from elongated shapes, dictated by solidification direction in laser metal deposition, to the granular shape will significantly mitigate the effect of orientation on the tensile properties. This is also evident from Fig. 2.11(a), in which there was no difference between the UTS and elongation of parallel and perpendicular samples in the annealed condition.

The tensile test fracture surfaces were also obtained by using a SEM and are presented in Fig. 2.12. All samples showed a typical form of ductile fracture mode with dimples. Fig. 2.12(a) and (b) showed a typical fracture surface of thin-walled and block structures, respectively. A large number of dimples and in some locations small dimples

inside the larger dimples were found, justifying the ductile mode of fracture in all specimens. It is reported that in austenitic stainless steels the weaker bonding between austenitic and δ-ferritic phases caused the crack formation. The cracks expanded at the interface and then separate into the two phases and eventually form the dimples [42]. Moreover, the existence of some torn belts in the fracture surface of thin-walled samples (Fig. 2.12(a)) is associated with the existence of many columnar dendrites in the direction of loading. The whole fracture surface of all samples was also observed. No indication of pores or defects was found except for the tensile specimen taken from the block structure in perpendicular orientation as shown in Fig. 2.12(c). Two relatively large pores that were originally formed as a result of lack-of-fusion at interface of beads/layers are presented. These pores subsequently were enlarged under tensile loading as is obvious in Fig. 2.12(c).

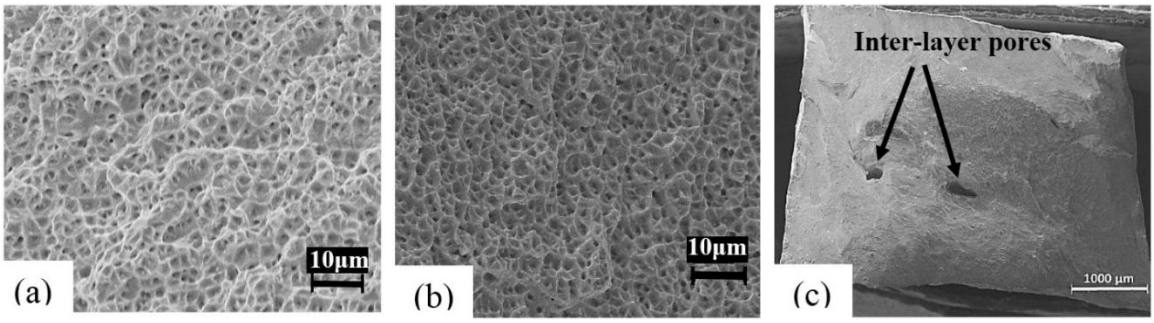

Figure 2.12 Tensile fracture surfaces. (a) in high magnification show ductile fracture mode with dimples for thin-walled; (b) in high magnification show ductile fracture mode with dimples for block; (c) and existence of inter-layer pores caused by lack-of-fusion for specimen in the perpendicular directionfrom block coupon.

2.3.3 Microstructure-tensile properties relation

As it is obvious from the stress-strain curves (Fig. 2.11(a)), there is a clear difference between the UTS, YS and elongation to failure of block, thin-wall, and heat-

treated samples. In general, samples from block structures showed higher UTS and YS and lower elongation to failure with respect to those from thin-wall structure. Similarly, samples from thin-wall indicated higher UTS and YS but lower elongation to failure compared to heat-treated ones. From microstructural analysis, we have found that the grain size ranged from 4 µm to 7µm in the block structure, from 5 µm to 12 µm in the thin-wall, and from 20 µm to 80 µm in the heat-treated samples. Based on the grain size measurement from tensile results, we can conclude that the finer microstructure (e.g., in block) corresponded to relatively higher value of UTS and YS. In contrast, larger grain size resulted in lower UTS and YS in the thin-wall structure. Moreover, the annealing which caused grain refinement and an increase in grain size, corresponded to significant lower value of UTS and YS but higher elongation to failure.

2.3.4 Microhardness

Vickers microhardness measurements were obtained along the vertical direction of block and thin-walled coupons. This experiment was conducted to specify the influence of inter-layer time interval on the hardness of as-built parts. The results of the microhardness measurements are plotted in Fig. 2.13(a). Each data point in the plot was obtained by averaging the results of three measurement points. The hardness data are plotted as a function of distance, starting from the bottom of the buildups. Due to the difference between the total height of the block and thin-walled coupons, the result of each coupon is plotted as a function of its own height distance separately. As can be seen from Fig. 2.13(a), hardness of the block coupon is apparently higher than the thin-walled, revealing the effect of thermal history (i.e., inter-layer time interval) on microhardness. In the block with a higher inter-layer time, finer microstructure caused the higher value of Vickers

hardness. The average microhardness values for block and thin-walled are 226 and 216 HV, respectively. The obtained values of microhardness are comparable with the microhardness of standard commercially-available 316L stainless steel, which is 215-225 HV [43]. It should be noted that the microhardness values are uniformly distributed along the building direction with a slight increase at the first layer of deposition. This increase was attributed to the higher heat transfer rate (high heat sink) to the cold substrate. Also, there exist some variations in the profile of microhardness for both coupon types. These variations might be attributed to the location of indentations. Fig. 2.13(b) shows a few indentations on the block sample in which some of them are located near or at the layer boundaries where the local cooling rate might slightly differ. Hence, a small variations in microhardness due to location of indentations is inevitable. The other processing parameters might also affect the hardness of material as reported in literature. For instance, Majumder et al. [44] studied the effects of laser power and travel speed on hardness and found that microhardness value of the as-built material reduced with the rise in the laser power and reduction in the travel speed. Investigating the effects of these processing variables on the hardness of buildups was out of the scope of this study.

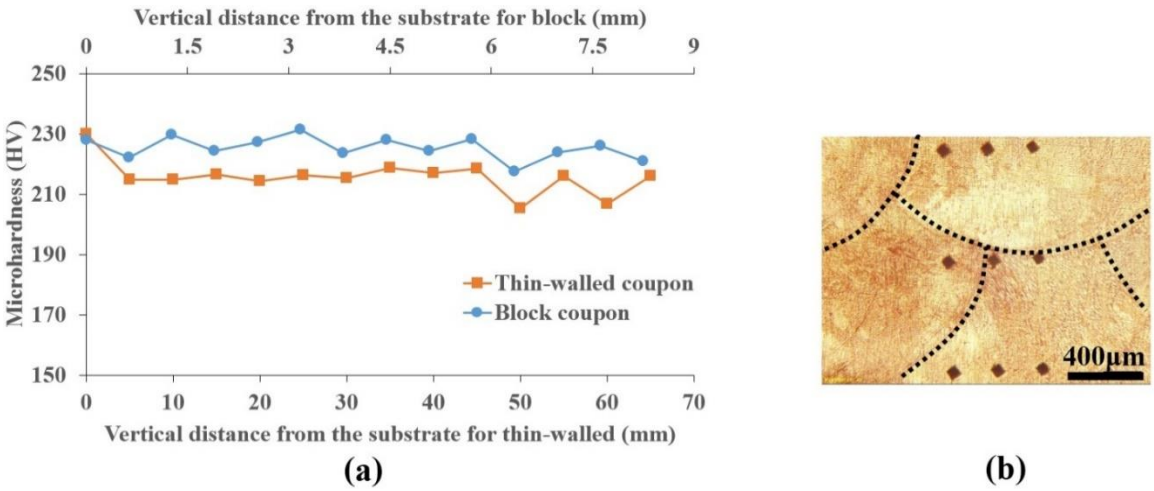

Figure 2.13 (a) Hardness distribution along height direction for both thin-walled and block samples; (b) optical micrograph of block sample showing the location of some of indentations.

2.3.5 Porosity

Porosity is considered as one of the drawbacks of additively manufactured parts. Many researchers have made efforts in studying the source of process-induced defects that cause the formation of pores and voids. The majority of these works were dedicated to LENS®- produced components [45-48]. Generally, there are three types of porosity in as-deposited powder-fed parts in terms of source of creation. Porosity is due to the lack of fusion, entrapment of gas, and porous powder. Lack of fusion (LoF) defects are formed mainly due to the insufficient energy input (i.e., laser power) to fully melt the material [45, 46]. In this case, the proper adjustment of the processing parameters such as laser power, travel speed and degree of overlap could mitigate the existence of unmelted material or LoF. The LoF porosity exists at interfacial boundaries of the beads or layers. Another common type of porosity, which is due to the gas entrapment, is formed because the LENS® process utilizes a gas (mostly Argon) as the carrier gas to assist the metal powder

transfer to the melt pool. Shielding gas protects the melt pool from oxidation, and thus it eventually promotes the gas entrapment inside the buildup [47]. This type of porosity appears at intralayer of the deposition in a spherical shape. Generally, this porosity does not form at a specific location. Moreover, the interaction of metallic powders and stability of powder flow are correlated with intralayer pores [46]. Another type of porosity comes from inherent pores inside the powder particles that were formed during the gas atomization process. These pores were reported as a potential source of intralayer porosity in the LENS® process [47, 48]. All aforementioned porosity types act as stress-raisers that can nucleate under loading and finally grow with increasing local plastic deformation. Subsequently, voids start interacting that lead to an increase in the porosity volume fraction. Finally, local necking and failure occur [49].

In the LW-DMD process, it was found that the main source of pores was the LoF at the inter-layer/bead boundaries as shown in Fig. 2.14. Su et al. [50] and Oliari et al. [51] showed that the main defect type in laser wire deposition is inter-layer pores that are produced due to the insufficient laser power or inappropriate setting of vertical overlap between layers. This type of porosity was observed in the first layers of deposition. The porosity could be attributed to the high heat transfer rate at the initial layers when the substrate is still cold. This was more obvious in block coupon where the cooling rates was higher. As it is clear from Figs. 2.14(a) - (e), by increasing the number of layers, as the cooling rate decreases, the density of pores was reduced significantly in both coupons. The pores were observed in elongated shapes with very sharp edges that typically result in high local stress. Also, pores ranged from 50µm to 200µm in both coupons. The LoF pores might have large impact on weakening the tensile properties of the samples in the

perpendicular direction as discussed earlier. Another type of porosity observed in the microstructure of LW-DMD coupons was microvoids with the size of less than 1µm (see Figs. 2.3(h) and 2.4(h)). The existence of such microvoids is the consequence of shrinkage from solidification [52]. During the phase change from liquid to solid, similar to welding process, microvoids could be nucleated and grown.

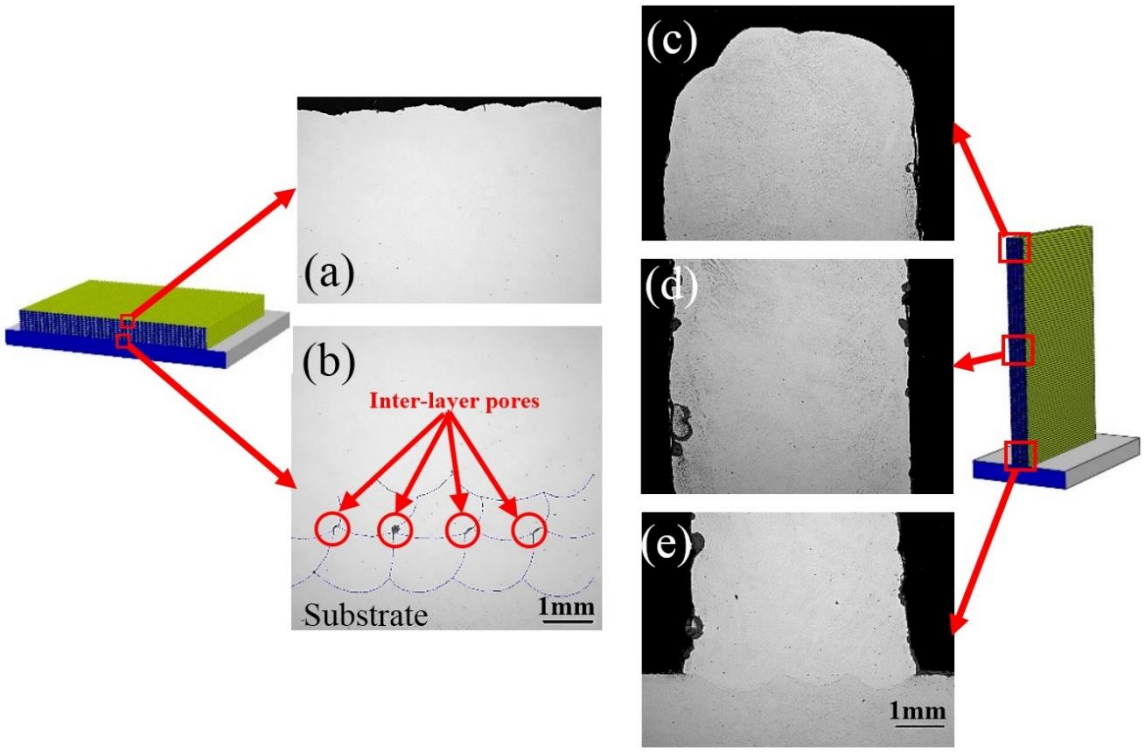

Figure 2.14 SEM micrographs showing porosity distribution across the coupons. (a) Top and (b) lower part of the block coupon; (c) top; (d) middle and (e) lower part of the thin-walled coupon.

2.4 Conclusions

In this paper, characterization of microstructure and mechanical properties of two coupon types, thin-walled and block, have been performed. Based on the achieved results, the following conclusions can be drawn:

1- Columnar dendritic was the dominant grain morphology in microstructure of both coupons. The shorter inter-layer time interval in thin-walled coupon caused a decrease in cooling rate, resulting in a coarser grain size and lower UTS. It was also found that the size of the grains were increased from bottom to top of each layer due to an increase in the cooling rates. Block sample showed relatively finer and more uniform microstructure because of the more uniform thermal history.

2- An empirical relationship correlating the cooling rate to the melt pool area was established. The relation suggested that cooling rate inversely scales with the power of 4 of melt pool area in both coupon types. That is, by applying a real-time monitoring of melt pool and a closed loop control system, one can control the solidification microstructure of the buildup.

3- The tensile results indicated that the samples parallel to the deposition direction had higher UTS and elongation to failure in both coupon types compared to those in normal direction.

4- The results of microhardness test showed the higher values for block coupon. The porosity analysis also revealed that the main source of imperfection was lack-of-fusion existing mostly in the first layers of deposition.

REFERENCES

[1] A. Uriondo, M. Esperon-Miguez, S. Perinpanayagam, The present and future of additive manufacturing in the aerospace sector: A review of important aspects, Proceedings Of The Institution Of Mechanical Engineers, Part G: Journal Of Aerospace Engineering. 229 (2015) 2132-2147.

[2] Additive Manufacturing—General Principles—Terminology; ISO/ASTM 52900; International Organization for Standardization: Geneva, Switzerland, 2015.

[3] D. Hu, R. Kovacevic, Sensing, modeling and control for laser-based additive manufacturing, International Journal Of Machine Tools And Manufacture. 43 (2003) 51-60.

[4] R. Mahamood, E. Akinlabi, Laser metal deposition of functionally graded Ti6Al4V/TiC, Materials & Design. 84 (2015) 402-410.

[5] J. Wilson, C. Piya, Y. Shin, F. Zhao, K. Ramani, Remanufacturing of turbine blades by laser direct deposition with its energy and environmental impact analysis, Journal Of Cleaner Production. 80 (2014) 170-178.

[6] Y. Ding, M. Akbari, X.L. Gao, L. Ai, R. Kovacevic, 3 Use of Powder-Feed Metal Additive Manufacturing System for Fabricating Metallic Metamaterials, in: T.S. Srivatsan,

T.S. Sudarshan, K., Manufacturing Techniques for Materials: Engineering and Engineered, CRC Press, 2018, pp. 51-65

[7] R. Aman, R. Hurley, Can Metal Additive Manufacturing Compete with Casting?, retrieved from (EWI website): https://marketing.ewi.org/acton/attachment/12956/f-03c0/1/-/-/-/-/ , 2017

[8] M. Akbari, Y. Ding, R. Kovacevic, Process Development for a Robotized Laser Wire Additive Manufacturing. In ASME 2017 12th International Manufacturing Science and Engineering Conference collocated with the JSME/ASME 2017 6th International Conference on Materials and Processing (pp. V002T01A015-V002T01A015). American Society of Mechanical Engineers.

[9] L. Song, V. Bagavath-Singh, B. Dutta, J. Mazumder, Control of melt pool temperature and deposition height during direct metal deposition process, The International Journal Of Advanced Manufacturing Technology. 58 (2011) 247-256.

[10] A. Heralić, A. Christiansson, M. Ottosson, B. Lennartson, Increased stability in laser metal wire deposition through feedback from optical measurements, Optics And Lasers In Engineering. 48 (2010) 478-485.

[11] A. Heralić, A. Christiansson, B. Lennartson, Height control of laser metal-wire deposition based on iterative learning control and 3D scanning, Optics And Lasers In Engineering. 50 (2012) 1230-1241.

[12] Y. Ding, J. Warton, R. Kovacevic, Development of sensing and control system for robotized laser-based direct metal addition system, Additive Manufacturing. 10 (2016) 24-35.

[13] W. Syed, L. Li, Effects of wire feeding direction and location in multiple layer diode laser direct metal deposition, Applied Surface Science. 248 (2005) 518-524.

[14] Y. Ding, M. Akbari, R. Kovacevic, Process planning for laser wire-feed metal additive manufacturing system, The International Journal Of Advanced Manufacturing Technology. 95 (2017) 355-365.

[15] W. Frazier, Metal Additive Manufacturing: A Review, Journal Of Materials Engineering And Performance. 23 (2014) 1917-1928.

[16] Herderick, E. "Additive manufacturing of metals: A review." Materials Science and Technology MS (2011): 1413.

[17] N. Shamsaei, A. Yadollahi, L. Bian, S. Thompson, An overview of Direct Laser Deposition for additive manufacturing; Part II: Mechanical behavior, process parameter optimization and control, Additive Manufacturing. 8 (2015) 12-35.

[18] A. Yadollahi, N. Shamsaei, S. Thompson, D. Seely, Effects of process time interval and heat treatment on the mechanical and microstructural properties of direct laser deposited 316L stainless steel, Materials Science And Engineering: A. 644 (2015) 171-183.

[19] J. Su, M. Xiao, Z. Zhang, Z. Ye, X. Jin, Y. Yang, Microstructural morphology and evolution of austenite stainless steel deposited using pulsed laser and wire. The International Journal of Advanced Manufacturing Technology 93.9-12 (2017) 3357-3370.

[20] J. Lewandowski, M. Seifi, Metal Additive Manufacturing: A Review of Mechanical Properties, Annual Review Of Materials Research. 46 (2016) 151-186.

[21] B. Carroll, T. Palmer, A. Beese, Anisotropic tensile behavior of Ti–6Al–4V components fabricated with directed energy deposition additive manufacturing, Acta Materialia. 87 (2015) 309-320.

[22] B. Zheng, Y. Zhou, J. Smugeresky, J. Schoenung, E. Lavernia, Thermal Behavior and Microstructure Evolution during Laser Deposition with Laser-Engineered Net Shaping: Part II. Experimental Investigation and Discussion, Metallurgical And Materials Transactions A. 39 (2008) 2237-2245.

[23] K. Zhang, S. Wang, W. Liu, X. Shang, Characterization of stainless steel parts by Laser Metal Deposition Shaping, Materials & Design. 55 (2014) 104-119.

[24] X. Xu, G. Mi, Y. Luo, P. Jiang, X. Shao, C. Wang, Morphologies, microstructures, and mechanical properties of samples produced using laser metal deposition with 316 L stainless steel wire, Optics And Lasers In Engineering. 94 (2017) 1-11.

[25] I. Bernstein, D. Peckner, Handbook of stainless steels, Central Book Co, Taipei, 1977.

[26] B. Zheng, Y. Zhou, J. Smugeresky, J. Schoenung, E. Lavernia, Thermal Behavior and Microstructural Evolution during Laser Deposition with Laser-Engineered Net Shaping:

Part I. Numerical Calculations, Metallurgical And Materials Transactions A. 39 (2008) 2228-2236.

[27] L. Costa, R. Vilar, T. Reti, A. Deus, Rapid tooling by laser powder deposition: Process simulation using finite element analysis, Acta Materialia. 53 (2005) 3987-3999.

[28] V. Manvatkar, A. Gokhale, G. Jagan Reddy, A. Venkataramana, A. De, Estimation of Melt Pool Dimensions, Thermal Cycle, and Hardness Distribution in the Laser-Engineered Net Shaping Process of Austenitic Stainless Steel, Metallurgical And Materials Transactions A. 42 (2011) 4080-4087.

[29] ASM Handbook, Heat treating, A S M International, Materials Park, vol, 4, p.744, 1991.

[30] W. Kurz, B. Giovanola, R. Trivedi, Theory of microstructural development during rapid solidification, Acta Metallurgica. 34 (1986) 823-830.

[31] T. DebRoy, H.L. Wei, J.S. Zuback, T. Mukherjee, J.W. Elmer, J.O. Milewski, A.M. Beese, A. Wilson-Heid, A. De, W. Zhang, Additive manufacturing of metallic components – Process, structure and properties, Progress in Materials Science 92 (2018) 112–224.

[32] D. Hu, R. Kovacevic, Modelling and measuring the thermal behaviour of the molten pool in closed-loop controlled laser-based additive manufacturing, Proceedings of the Institution of Mechanical Engineers, Part B: Journal of Engineering Manufacture 217.4 (2003) 441-452.

[33] S. Kou, Welding metallurgy, John Wiley & Sons. 2003

[34] L. Wang, S. Felicelli, Y. Gooroochurn, P. Wang, M. Horstemeyer, Optimization of the LENS® process for steady molten pool size, Materials Science And Engineering: A. 474 (2008) 148-156.

[35] W. Hofmeister, M. Griffith, Solidification in direct metal deposition by LENS processing, JOM. 53 (2001) 30-34.

[36] J. Elmer, S. Allen, T. Eagar, Microstructural development during solidification of stainless steel alloys, Metallurgical Transactions A. 20 (1989) 2117-2131.

[37] ASTM E8/E8M - 09 Standard Test Methods for Tension Testing of Metallic Materials, ASTM, West Conshohocken, PA, 2009.

[38] J. Davis, Stainless steels, ASM international, Materials Park, Ohio, 1994.

[39] L. Costa, R. Vilar, Laser powder deposition, Rapid Prototyping Journal. 15 (2009) 264-279.

[40] T. Vilaro, C. Colin, J. Bartout, As-Fabricated and Heat-Treated Microstructures of the Ti-6Al-4V Alloy Processed by Selective Laser Melting, Metallurgical And Materials Transactions A. 42 (2011) 3190-3199.

[41] P. Guo, B. Zou, C. Huang, H. Gao, Study on microstructure, mechanical properties and machinability of efficiently additive manufactured AISI 316L stainless steel by high-power direct laser deposition, Journal Of Materials Processing Technology. 240 (2017) 12-22.

[42] K. Li, D. Li, D. Liu, G. Pei, L. Sun, Microstructure evolution and mechanical properties of multiple-layer laser cladding coating of 308L stainless steel, Applied Surface Science. 340 (2015) 143-150.

[43] K.M. Zwilsky, Handbook, A.S.M., Volume 1: Properties and Selection: Irons. Steels, and High-Performance Alloys, ASM Handb, 2071. 1993

[44] J. Dutta Majumdar, A. Pinkerton, Z. Liu, I. Manna, L. Li, Mechanical and electrochemical properties of multiple-layer diode laser cladding of 316L stainless steel, Applied Surface Science. 247 (2005) 373-377.

[45] R.M. Mahamood, E.T. Akinlabi, M. Shukla. S. Pityana, Characterizing the Effect of Processing Parameters on the Porosity of Laser Deposited Titanium Alloy Powder. In Proceedings of the International MultiConference of Engineers and Computer Scientists 2 (2014)

[46] L. Wang, P. Pratt, S.D. Felicelli, H. El Kadiri, J.T. Berry, P.T. Wang, M.F. Horstemeyer, Experimental analysis of porosity formation in laser-assisted powder deposition process. In 2009 TMS Annual Meeting & Exhibition.

[47] M. Ahsan, R. Bradley, A. Pinkerton, Microcomputed tomography analysis of intralayer porosity generation in laser direct metal deposition and its causes, Journal Of Laser Applications. 23 (2011) 022009.

[48] D. Susan, J. Puskar, J. Brooks, C. Robino, Quantitative characterization of porosity in stainless steel LENS powders and deposits, Materials Characterization. 57 (2006) 36-43.

[49] G. Sun, R. Zhou, J. Lu, J. Mazumder, Evaluation of defect density, microstructure, residual stress, elastic modulus, hardness and strength of laser-deposited AISI 4340 steel, Acta Materialia. 84 (2015) 172-189.

[50] J. Z. Su, M. Z. Xiao, Z. J. Zhang, Z. P. Ye, X. Jin, Y. C. Yang, Microstructural morphology and evolution of austenite stainless steel deposited using pulsed laser and wire, The International Journal of Advanced Manufacturing Technology 93.9-12 (2017) 3357-3370.

[51] S. H. Oliari, A. D'Oliveira, M. Schulz, Additive Manufacturing of H11 with Wire-Based Laser Metal Deposition, Soldagem & Inspeção 22.4 (2017) 466-479.

[52] D. Olson, G. Edwards, Interfacially driven mass transport in joining and coating technologies, Philosophical Transactions Of The Royal Society A: Mathematical, Physical And Engineering Sciences. 356 (1998) 927-940.

Chapter 3

JOINING OF ELEMENTS FABRICATED BY A ROBOTIZED LASER/WIRE DIRECTED ENERGY DEPOSITION PROCESS BY USING AN AUTOGENOUS LASER WELDING

3.1 Introduction

Robotized laser/wire directed energy deposition (RLW-DED) as a metal based additive manufacturing (AM) technology has been gaining attention. According to ISO/ASTM 52900:2015 [1] and ASTM F3187-16 [2], DED is defined as "an additive manufacturing process in which focused thermal energy is used to fuse materials by melting as they are being deposited." DED is accomplished by feeding of metallic powder or wire into the melt pool formed by a highly focused energy source such as laser, electron beam, or arc. For instance, Williams et al. [3] employed wire and arc to produce large titanium parts (>10 kg). They also evaluated the residual stress in the buildups. Abioye et al. [4] used laser as a heat source and Inconel wire to fabricate multi-layer coatings in order to increase the corrosion resistance of stainless steel components. They showed that the coating could well protect the parts exposed to corrosion. Brandl at al. [5] utilized laser and wire to manufacture multi-layer depositions. They characterized the microstructural properties of buildups and showed that grain dimensions at single beads can be used to qualitatively indicate microstructural and mechanical properties. Industry is noticing

DED's capability to fabricate near-net-shape metal parts with higher deposition rates. Using a low-cost welding wire as feedstock and a robot as a kinematic system provides a high flexibility to print complex geometries with dimensional accuracy within ±0.5 mm [6]. Also, some efforts have been made in RLW-DED process by means of vision system, to increase the process stability [7] and predict and control the mechanical and microstructural properties of the buildup in real-time [8]. However, there exist some limitations in printing certain parts in the DED process. For instance, a part with very complex form or intrinsic features could be difficult to fabricate even with a robotized system. In the DED process, there is no support material. This lack of support is unlike the powder bed fusion (PBF) process, in which the melt pool is always supported by the metal powder in the bed. In DED the motion system, mainly the positioning table, provides the possibility for the melt pool to get support from the previously deposited layer. However, in special cases; for example, in fabricating a part with an overhang section, the positioning table needs to be tilted in a large angle to be able to build the overhang section. Many researchers developed different methods in the DED process for fabricating the overhang parts. Zhang et al. [9] developed an adaptive slicing algorithm to build non-uniform thickness layer due to the change in the build direction. By using this technique, they were able to build the overhang parts. Dwivedi et al. [10] developed an algorithm to fabricate branching slender structures. However, adding more overhang sections or branches to the existing overhang part makes the geometry and thereby the path planning very complex. Moreover, there might be possible inaccessibility of laser head to the part and eventually a collision could happen. Therefore, segmenting part into smaller sub-parts and joining the elements back together could be a solution to deal with those limitations in the DED

process to some extent. For instance, a slender branched larger structure could be divided into several easy to print sub-parts and then joined back together. It should be noted that, in complex geometries, the part should be segmented at locations with no structurally-critical intersections.

Very few studies focused on joining of AM parts. Casalino et al. [11] studied the possibility of joining selective laser melted (SLM) parts to wrought stainless steel parts by using fiber hybrid laser-arc welding. Then they evaluated the efficiency of the welding process. Wits et al. [12] achieved good quality welds by adjusting process parameters in a laser welding of SLM titanium parts. Also, Matilainen et al. [13] investigated the weldability of SLM 316L components to cold-rolled sheet metal 316L parts in terms of the existence of pores and cracks in the weld area. However, to the authors' knowledge, no study was found in the literature that focused on joining the DED parts by using an autogenous laser welding process.

Autogenous laser welding has been used extensively in joining applications where the higher welding speed and a lower heat input are desired. Different laser types such as fiber laser, disk laser, CO_2 laser or diode laser could be used in such applications. This process can also provide a very small heat-affected zone (HAZ), low heat distortion, narrow and deep penetration, and eventually can produce joints with a high quality [14]. It is also suitable for welding of dissimilar materials with high quality joints and small HAZ [15]. Laser could also offer a better absorptivity in welding a broad range of materials. In the present investigation, a robotized laser/wire directed energy deposition system followed by an autogenous fiber laser welding were utilized to boost the flexibility of the DED process. This process is considered as a hybrid system since it combines two

processes to fabricate a part. This process broadened the range of DED applications. The main objective of this paper was to investigate the mechanical and microstructural properties of the butt welds between the DED thin-wall parts obtained by the autogenous laser welding.

3.2 Experimental procedure

3.2.1 Materials

The feedstock material used in this study was an austenitic stainless steel (316LSi) in the form of wire from ESAB with a diameter of 1.2 mm. Also, a commercially-available 304L stainless steel plate with a thickness of 6 mm was utilized as a support plate (substrate). The chemical compositions of wire and substrate are given in Table 3.1.

Table 3.1 Chemical compositions of wire and substrate.

Element (wt.%)	C	Mn	Si	Ni	Mo	Cr	Cu	P	S	Fe
Wire (316LSi)	0.01	1.8	0.9	12.2	2.60	18.4	0.12	0.03	0.03	Bal.
Substrate (304L)	0.03	2	-	8	-	18	-	0.045	0.03	Bal.

3.2.2 Methodology

A robotized laser/wire directed energy deposition system (RLW-DED) was used to fabricate the parts. Fig. 3.1 illustrates the experimental setup. A 6-axis KUKA robot (KR-60) coupled with a 2-axis rotary table was used to provide the kinematics of the deposition system. A 4 kW fiber laser with 1070 nm wavelength from IPG was utilized as a heat source. A Precitec YW50 laser welding head was mounted on the robot arm to deliver the laser beam to the processing zone. The laser beam was defocused at 10mm below the focal point, resulting in 1.6mm beam spot diameter. Also, in order to feed the wire, a Binzel wire feeding system with two synchronized push and pull motors was used. Moreover, slicing

the STL file of the 3D model and generating the toolpath and code for the robot controller were done in SKM DCAM offline programming software. The same setup without the wire feeder was used also for autogenous laser welding of the DED parts.

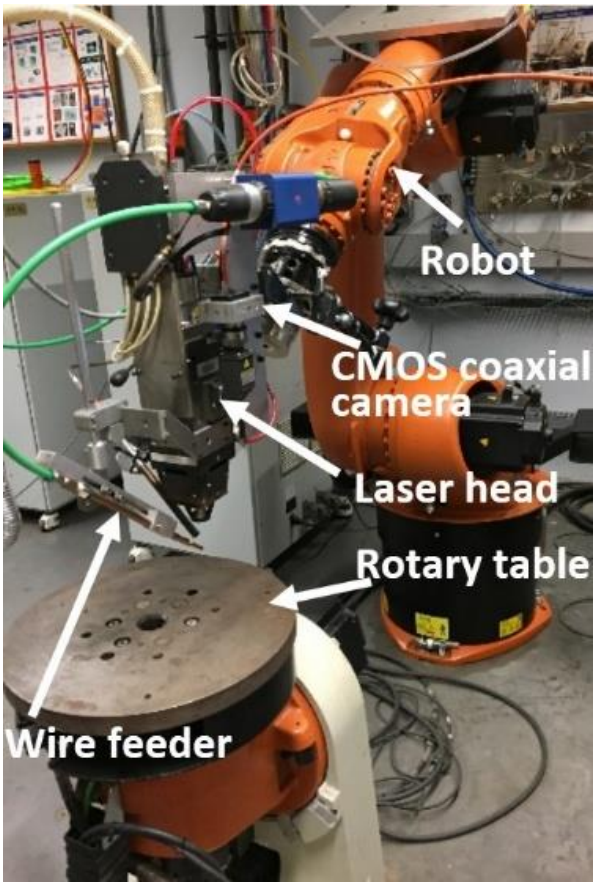

Figure 3.1 A robotized laser/wire directed energy deposition system used for DED and welding processes.

Four thin-walled coupons of the same geometry and dimensions were built by using a RLW-DED system as shown in Fig. 3.2(a). All the beads in coupons were deposited in one direction as shown in Fig 3.2 (b and c). Three beads were deposited per layer to achieve 4 mm thickness of the wall. After each track was deposited, the laser head was positioned for the next bead. The idle time to position the laser head, was kept at a low level by adjusting the robot speed at higher speed of 250 mm/s. The coupons were machined before

the welding process in order to make the DED plates with a precise and consistent thickness for butt welding, and then welded together. Fig. 3.2 (b and c) shows the configurations of welds and orientation of tensile samples with respect to joints and DED parts. Two coupons were welded together such that the tensile samples were cut out "parallel" to the direction of the DED beads in the "deposition" direction as depicted in Fig. 3.2(b). This configuration is called Weld DED-P for simplicity. Two other coupons were joined in such a way that the tensile samples were taken out "normal" to the deposition direction as indicated in Fig. 3.2(c). This configuration is referred to as Weld DED-N in the rest of this paper. In the Weld DED-N specimens, the tensile loading direction was normal to the sliced layers. The reason for considering the tensile samples in two directions was to involve the effects of inherent anisotropic mechanical behavior of the DED parts. In each type of configuration three tensile specimens were prepared. Fig. 3.2(d and e) depict the welded DED parts. In addition, two sets of samples, one normal and the other parallel to the deposition direction, were prepared from DED parts without joints. Therefore, larger buildups were necessary to meet the size of the standard tensile specimen. Two thin-walled coupons with the same size, one for making normal tensile specimens and the other for making parallel ones, were fabricated as shown in Fig. 3.3(a-c). The purpose of preparing tensile samples without a weld was to compare their tensile properties to those properties of the welded DED specimens. The tensile samples taken from the DED part without a weld were designated as DED-P and DED-N specimens; that is, those specimens in the parallel and normal direction relative to the deposition direction, respectively. The processing parameters used for the RLW-DED process and autogenous laser welding are provided in Table 3.2. The main process variables such as laser power, travel speed, wire

feed speed, Z-increment and overlap increment were optimized in the previous work [6]. The optimized process parameters provided the constant and stable deposition on the entire build. The RLW-DED was conducted in an open atmosphere, therefore, in order to achieve a successful process, it is necessary to protect the melt pool. An inert gas (Argon) was used to shield the melt pool from oxidation. Shielding could also improve the properties of deposition and eventually promote the inter-layer bonding by providing better surface wetting [16]. A side-feeding nozzle with respect to the laser head was used to feed the Argon with the flow rate of 15 l/min and 30 l/min for DED and welding processes, respectively. The parameters for the welding process were optimized by welding several dummy samples of wrought plates with 3 mm thickness. The dimensions of the tensile specimens used in this study were selected according to the ASTM E08 standard [17] as shown in Fig. 3.3(d). After welding, the tensile samples were cut out by using a waterjet cutting machine and were ground to remove the face and root of the welds.

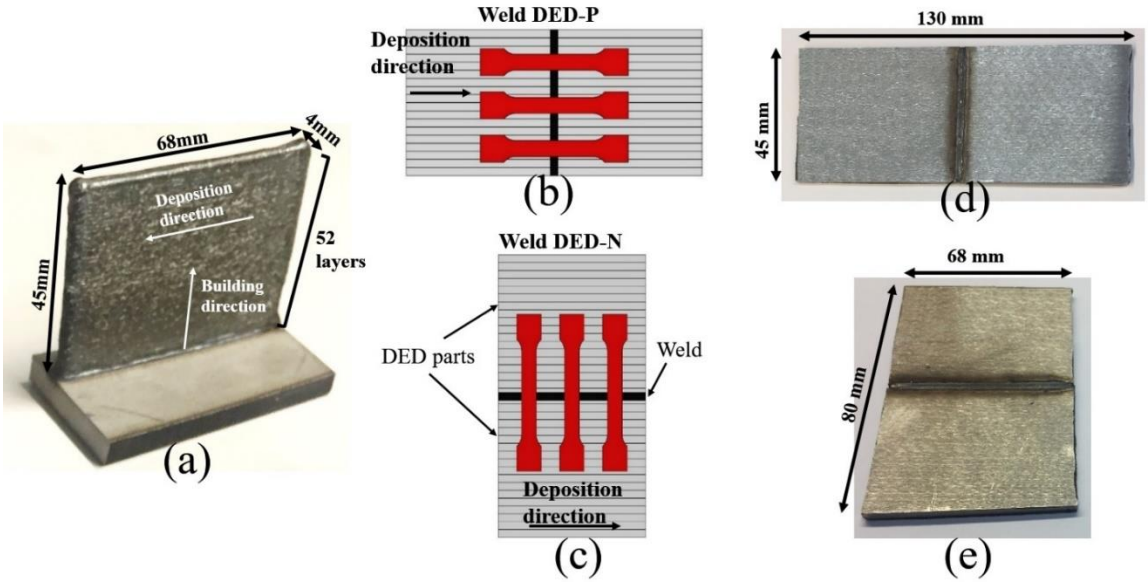

Figure 3.2 (a) As-built coupon used for welding (b) Weld DED-P sample: tensile specimens parallel to the deposition direction (c) Weld DED-N sample: tensile specimens normal to the deposition direction (d and e) welded DED parts.

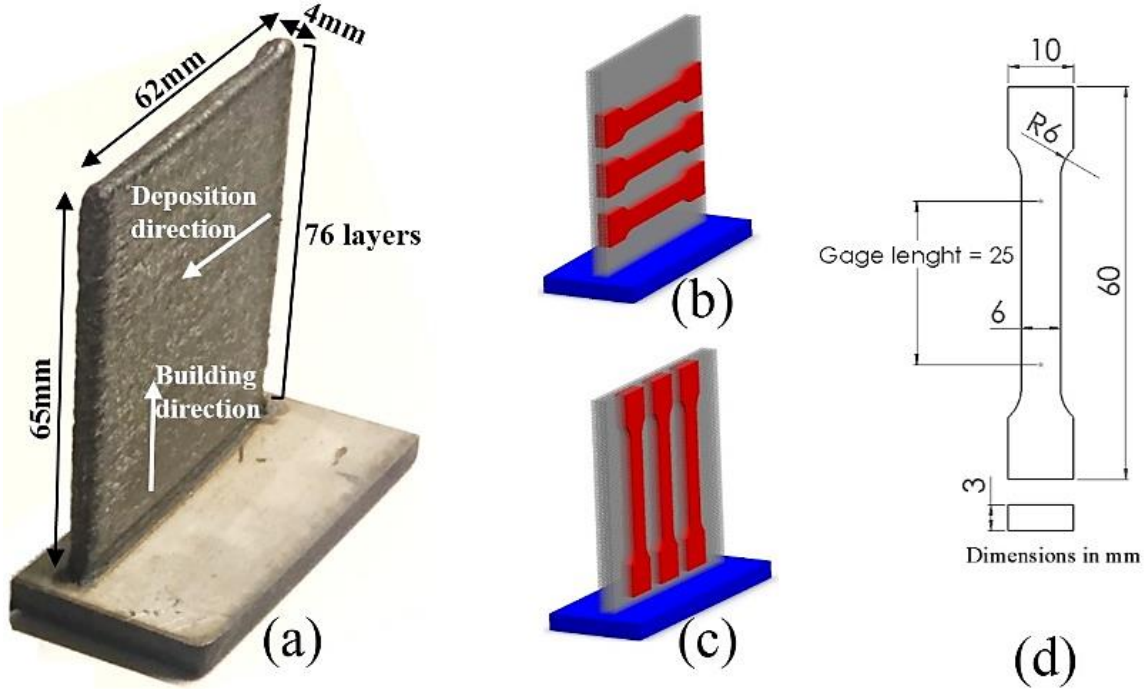

Figure 3.3 (a) As-built coupon for preparing tensile specimens without weld (b) orientation of tensile specimens in the normal direction (DED-N) (c) orientation of

tensile specimens in the parallel direction (DED-P) (d) the dimensions of the standard tensile specimen per ASTM E8 [17].

Table 3.2 Processing parameters for DED and welding.

Process	Laser Power (W)	Travel speed (mm/s)	Shielding gas flow rate (l/min)	Wire Feed Speed (mm/s)	Z-increment (mm)	overlap increment (mm)
DED	1000	8	15 (Argon)	12	0.85	1.35
Welding*	2900	30	30 (Argon)	-	-	-

* The focal point was positioned at the top surface of the plates

Tensile tests were performed on an Instron 5582 tensile test machine with 1mm/min strain rate at room temperature. In order to capture the elongation (strain) during the tensile test, the crosshead displacement of the machine was used. Also, to verify the value of elongation to failure of specimens obtained from the machine crosshead, all the specimens were marked before the test based on the gage length and after the test the broken parts were put back together to measure the elongation to failure. The cross-sections of the joints were mounted, sanded, and polished using a diamond polishing pad. Then, the samples were chemically etched in a solution of (HCL:HNO3=3:1) for 40 seconds. Microstructural analysis of the welds was conducted by using an optical microscope (Olympus DP72) and scanning electron microscopy (SEM LEO 1450) equipped with an energy dispersive spectroscopy (EDS). A Vickers microhardness tester machine (Clark-CM700) was utilized to perform microhardness measurements. A load of 1kg with the waiting time of 15 seconds were applied during microhardness test. A fracture surface analysis was also done by the same SEM.

3.3 Experimental results and discussion

3.3.1 Microstructural analysis

Figs. 3.4 and 3.5 show the cross-section microstructure of the Weld DED-N and Weld DED-P, respectively. In Figs. 3.4(a) and 3.5(a), the footprint of laser tracks are indicated. The footprint of laser tracks are indicator of border of each new track that is being deposited in the cross sectional microstructure. This could be also recognized as melt pool boundary. Butt joints with full penetration were observed. The weld zone was found to be in a "Y" shape in both coupons with the widest dimension at the crown and the narrowest at the middle of the bead section as shown in Figs. 3.4(a) and 3.5(a). Also, no HAZ was observed in the joints. This is attributed to the higher energy density and lower heat input of the laser welding process compared to arc based welding methods such as GMAW. Due to the higher cooling rates in the laser welding process compared to GTAW, there is no sufficient time for grains that are located between fusion zone (FZ) and the base plates to grow, resulting in a joint without HAZ [18]. This is considered as a good characteristic of a laser-welded joint. No noticeable cracks or inclusions were found in the fusion zone. Due to the similar nature of laser welding and laser directed energy deposition during the process of solidification, the final morphology was found to be mainly columnar dendritic in both the weld zone and DED parts as shown in Fig. 3.4(b and d). It can be seen from Fig. 3.4(b) that in the fusion zone, the dendrites were symmetrically distributed around the weld centerline. Also, dendrites were grown epitaxially from fusion boundary to the weld centerline, opposite to the heat flow direction [19]. In addition, the similar columnar dendritic structure directed from the bottom of the tracks toward the top was observed in the DED microstructure as shown in Fig. 3.4(d). The magnified views of

microstructure in the weld and DED are displayed in Fig. 3.4 (e and f) and Fig. 3.5(b). The dendritic structure is clear. The darker areas are the primary dendrite cells that were consisted of the austenite (γ) phase. The lighter area between dendrites was the skeletal δ-ferrite phase. During the solidification of the weld zones and DED of 316LSi, due to the high cooling rates associated with laser material processing, the $\delta \rightarrow \gamma$ transformation remained incomplete. Thereby, formation of the skeletal δ-ferrite in the austenitic matrix was the result [20]. Therefore, the final solidification mode of the material either in the weld zone or DED was found to be ferritic-austenitic (FA). The primary dendrite arm spacing in the weld zone for both Weld DED-N and Weld DED-P coupons was about 2.5-5 μm; whereas, this value for the DED part was about 4-10 μm. The finer dendrite size in the weld zone clearly signified relatively higher cooling rate and lower heat input in the welding process compared to those experienced in the DED process. Figs. 3.4(c) and 3.5(c) also demonstrate the fusion boundary between the DED parts and weld fusion zone. The transition in the size of grains from DED to weld was clear.

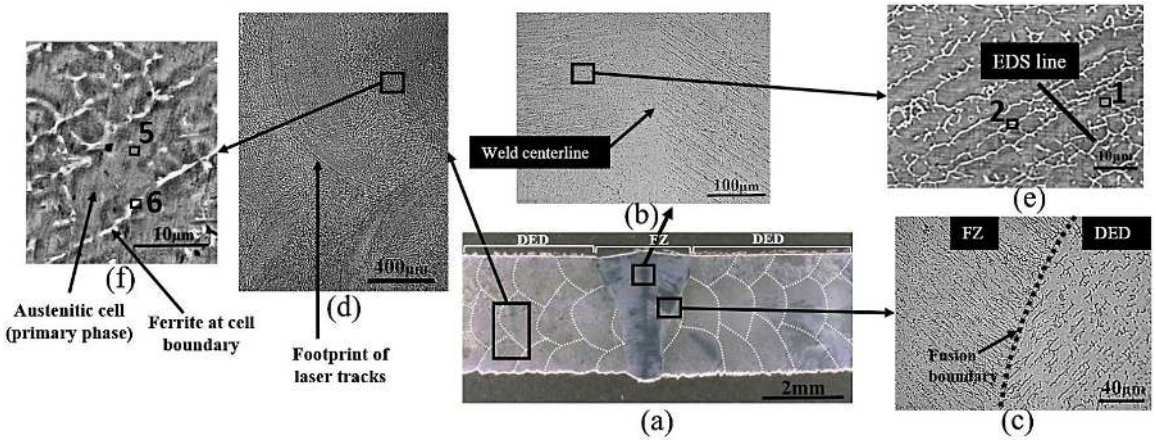

Figure 3.4 The transverse-section images of Weld DED-N sample (a) optical micrograph showing the weld zone and DED plates (b) distribution of grains around weld centerline (c) fusion boundary (d) DED microstructure (e) SEM image of the

weld zone indicating the columnar dendrites (f) SEM image of the DED indicating the columnar dendrites.

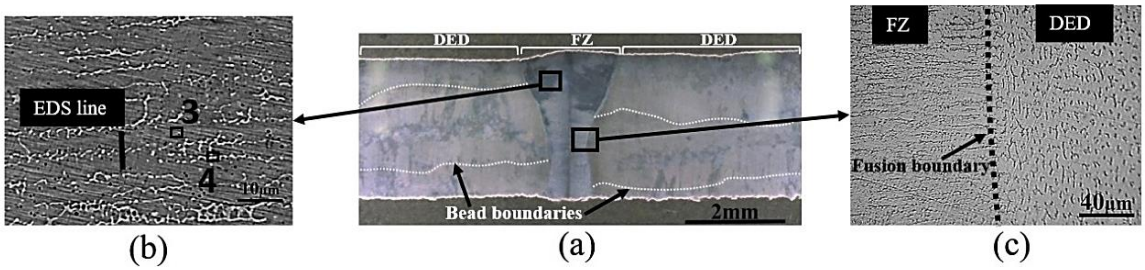

Figure 3.5 The transverse-section optical images of Weld DED-P sample (a) optical micrograph showing the weld zone and DED plates (b) SEM image of the weld zone indicating the columnar dendrites (c) fusion boundary.

In order to study the variations in distribution of elements in the weld zone and DED parts, the EDS analysis was performed, and the results are shown in Fig. 3.6 and Table 3.3. Figs. 3.6 (a and b) show the EDS scanning line for Cr and Ni elements in the weld zone of the Weld DED-N and Weld DED-P samples, respectively. The lines are shown in Fig. 3.4(e) and Fig. 3.5(b). No noticeable segregation can be seen from the EDS profiles that could increase the degree of homogeneity, mechanical properties and the pitting corrosion resistance of the austenitic stainless steel welds [21,22]. Also, the alloying elements distribution in different points located on the dendritic austenite matrix and δ-ferrite were measured as depicted in Table 3.3. In this Table, the weight content of alloying elements in DED was compared to those in the weld zone. The weight content of chrome, as expected, was slightly lower at all points in the austenitic phase both in the weld area and the DED parts. However, the Ni weight content was slightly higher in these areas. These results revealed no significant segregation. Thereby a uniform chemical composition was presented throughout the entire fusion zone and the DED parts.

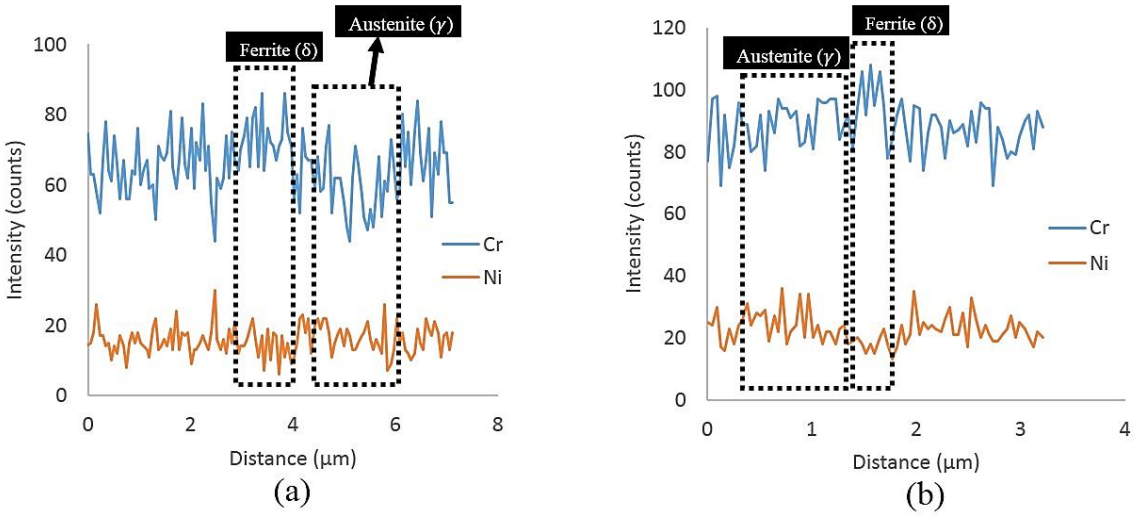

Figure 3.6 EDS line profiles of Cr and Ni elements across the phase boundaries for (a) Weld DED-N and (b) Weld DED-P coupons. The scanning lines are shown in Fig. 4(e) and 5(b).

Table 3.3 EDS chemical composition of different points across the weld zone and DED parts.

	Weld				DED	
	Point 1	**Point 2**	**Point 3**	**Point 4**	**Point 5**	**Point 6**
Element	Wt%	Wt%	Wt%	Wt%	Wt%	Wt%
Si	0.92	0.66	0.69	0.71	0.81	0.87
Mo	2.92	2.79	3.29	3.02	2.12	2.45
Cr	18.85	19.22	18.78	19.71	19.77	20.66
Fe	63.87	66.65	64.9	66.9	64.55	65.66
Ni	13.44	10.69	12.34	10.66	12.26	10.51

3.3.2 Tensile properties

Tensile testing with the standard specimen taken from the welded DED parts and DED parts (Figs. 3.2 and 3.3) were conducted to evaluate the ultimate tensile strength (UTS) and elongation to failure of the samples. The typical stress-strain curves of all

specimens are illustrated in Fig. 3.7(a). The typical broken tensile specimens are also shown in this Figure. All tensile specimens of the welded coupons were fractured in DED parts, demonstrating that the good quality welds were achieved. The average values of UTS and elongation along with their relevant error bar that indicate the range for each value are presented in Fig. 3.7(b). It can be seen from Fig. 3.7(b) that the UTS and elongation of specimens from the Weld DED-P and DED-P coupons were higher than those from the Weld DED-N and DED-N coupons. In other words, regardless of whether the tensile specimen had a joint or not, the specimen showed higher tensile properties if it was aligned parallel to the direction of deposition. These results indicated the anisotropic mechanical behavior of the DED parts. The lower UTS and ductility of specimens in the normal direction might be attributed to weaker metallurgical bonding, presence of imperfections such as inter-layers/beads pores caused by lack-of-fusion in DED parts, epitaxial grain growth during solidification and orientation of dentrites in the microstructure. The lack-of-fusion is the major source of porosity in the as-deposited parts that are usually caused by insufficient melting, mostly occurred at the layer interface [23]. Furthermore, by comparing the Weld DED-P to DED-P specimens or Weld DED-N to DED-N specimens, it can be deduced that the existence of weld joints did not have a negative effect on the tensile properties of the DED parts. In the commonly-used laser welding of wrought plates, the joints usually indicated better mechanical properties compared to the wrought base plate. This result is because the microstructure of welds changed greatly [24,25]. However, in the laser welded DED parts, the mechanical properties were not improved after welding, since the microstructure and chemical composition of the joints remained very similar to those of DED (e.g., columnar dendritic microstructure).

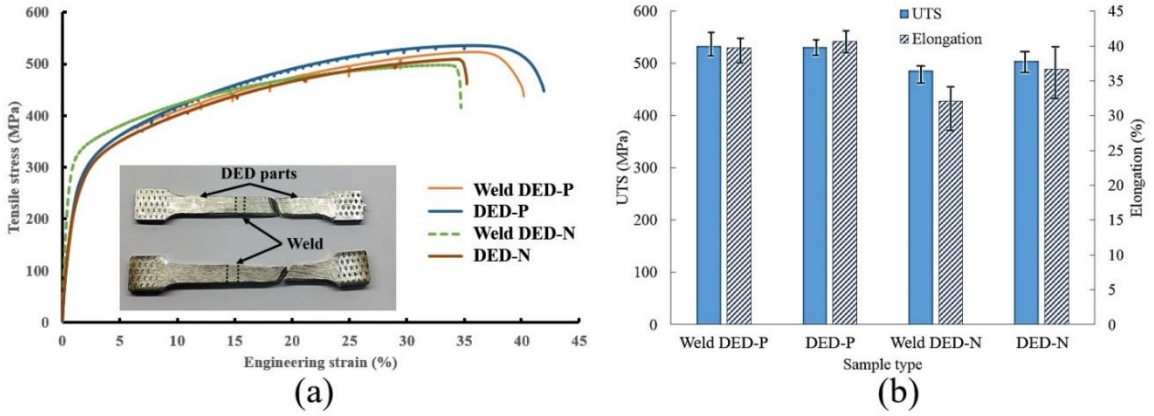

Figure 3.7 Tensile test results for DED and welded DED specimens (a) typical stress-strain curves of different specimens along with broken tensile specimens (b) the average UTS and elongation values of all tested specimens.

Fig. 3.8(a and b) show the SEM fracture surfaces of the Weld DED-N and Weld DED-P coupons, respectively. The orientation of fracture surface was about 45° to the specimen axis that is evidence of ductile fracture (see also Fig. 3.7(a)). At the higher magnifications (Fig. 3.8(c and d)), fine and uniform dimples were predominantly observed, indicating the failure of samples in a ductile manner. Moreover, some torn belts in the fracture surface associated with columnar dendritic structure were observed.

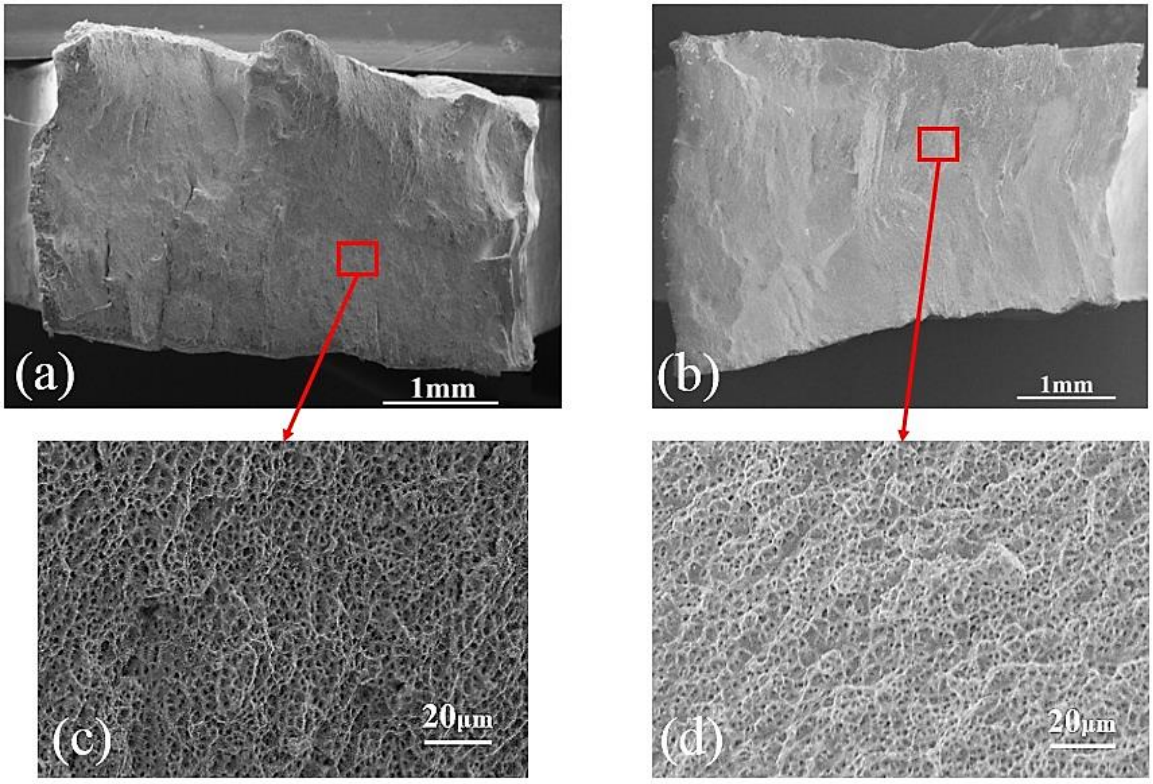

Figure 3.8 Typical tensile fracture surfaces (a) Weld DED-N specimen (b) Weld DED-P specimen (c and d) dimples in the fracture surfaces showing the ductile fracture.

3.3.3 Microhardness

Vickers microhardness measurements were performed across the fusion zone as depicted in Fig. 3.9. No significant difference between microhardness of the fusion zone and DED parts was observed. The average microhardness values for the fusion zone and DED parts were about 247 HV and 242 HV, respectively. The hardness is a result of grain size, meaning that finer microstructure results in higher microhardness [26]. The grain boundaries act as barrier for dislocations and eventually smaller grain size would have higher microhardness [26]. Owing to the identical grain morphology, as discussed earlier,

and close values of grain size between the DED and weld zone, a uniform hardness profile across the DED and fusion zone was obtained.

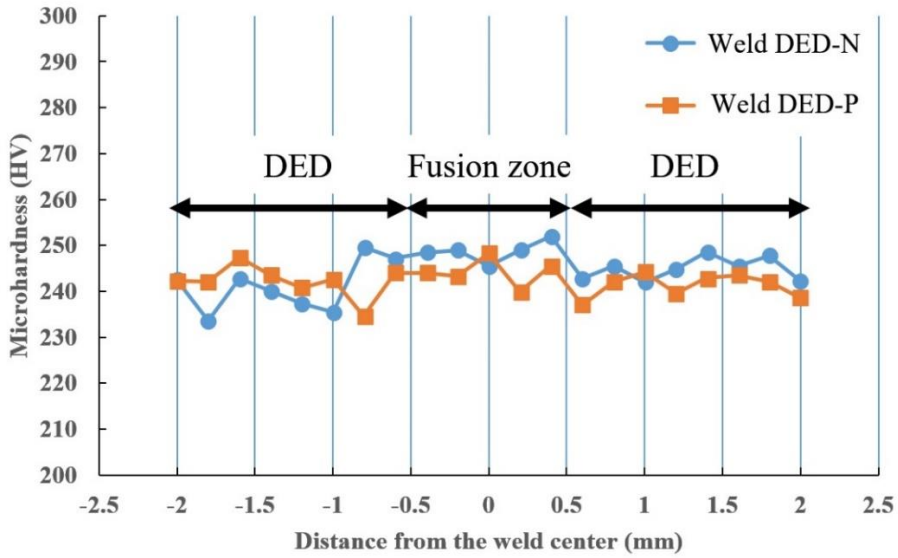

Figure 3.9 Microhardness profiles along the cross-sections of the joints.

3.3.4 Porosity

Fig. 3.10(a and b) illustrate the SEM micrographs of the transverse cross-sections of Weld DED-N and Weld DED-P samples, respectively. A few macropores were observed in both DED and fusion zone. Generally, the main source of pores in the welding process is due to the gas entrapment during the solidification process and are found mostly in spherical shape [27,28]. The pores in the weld zone of DED parts might have two sources of formation. They may either come from the already existing pores in the DED parts that were generated mainly due to the lack-of-fusion or they might be formed in the welding process as a result of gas entrapment. The DED process is prone to the production of microscopic or even macroscopic voids. Upon welding the DED parts, some of the pores may escape from the fusion zone and some of them may combine to form larger pores. The porosity was found to be scattered in the weld zone, similar to the distribution of pores in

DED parts. The size of the porosity was found to be within the range of approximately 18-35 μm in both DED and fusion zone.

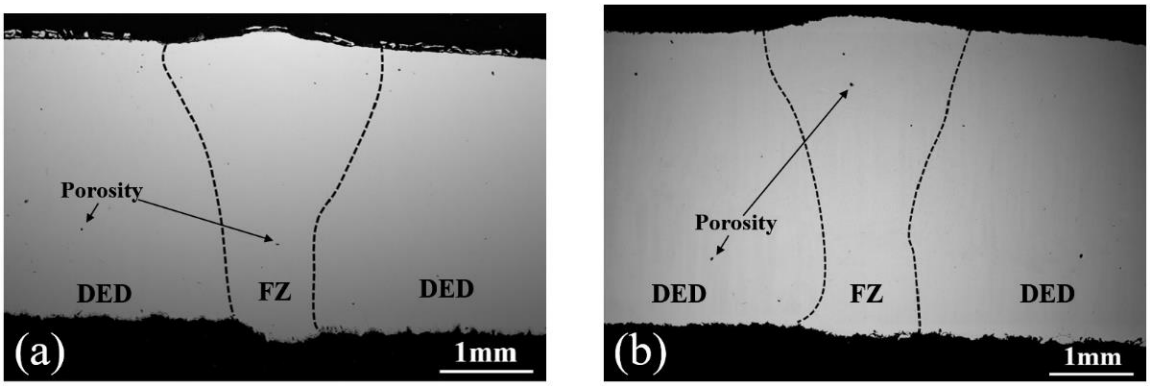

Figure 3.10 Porosity obsereved in (a) Weld DED-N and (b) Weld DED-P coupons.

3.4 A case of fabricating a part with overhang surface

To further verify the capability of the developed process, a part with an overhang section was selected. One of the challenges in the DED process is building complex parts with overhang sections. As an example, a part that was composed of two cones is illustrated in Fig. 3.11(a). It should be noted that the part is a thin-walled structure, where the thickness of wall was equal to the width of a bead. Therefore, a spiral path planning was selected to avoid multiple start-finishes of the process. Building the lower cone is feasible by titling the rotary table for angle α (Fig. 3.11(b)). During the deposition of the lower cone the tilting angle of the rotary table was fixed. Then, after the lower cone was printed, the process should be stopped for repositioning the laser head. The process started deposition of the upper cone on the last layer of the lower cone (Fig. 3.11(c)). Fig. 3.11(b) shows the instance when the lower cone is being printed. Fig. 3.11(c) illustrates an instance when the printing of the upper cone is begun.

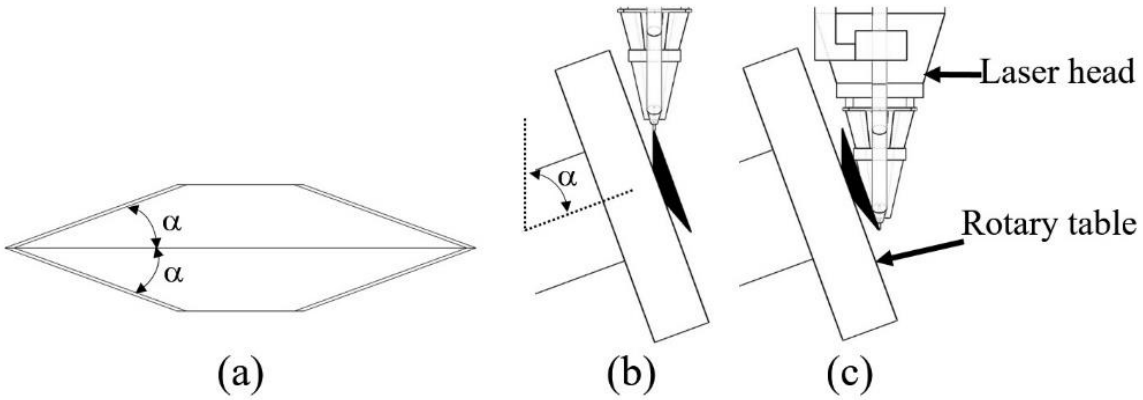

Figure 3.11 (a) A part with overhang sections (b) illustration of kinematic system when the lower cone was printed (c) the occurrence of collision between laser head and lower cone at the instance when the upper cone started to be printed.

However, under the higher values of the angle (α), there might be a collision between the laser head and lower cone as can be seen from Fig. 3.11(c). Thus, it would be impossible to continue printing of the upper overhang section. Moreover, in the position that is shown in Fig 3.11(c), the melt pool was partially supported by the lower cone, leading to instability in the process. Therefore, for such a case, printing the cones individually and then joining them in order to fabricate the whole part could be a solution. Fig. 3.12(a and b) show the lower and upper cones that were printed by the RLW-DED process. Then, an autogenous laser welding process was used to join the cones together on the rotary table (Fig. 3.12(c)). The same process parameters given in Table 3.2 were used to fabricate the slopped component. This part was fabricated to show the application of laser welding in joining the DED parts. The angle (α) in this case was 35°, however this part could be fabricated with higher angles.

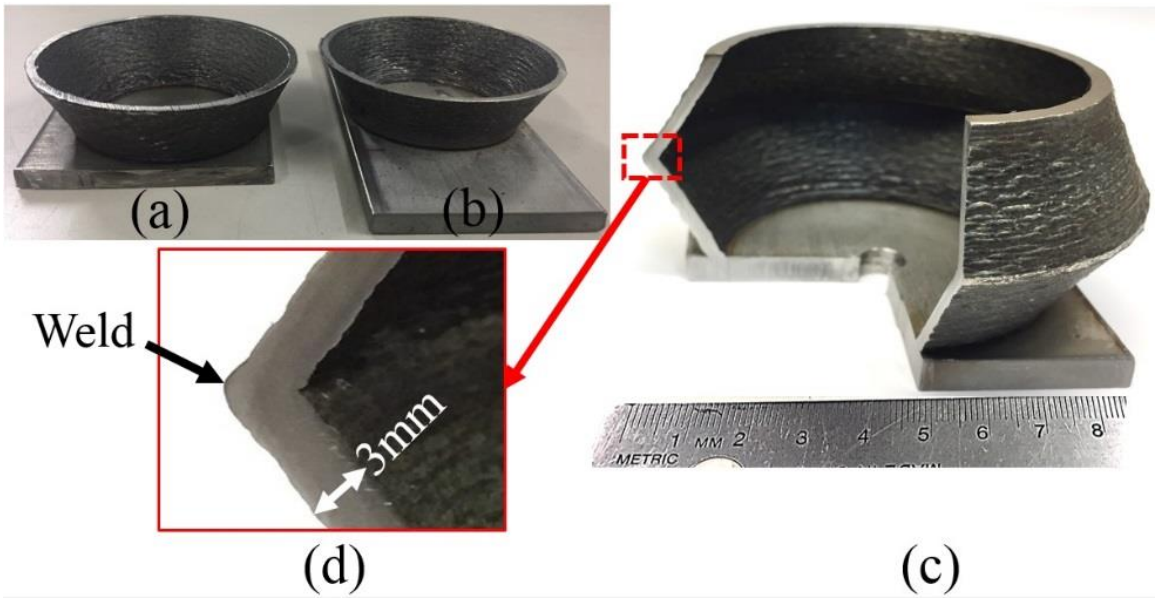

Figure 3.12 (a and b) The lower and upper cones fabricated by RLW-DED (c) the final part after autogenous laser welding of two cones (d) the cross-section of the joint.

Fig. 3.12(d) also demonstrates the cross-section of the weld. A good joint was achieved, confirming the capability of autogenous laser welding in joining thin-walled DED parts. The results proved that the flexibility of the DED process in printing certain complex geometries, especially overhang structures, could be improved.

3.5 Conclusions

In this investigation, an autogenous laser welding process was applied to join the thin-walled elements fabricated by a robotized laser/wire directed energy deposition system. This hybrid system showed the capability of fabricating complex geometries that are difficult to build by using DED process. Microstructural analysis revealed sound welds with almost no HAZ. The dominant grain morphology either in the weld zone or DED parts was found to be columnar dendritic, since autogenous laser welding and laser directed

energy deposition processes have identical solidification behavior. The alloying elements distribution showed a uniform chemical composition in the weld and DED parts with minimum segregation. Also, the mechanical test results showed no significant difference between the welded DED parts and DED parts without weld, in terms of UTS and elongation to failure. However, the tensile specimens taken from normal direction relative to the deposition direction indicated lower UTS and elongation, revealing the anisotropic mechanical behavior of DED parts. Microhardness distribution results showed no noticeable difference between the fusion zone and DED parts, owing to the close size of the grains in these two areas.

Eventually, this study demonstrated that some limitations in DED process such as fabricating parts with overhang sections could be solved by part segmentation and then joining the elements back together by an autogenous laser welding. Therefore, product design in DED process could obtain more flexibility.

REFERENCES

[1] Additive Manufacturing—General Principles—Terminology; ISO/ASTM 52900; International Organization for Standardization: Geneva, Switzerland, 2015.

[2] ASTM F3187-16, Standard Guide for Directed Energy Deposition of Metals, ASTM International, West Conshohocken, PA, 2016, www.astm.org

[3] S.W. Williams, F. Martina, A.C Addison, J. Ding, G. Pardal, P. Colegrove, Wire+ arc additive manufacturing. Materials Science and Technology. 2016 May 2;32 (7):641-7.

[4] T.E. Abioye, D.G. McCartney, A.T. Clare, Laser cladding of Inconel 625 wire for corrosion protection. Journal of Materials Processing Technology. 2015 Mar 1;217:232-40.

[5] E. Brandl, V. Michailov, B. Viehweger, C. Leyens, Deposition of Ti–6Al–4V using laser and wire, part I: Microstructural properties of single beads. Surface and Coatings Technology. 2011 Dec 15;206(6):1120-9.

[6] M. Akbari, Y. Ding, R. Kovacevic. Process Development for a Robotized Laser Wire Additive Manufacturing. In ASME 2017 12th International Manufacturing Science and Engineering Conference collocated with the JSME/ASME 2017 6th International Conference on Materials and Processing 2017 Jun 4 (pp. V002T01A015-V002T01A015). American Society of Mechanical Engineers.

[7] A. Heralić,A.K. Christiansson, M. Ottosson, B. Lennartson, Increased stability in laser metal wire deposition through feedback from optical measurements. Optics and Lasers in Engineering. 2010 Apr 1;48(4):478-85.

[8] M. Akbari, R. Kovacevic, An investigation on mechanical and microstructural properties of 316LSi parts fabricated by a robotized laser/wire direct metal deposition system. Additive Manufacturing. 2018 Oct 1;23:487-97.

[9] J. Zhang, F. Liou. Adaptive slicing for a multi-axis laser aided manufacturing process. Journal of Mechanical Design. 2004 Mar 1;126(2):254-61

[10] R. Dwivedi R, S. Zekovic, R. Kovacevic. A novel approach to fabricate uni-directional and branching slender structures using laser-based direct metal deposition. International Journal of Machine Tools and Manufacture. 2007 Jun 1;47(7-8):1246-56.

[11] G. Casalino, SL. Campanelli, AD. Ludovico. Laser-arc hybrid welding of wrought to selective laser molten stainless steel. The International Journal of Advanced Manufacturing Technology. 2013 Sep 1;68(1-4):209-16.

[12] WW. Wits, JJ. Becker. Laser beam welding of titanium additive manufactured parts. Procedia CIRP. 2015 Jan 1;28:70-5.

[13] VP. Matilainen, J. Pekkarinen, A. Salminen. Weldability of additive manufactured stainless steel. Physics Procedia. 2016 Jan 1;83:808-17.

[14] A. Salminen, E. Westin, E. Lappalainen, A. Unt. Effect of gas shielding and heat input on autogenous welding of duplex stainless steel. ICALEO2012. 2012.

[15] JR. Berretta, W. de Rossi, MD. das Neves, IA. de Almeida, ND. Junior. Pulsed Nd: YAG laser welding of AISI 304 to AISI 420 stainless steels. Optics and Lasers in Engineering. 2007 Sep 1;45(9):960-6.

[16] Oshida Y. Bioscience and bioengineering of titanium materials. Elsevier; 2010 Jul 7.

[17] Standard AS. E8," Standard Test Methods for Tension Testing of Metallic Materials. Annual book of ASTM standards. 2004;3:57-72.

[18] J. Yan, M. Gao, X. Zeng. Study on microstructure and mechanical properties of 304 stainless steel joints by TIG, laser and laser-TIG hybrid welding. Optics and Lasers in Engineering. 2010 Apr 1;48(4):512-7.

[19] CY. Cui, XG. Cui, XD. Ren, TT. Liu, JD. Hu, YM. Wang. Microstructure and microhardness of fiber laser butt welded joint of stainless steel plates. Materials & Design. 2013 Aug 1;49:761-5.

[20] CC. Silva, HC. de Miranda, HB. de Sant'Ana, JP. Farias. Microstructure, hardness and petroleum corrosion evaluation of 316L/AWS E309MoL-16 weld metal. Materials characterization. 2009 Apr 1;60(4):346-52.

[21] CT. Kwok, SL. Fong, FT. Cheng, HC. Man. Pitting and galvanic corrosion behavior of laser-welded stainless steels. Journal of materials processing technology. 2006 Jun 6;176(1-3):168-78.

[22] M. Vilpas. Prediction of microsegregation and pitting corrosion resistance of austenitic stainless steel welds by modelling. Technical Research Centre of Finland; 1999.

[23] PA. Kobryn, EH. Moore, SL. Semiatin. The effect of laser power and traverse speed on microstructure, porosity, and build height in laser-deposited Ti-6Al-4V. Scripta Materialia. 2000 Jul 28;43(4):299-305.

[24] A. Zambon, P. Ferro, F. Bonollo. Microstructural, compositional and residual stress evaluation of CO2 laser welded superaustenitic AISI 904L stainless steel. Materials Science and Engineering: A. 2006 May 25;424(1-2):117-27.

[25] X. Cao, M. Jahazi. Effect of welding speed on butt joint quality of Ti–6Al–4V alloy welded using a high-power Nd: YAG laser. Optics and Lasers in Engineering. 2009 Nov 1;47(11):1231-41.

[26] M. Gao, X. Zeng, J. Yan, Q. Hu. Microstructure characteristics of laser–MIG hybrid welded mild steel. Applied Surface Science. 2008 Jul 15;254(18):5715-21.

[27] N. Seto, S. Katayama, A. Matsunawa. High-speed simultaneous observation of plasma and keyhole behavior during high power CO 2 laser welding: effect of shielding gas on porosity formation. Journal of laser applications. 2000 Dec;12(6):245-50.

[28] S. Katayama, Y. Kobayashi, M. Mizutani, A. Matsunawa. Effect of vacuum on penetration and defects in laser welding. Journal of Laser Applications. 2001 Oct;13(5):187-92.

Chapter 4

CLOSED LOOP CONTROL OF MELT POOL WIDTH IN ROBOTIZED LASER POWDER DIRECTED ENERGY DEPOSITION PROCESS

4.1 Introduction

Additive Manufacturing (AM) is a technique used to fabricate parts in a layer-wise fashion. This technique offers reduction in time and material waste, leading to a decreased buy-to-fly ratio [1]. Different AM techniques that utilize metal as material supply have been researched in recent years. Powder Bed Fusion (PBF) and Directed Energy Deposition (DED) are the two well-recognized sub-categories of metal AM processes [2]. DED is defined as "an additive manufacturing process in which focused thermal energy is used to fuse materials by melting as they are being deposited," according to ISO/ASTM 52900:2015 [3]. In the DED process, metallic powder, wire or a combination of both is fed into the melt pool that is formed by a high energy focused heat source such as electron beam, arc or laser. In contrast, powder bed fusion process works based on a bed of powder that is selectively sintered or melted via laser or electron beam heat source. Using PBF process, building of highly complex parts with internal features is possible. Surface finish of final buildup is also far better than DED process. However, PBF-processed parts are associated with different issues. Fotovvati et al [4], showed the inconsistency and variation of microstructural and mechanical properties of AM Ti-6Al-4V sheets in different

directions and thicknesses. There are numerous advantages of using DED with respect to the PBF process, including an unlimited buildup size, a higher deposition rate, and the possibility to make functionally-graded compositions. DED can repair worn out or damaged high value components, and decrease the need for the support structure. Utilization of sensors for the purpose of monitoring and control is also common in DED, helping the researchers to better understand the physics of the process. Laser powder directed energy deposition or commonly known as LENS® (Laser Engineered Net Shaping) has been extensively used in literature for different applications. For instance, Hu and Kovacevic [5] used multiple powder feeding systems to print functionally-graded structures to tailor the mechanical and compositional properties of the buildup. Wilson et al. [6] showed the effectiveness of the laser powder feeding process to repair and remanufacture a damaged turbine blade. Yaoyu et al. [7] employed a robotized laser-based powder feeding system to print metamaterials with exotic behavior such as negative coefficient of thermal expansion or large Poisson's ratio. Beside the tremendous advantages of laser DED process, one main concern is the energy efficiency of this process. Lin et al. [8] established an empirical model to characterize a relationship between process parameters and energy efficiency and they were able to improve the energy efficiency of DED process significantly.

In robotized laser powder directed energy deposition (RLP-DED), the main processing variables such as powder flow rate, laser power, layer thickness, travel speed, and step-over value affect the quality of deposition and stability of the process. Optimization and tuning of these parameters are necessary prior to the process in order to achieve a consistent and stable process. However, due to the existence of disturbances such

as change in the thermal condition (usually heat transfer mode changes from 3D to 2D conduction during the process) or small change in variables like thermal conductivity (a temperature-dependent material property), powder flow rate or laser power, the implementation of an in-situ sensing and control system is required.

Bi et al. [9] used IR-temperature signals from a single-wall deposition in order to develop a feedback system in the laser powder feeding process. They tried to maintain the melt pool temperature as a control input by adjusting the laser power as a control variable. Their result showed a nearly constant melt pool size and homogeneous microstructure. Farshidianfar et al. [10] developed a feedback proportional integral derivative (PID) controller based on an infrared imaging system in the laser powder cladding process. They were able to maintain the cooling rate by adjusting the travel speed. They showed that the closed loop controller was capable of producing a relatively consistent microstructure. Yaoyu et al. [11] developed a sensing and control system in a robotized laser powder deposition system. They utilized an infrared imaging system to monitor the melt pool size in real time and adjusted the laser power as the control output. They verified the performance of the controller by achieving a uniform cross-sectional thickness of the L-shaped component. Hofman et al. [12] employed a CMOS camera to obtain the width of the melt pool in the laser powder cladding process. They showed that constant laser power can produce higher degrees of dilution and lower value of microhardness in the cladded layer. However, after applying a feedback system, the laser power was reduced by 50%, and hardness and dilution of the clads remained constant. Heralic et al. [13] proposed a controller for the laser wire direct metal deposition system. Their controller was composed of a PI-controller, to maintain the melt pool width, and a feed-forward compensator, to

keep the layer height consistent. The controller was able to increase the stability by minimizing the risk of droplet formation and stubbing.

Most of the studies related to closed loop control of laser directed energy deposition have relied on fixed parameters of the control algorithm. These researches have mainly dealt with a cladding process or a part with a few layers of deposition, where the disturbances such as change in the heat transfer mode or cooling rate had a relatively low effect on the dynamics of the process. Therefore, the control parameters were considered to be fixed values during the process. The existence of disturbances could make the process highly non-linear. For instance, the relation between the melt pool size or temperature and laser power is typically non-linear throughout the entire process, especially when the structure has numerous layers.

In this paper, a monitoring and a PI-closed loop controller based on an infrared imaging system were set up on a robotized laser powder directed energy deposition system. The aim of the work was to investigate the different responses of the non-linear laser deposition process and present a more accurate and reliable controller. The performance of the controller was evaluated by deposition of a 160-layer stainless steel 316L thin wall part. The resulting microstructure was discussed and compared with a deposition under constant laser power.

4.2 Experimental procedure

The block diagram of the RLP-DED system is shown in Fig. 4.1. The system included a 6-axis KUKA robotic arm (KR60) coupled with a two axis positioning table, an IPG 4kW fiber laser with wavelength of 1070 nm, a laser welding head (Precitec YW50),

and an in-house powder feeder [14]. The laser spot was 2 mm in diameter which was achieved at 17 mm defocused distance below the focal point. The image monitoring system was based on a CMOS camera (Prosilica GC 640) that was coaxially mounted on the laser head. The camera worked on a monochrome mode with a resolution of 640x480 pixels, corresponding to a maximum acquisition of 200 frames per second.

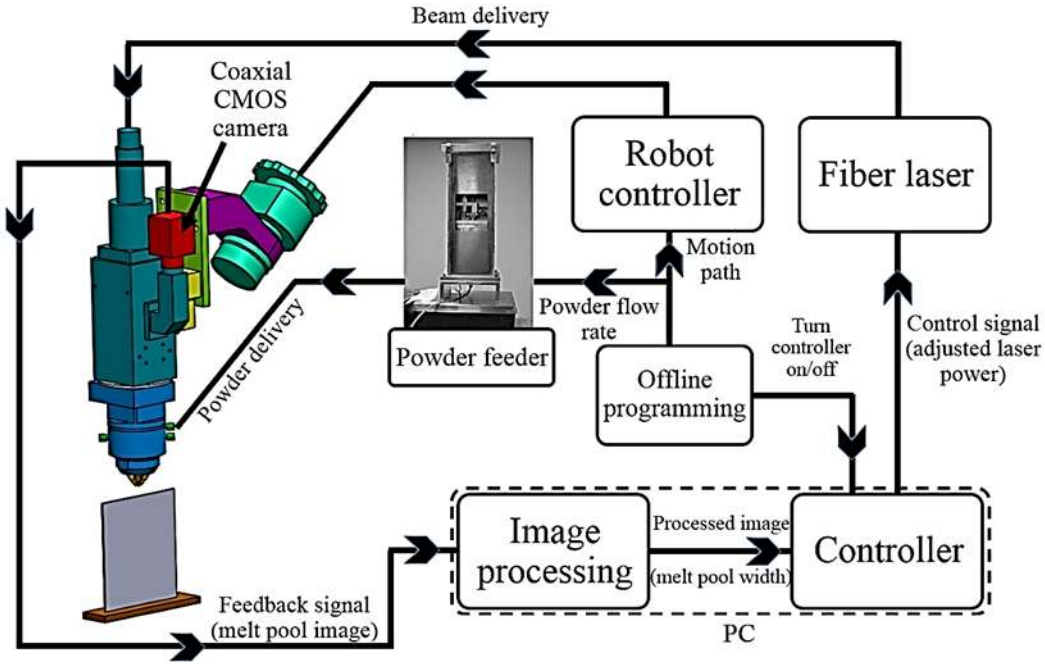

Figure 4.1 Schematic overview of robotized laser powder directed energy deposition equipped with closed loop control system.

The thin wall samples were fabricated by using the optimized process parameters listed in Table 4.1. All parameters except laser power were kept constant during the process for both samples with constant and controlled laser power.

Table 4.1 Process parameters used in this study

Process Parameters	Travel speed (mm/s)	Laser power (W)	Powder feed rate (g/s)	z-increment (mm)	Carrier gas* (l/min)	Shielding gas* (l/min)
Sample with constant laser power	5	600	0.4	0.5	8	15
Sample with controlled laser power	5	Adjustable by controller	0.4	0.5	8	15

*Argon was used as carrier and shielding gas

The depositions were carried out using austenitic Stainless Steel 316L powder produced by North American Hoganas High Alloys LLC. The powder with a particle size of 50-150μm was deposited onto the SS 304L plates as substrate. Chemical composition of the powder and substrate are listed in Table 4.2.

Table 4.2 Chemical composition of powder and substrate

Element (wt.%)	C	Mn	Si	Ni	Mo	Cr	P	S	Fe
Powder (316L)	0.03	1.5	0.8	12	2.50	17	-	-	Bal.
Substrate (304L)	0.03	2	-	8	-	18	0.045	0.03	Bal.

Both samples, i.e. the sample with constant laser power and the sample with controlled laser power, were cross cut and mounted for metallurgical analysis. Then, the samples were sanded and a diamond polishing pad was used to polish them. Afterward, they were chemically etched in HCL:HNO3=3:1 solution for 45 s. A scanning electron microscope (SEM LEO 1450) and an optical microscope (Olympus DP72) were used for microstructural analysis.

4.3 Closed loop control system

4.3.1 Image acquisition and processing

The melt pool width, as the process variable or control variable was monitored and controlled in real-time. The CMOS camera was coaxially mounted on the laser head to take the melt pool images from the top view. All the lights from the melt pool including laser radiation and heat radiation were reflected by a dichroic mirror placed inside the laser head and received by a camera chip. A long-pass infrared filter was utilized in front of the camera to pass the light with a wavelength greater than 700 nm. A notch filter that blocks the laser light with a wavelength of 1070 nm was also used in order to protect the camera from laser damage.

A typical acquired image of the melt pool by a camera equipped with infrared filter is shown in Fig. 4.2(a). Fig. 4.2 shows the steps taken to process the raw image from the camera to eventually measure the width of the melt pool. The image processing code was developed by using the Vision Acquisition Module of Labview platform and was implemented in real time. In the first step, a grey level (0-255) image is captured by the camera (Fig. 4.2(a)). Then, the image is converted to a binary, black-and-white image by applying a user-defined threshold value (Fig. 4.2(b)). The threshold was obtained by depositing several tracks with different widths. Then, the measurement of track widths were taken and compared with the corresponding images to get the appropriate threshold value. The value of the threshold was chosen to be 80 in the experiments. As can be seen from Fig. 4.2(b), the melt pool is surrounded by some flare that is produced by the hot powder particles. The flare can cause considerable noise and error in measuring the melt pool width. Therefore, a low pass FFT (Fast Fourier Transform) filter was employed. The

FFT of an image represents the frequencies of occurrence of pixel intensity variations in the original image (Fig. 4.2(c)). The consistent and smooth intensity variations in the image correspond to low frequencies in the FFT, while the abrupt and fast intensity variations in the image such as flare or noisy pixels at the edge of melt pool correspond to high frequencies in FFT. A low pass filter with a cut-off frequency of 5% is utilized to remove the noise, while preserving the melt pool boundary as shown in Fig. 4.2(d). Frequency of each pixel is set to zero if it is higher than cut-off frequency and remained unchanged if it is less than cut-off frequency. In the next step, the outline of melt pool is extracted (Fig. 4.2(e)). Ultimately, in order to measure the widest section of melt pool, all possible circles that were contained inside the outline were detected (Fig. 4.2(f)). The diameter of the largest circle was recognized as the melt pool width. Therefore, the melt pool width as the control variable was obtainable in real time.

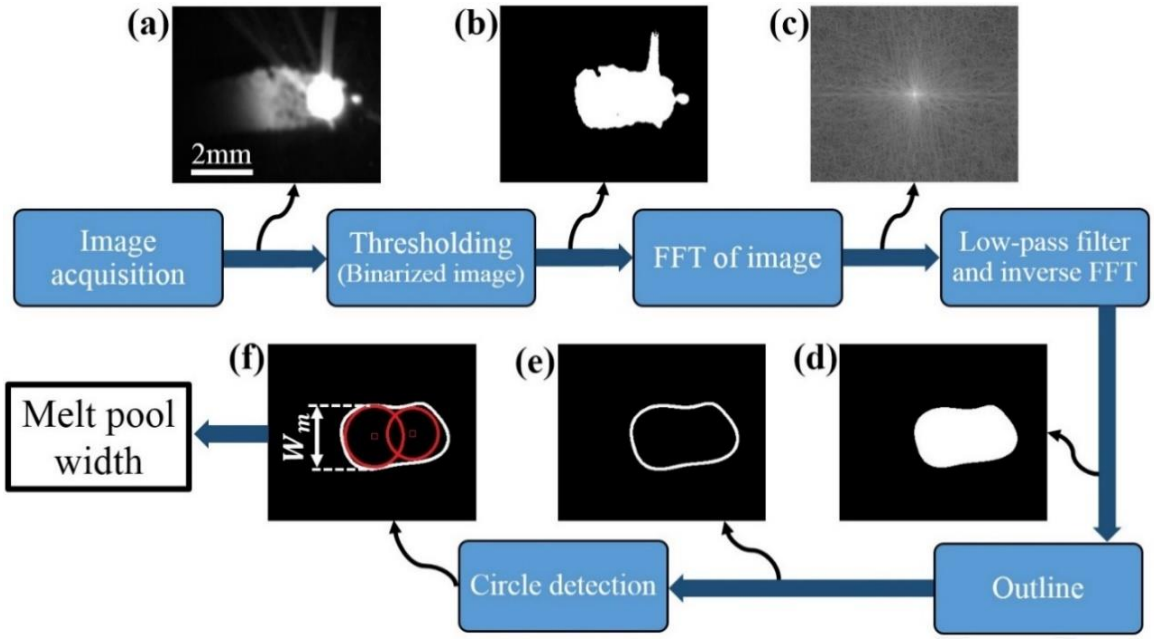

Figure 4.2 Image processing steps to obtain the melt pool width (see text for details).

4.3.2 System identification

The specific energy in the laser powder directed energy deposition process is defined as the energy delivered to the process by the laser [15]:

$$E = \frac{P}{D \times TS} \tag{4.1}$$

where P is the laser power, D is the laser beam diameter, and TS is the travel speed. The specific energy has a key role in determining the melt pool size, melt pool temperature, and morphology of the microstructure. However, given the fixed specific energy does not always guarantee a consistent melt pool size, temperature or homogeneous microstructure. The existence of low frequent disturbances such as change in the heat transfer mode and change in material properties (e.g., thermal conductivity) require that the specific energy be adjusted to ensure the stability of the process and quality of the deposition. In this study, the laser power that had a direct effect on specific energy was selected as an adjustable variable (control output). Melt pool width was chosen to be the control input.

To achieve a robust control system, it was essential to accurately identify and develop the dynamic model of the process. Experiments on the wall sample have shown that the dynamic relation between melt pool width and laser power is non-linear, especially in the initial layers. Therefore, a set of 10 step response tests were performed in the first 10 layers of a 160-layer thin wall part. The results of the tests are shown in Fig. 4.3.

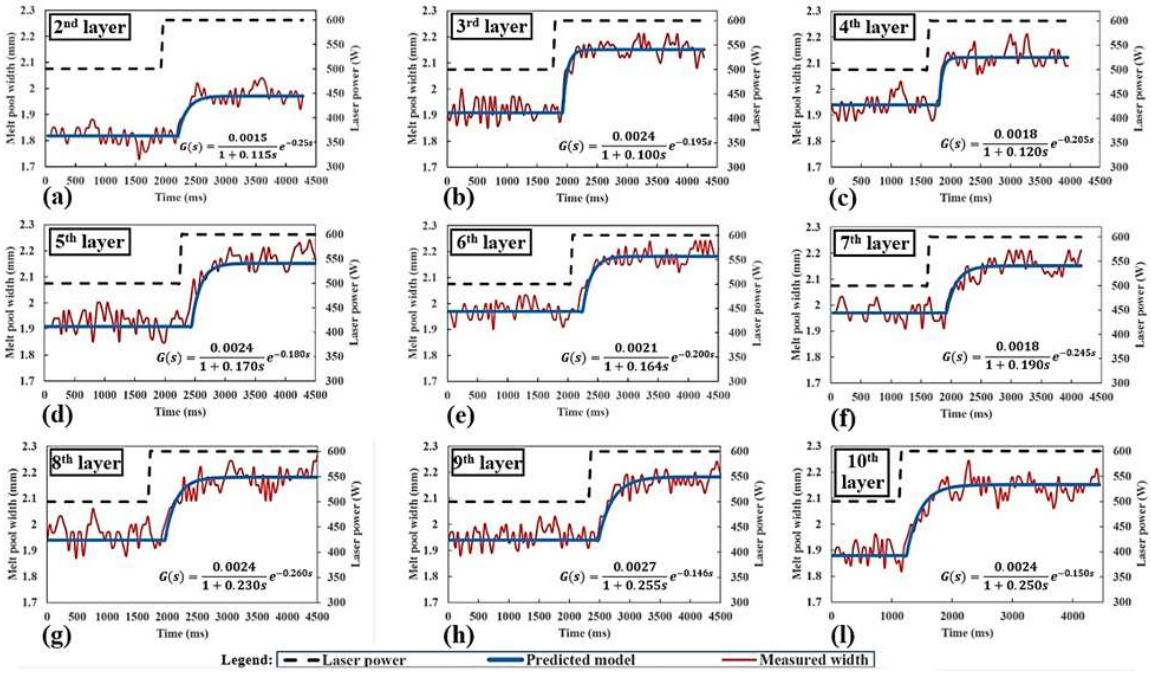

Figure 4.3 The results of step response tests in different layers of a thin wall deposition.

There is no data available for the first layer in Fig. 4.3. This is because the process was unstable in the first layer, due to the extreme heat sink and large fluctuations in measurements, therefore the step tests failed in this layer. In all step tests, the system was perturbed by increasing laser power abruptly from 500W to 600W. This increase caused a change in the melt pool width. As can be seen in all layers, there was no overshoot in the responses. Therefore, the dynamic model of the process can be approximated by a first order with a time delay transfer function as [16]:

$$G(s) = \frac{K}{1+\tau s} e^{-t_d s} \tag{4.2}$$

where K is the static gain, τ is the time constant, and td is the time-delay constant. The static gain is specified as the ratio between variations in the melt pool width (as output signal) and variations in the laser power (as input signal) after the steady state is reached

(K=ΔW/ΔP). The time constant is the time that the response is required to reach 63% of its total change. The time delay or dead time is defined as the time interval where there is no change in the response after the step input is applied. These parameters are graphically illustrated in Fig. 4.4.

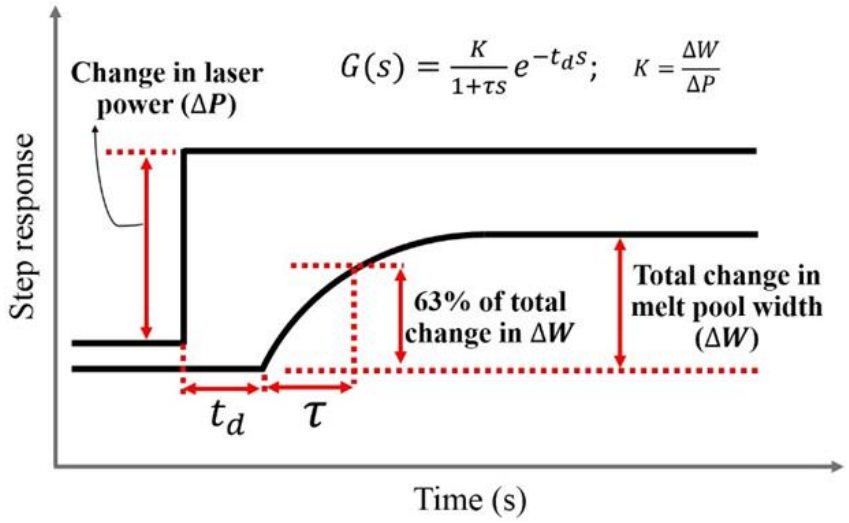

Figure 4.4 Schematic illustration of parameters for first order transfer function.

Experiments in the deposition of thin wall structure showed that the response of the system was almost the same inside each layer. However, from layer to layer, a new dynamic response was observed. This is mainly attributed to the change in thermal condition of the sample after a new layer was deposited. These changes were obvious from the 2nd layer up to the 8th layer, where the transfer function parameters, especially τ, indicated considerable variations. After the 9th layer there was no change in parameters or their changes did not have effect on control parameters. This result will be discussed in detail in the next section. The step response tests were performed around the operating points in which the process was stable. The fluctuations in the melt pool width signal, which can be seen in Fig. 4.3, were inherently associated with the laser-directed energy deposition process. The fluctuation amplitude could be attenuated by applying a digital smoothing

filter. However, the filter could cause a delay in the response of the system. Therefore, use of a digital filter was avoided. The sampling frequency of the process was 30 Hz. This frequency was high enough to control the RLP-DED process with 5 mm/s travel speed.

The raw data from the step response tests was imported into the Pitops software from PiControl Solution LLC to identify the transfer functions of different layers. The corresponding predicted curves of the first order time-delay transfer functions are depicted in the plots of Fig. 4.3. Also, the mathematical representation of the transfer functions are indicated in the plots.

4.3.3 Controller design

The block diagram of the closed loop control system is shown in Fig. 4.5. The melt pool width, as the user-defined set point (WSP), was compared with the measured melt pool width (Wm). The Wm was obtained after the low pass filter was applied on the raw image from the camera. The resulting error, e(t)=WSP-Wm, was sent to the PID controller that was implemented in the Labview platform.

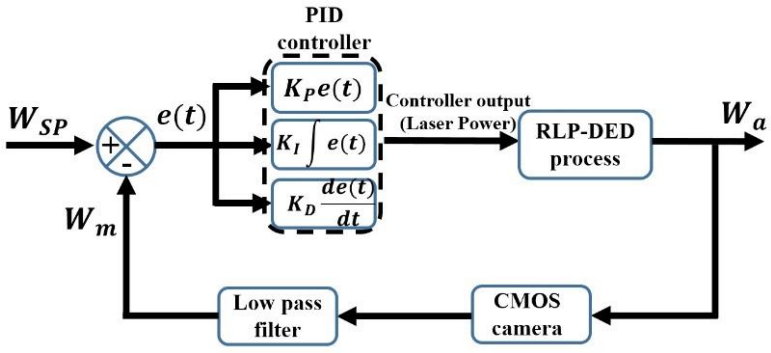

Figure 4.5 The block diagram of the closed loop control system used for RLP-DED process.

The PID controller has been extensively utilized in most industrial control applications due to its simple structure, high stability, and effectiveness. The PID controller

is used when the mathematical model of the process is not available because of the complexity and non-linearity of the system. The output of the controller, i.e. laser power, was sent to the laser power unit. The time continuous equation used for the controller is as follows:

$$u(t) = K_c \left[e(t) + \frac{1}{T_i} \int_0^t e(\tau) d\tau + T_d \frac{de(t)}{dt} \right] \tag{4.3}$$

where u(t) is the controller output sent to the laser unit as a voltage signal, Kc is the proportional gain, Ti is the integral gain, and Td is the derivative gain. In order to digitally implement the time continuous equation in the computer, a finite difference approximation was used:

$$\int_0^t e(\tau) d\tau \approx \sum_{k=1}^{n} T_s e(kT_s) \tag{4.4}$$

$$\frac{de(t)}{dt} \approx \frac{e(nT_s) - e(nT_s - T_s)}{T_s} \tag{4.5}$$

where Ts is the sampling time, which was 0.033 s in this paper, n is the number of discretized steps between zero and time t and k is the step number. Therefore, Eq. (4.3) is discretized as

$$u_n = K_c \left[e_n + \frac{1}{T_i} \sum_{k=1}^{n} T_s e_k + T_d \frac{e_n - e_{n-1}}{T_s} \right] \tag{4.6}$$

The tuning of PID gains were performed with Pitops software. Although, the derivative term could lead to faster response of the system, it caused oscillation and eventual instability in the system. Therefore, a PI algorithm was chosen to control the RLP-DED process in this work, and the derivative term was set at zero. As discussed in the previous section, the transfer function models of the first 10 layers were obtained through

step response tests. Accordingly, the corresponding controller gains were achieved as can be seen in Table 4.3.

Table 4.3 Transfer function parameters and controller gains for different layers

Layer No.	t_d (ms)	K	τ (ms)	K_c	T_i (s)
2	250	0.0015	115	1.40	0.15
3	195	0.0024	100	1.41	0.13
4	205	0.0018	120	1.36	0.18
5	180	0.0024	170	1.42	0.2
6	200	0.0021	164	1.53	0.25
7	245	0.0018	190	1.58	0.25
8	260	0.0024	230	1.61	0.38
9	146	0.0027	255	1.65	0.4
10	150	0.0024	250	1.62	0.4

The data from Table 4.3 reveals that while there was no obvious change in the time delay (td) and process gain (K), there existed a gradual increase in the time constant (τ). An increase in the time constant implies that the process became slower as the layer number increased. The faster response of the system in the bottom layers might be attributed to the fast heat sink into the substrate. Whereas, moving towards the 9th layer, the heat conduction mode changed from 3D to 2D and resulted in slower dynamic response. However, it was observed that after the 8th layer, the time constant remained almost steady at around 250 ms. This result may be related to the heat saturation; hence, heat exchange reached a quasi-steady status [9]. Moreover, there were no obvious variations in td and K beyond the 8th layer up to the last layer of the sample. Therefore, the parameters Kc and Ti were fixed at 1.62 and 0.4, respectively, in the controller for the layers after the 8th. From the control engineering standpoint, an increase in τ moves the closed loop control system in the direction of more stability, allowing a higher proportional gain without the risk of oscillation. This gain can be seen from Table 3 where Kc increased from the 2nd to

8th layer. The integral action (Ti) can be looked upon as the impatience level in the controller. As the process became slower in the upper layers, it allowed the controller to become more impatient; thereby, higher integral actions were achieved. In summary, the non-linear relation between the laser power and melt pool width resulted in different controller gains for a thin wall deposition. To verify the performance of the controller, a 160-layer thin wall part was deposited, which will be discussed in this paper.

4.4 Experimental results and discussion

4.4.1 Performance verification of controller

Fig. 4.6 depicts the closed loop performance of the controller. Two step disturbances in the laser power were applied in the closed loop system. One positive step change varied abruptly from 500W to 600W, and the other negative step change varied from 500W to 400W. As can be observed from Fig. 4.6, the controller successfully responds to the sudden variations in melt pool width and compensates with a change in the laser power until the melt pool reaches the desired set point.

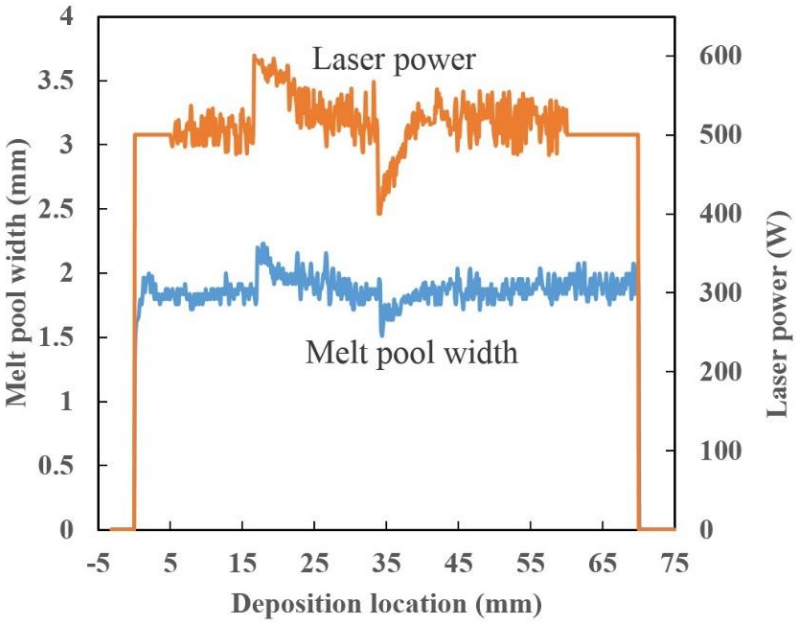

Figure 4.6 Response of the closed loop system to disturbances.

4.4.2 Deposition of thin wall structures with and without control

Fig. 4.7 displays the thin wall samples with 160-layers along with their cross sections at the bottom, middle, and top of the depositions. The sample with a constant laser power (600W) is shown in Fig. 4.7(a). A gradual increase in the melt pool width is clearly seen from bottom towards the top layers. This non-uniform wall thickness was mainly attributed to the change in heat transfer mode. In the first layers, close to substrate, an intense heat sink caused a significant reduction in the melt pool width size. As process continued, the constant laser power led to heat accumulation; thereby, a wider melt pool was achieved progressively.

In current study, all process parameters such as laser power (in the case of sample without control), scanning speed and powder feed rate are set as fixed values and their effects on the process are not studied. However, the effects of these process parameters on melt pool characteristics (size, temperature, geometry, fluid dynamics) and cooling rate are well-investigated in literature [17,18]. In general, by increasing the laser power, the melt pool geometrical features (depth, width, length and surface area) and melt pool temperature increase, while by increasing the scanning speed, all those geometrical features and melt pool temperature decrease.

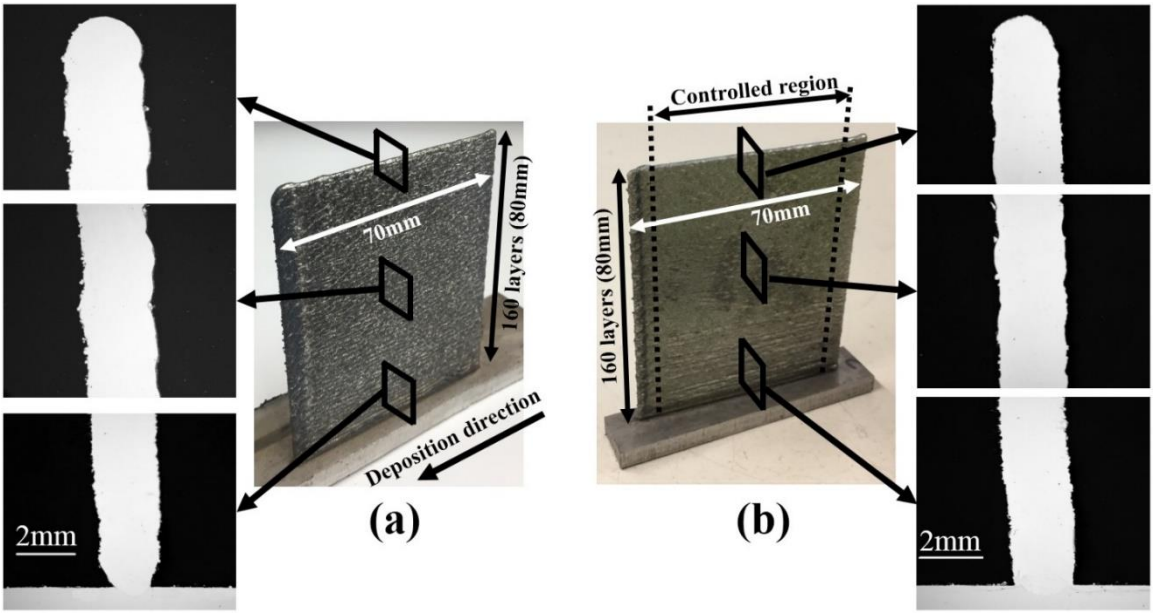

Figure 4.7 The deposited samples along with their micrographs. (a) Sample with constant laser power (b) Sample with controlled laser power.

In order to overcome the issue associated with constant laser power in this study, a PI-controller with adaptable transfer function as discussed in Section 4.3.3 was utilized. Due to the acceleration and deceleration of the robot at the start and end of each bead, larger melt pools were produced in these regions. Therefore, the controller was turned on after 5 mm from the start point, and turned off 10 mm before the end of track. Moreover, since the transfer function was not available in the first layer, the controller was turned off, and a constant laser power (750 W) was set for this layer. It should be noted that to avoid very high or very low laser power, a minimum and maximum range was adjusted. The minimum laser power was set at 350 W and the maximum at 700 W. These limit values for the laser power were obtained by trial and error deposition of tracks with laser powers out of the range. In the tracks deposited with less than 350 W laser power, insufficient heat input into the melt pool caused lack-of-fusion defects and delamination between deposition and substrate. Also, in the tracks with laser power higher than 700 W, excessive energy

caused the re-melting of a large portion of previously deposited layers and consequently an instability led to stop the process. As can be seen from Fig. 4.7(b), the cross sections of the buildup have a uniform thickness throughout the entire build.

The result of real-time measurements of the melt pool width for a constant laser power thin wall is displayed in Fig. 4.8. The significant increase of width in the first several layers and gradual increase in upper layers are also obvious from Fig. 4.8.

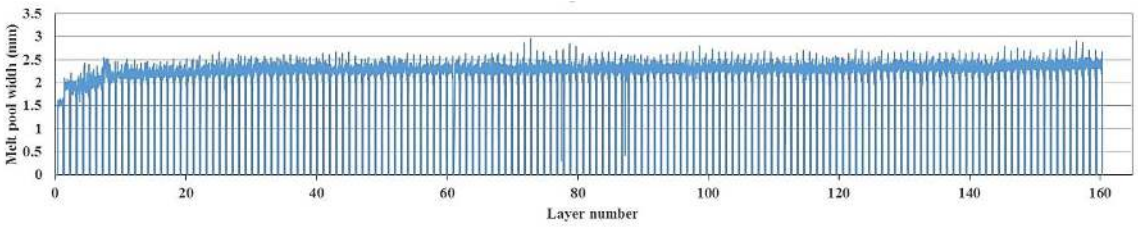

Figure 4.8 Melt pool width as a function of layer numbers for the sample with constant laser power.

Fig. 4.9 shows the variation of the melt pool width for the controlled thin wall. A constant width was observed from real-time measurements. The corresponding adjusted laser power by the controller is also shown in Fig. 4.9(b). It shows that the laser power gradually decreases from 640 W in the 2nd layer to 510 W in the 160th layer.

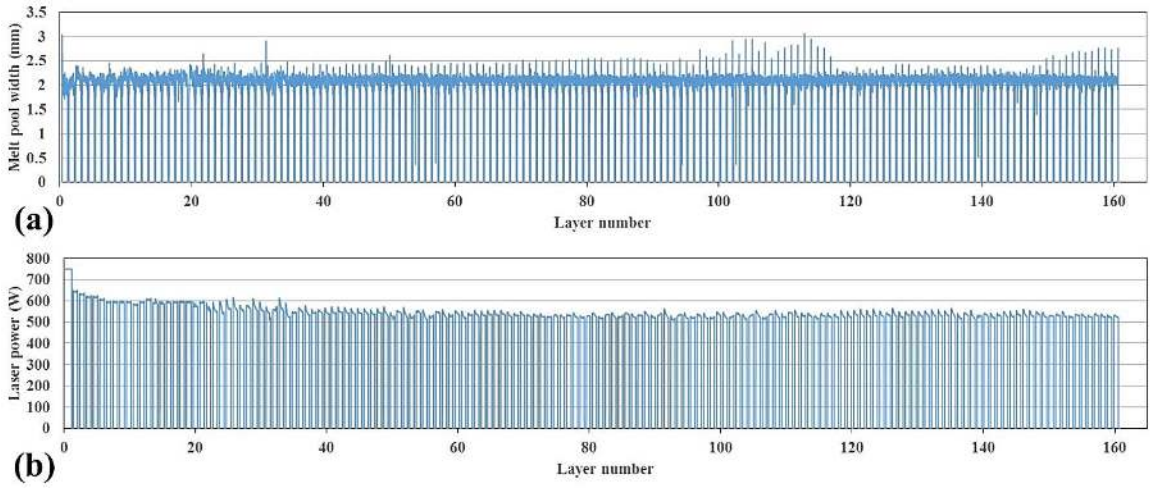

Figure 4.9 (a) The variation of melt pol width and (b) laser power for the controlled sample.

4.4.3 Microstructural analysis

The optical microscope observations revealed no evidence of large porosity, lack of fusion or cracks. The transverse cross sections of both samples, i.e. the sample with constant laser power and the sample with controlled laser power, were examined at the bottom, middle, and top of the depositions as can be seen from Figs. 4.10 and 4.11. The morphology mainly consisted of austenitic cells as the primary phase with ferrite at cell boundaries. The microsegregation at grain boundaries during solidification cause the compositional variations [19] and eventually results in producing darker regions that outline the austenite cells after etching, as can be seen from Figs. 4.10 and 4.11. Figs. 4.10(a) and 4.11(a) illustrate the low magnification of microstructure at the middle of samples. The laser tracks can be clearly observed. The general morphology of the microstructure consisted of a mixture of cellular and columnar dendritic structures. Various portions of cellular, columnar and dendrite structures with secondary arm spacing were observed at different locations of the cross sections. In the microstructure of the sample

with constant laser power, there exists a fine cellular structure in first several layers (Fig. 4.10(b)) that gradually changes to the combination of columnar and cellular structures in the middle (Fig. 4.10(c)). Further, in the top layers the coarse columnar grains are dominant and even dendrites with secondary arm spacing are visible (Fig. 4.10(d)). While, the dendritic grain growth is randomly oriented in some areas, a directional solidification is observed in particular regions (Fig. 4.10(a)). The directional solidification is a common microstructure orientation for laser-processed parts, and is the result of a high solidification rate and temperature gradients [20]. In the case of sample with controlled laser power (Fig. 4.11(b)-(d)), the microstructural observation revealed that the entire structure of sample consisted of only cellular grains, having different cell size in different locations of cross sections. This is attributed to the effect of controller on reducing the heat input and thereby producing relatively finer and more homogenous and uniform microstructure.

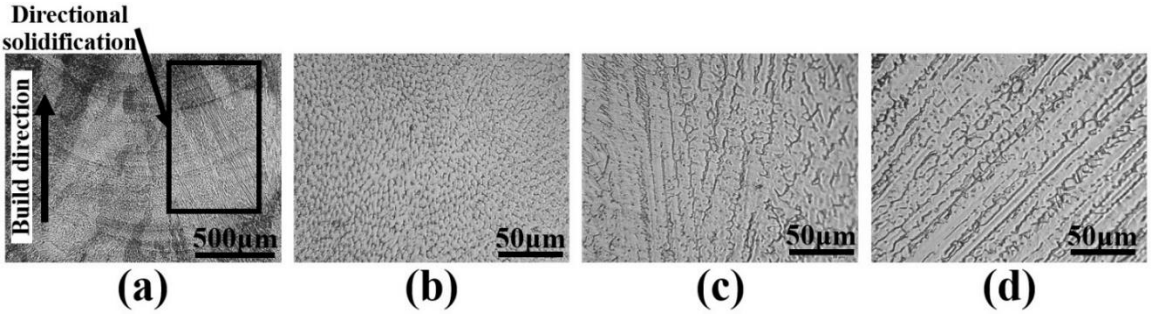

Figure 4.10 Microstructure of 316L sample with constant laser power (a) low magnification of micrograph at middle of sample (b) typical fine cellular structure

at bottom layers (c) cellular and columnar morphology at middle and (d) columnar dendritic structure at top layers.

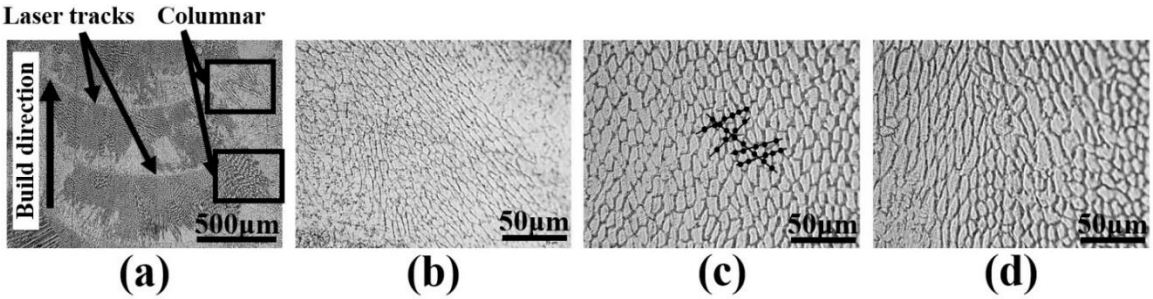

Figure 4.11 Microstructure of 316L sample with controlled laser power (a) low magnification of micrograph at middle of sample. Cellular structures at (b) bottom layers (c) middle and (d) top layers. The method of grain size measurement is shown in (c)

As shown in Fig. 4.12, the solidification map could be used to explain the variations in size and morphology of the microstructure. The two most important factors in describing the solidification map are temperature gradient and solidification rate. The temperature gradient, G, is defined as the tangent of the temperature profile of the melt pool with respect to distance. The solidification rate or growth rate, R, is the travel velocity of the solid/liquid interface. While the product, GR, which is also defined as the cooling rate, governs the size of the solidification structure, the ratio, G/R, is an important factor in determining the morphology preference of solidification (e.g. planar, cellular, columnar or equiaxed dendritic) [21].

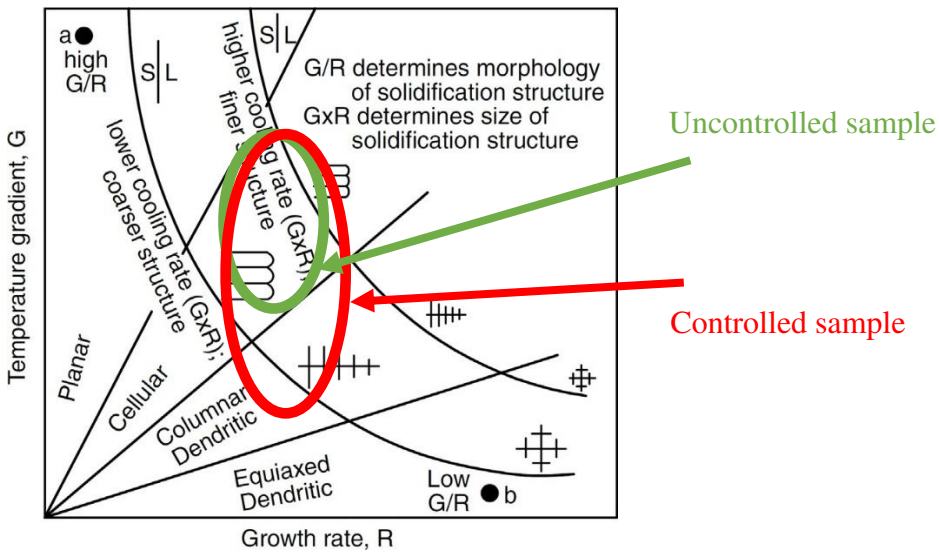

Figure 4.12 Solidification map showing the effect of temperature gradient, G, and growth rate, R, on the morphology and size of solidification microstructure [22].

The temperature of the melt pool progressively increased layer by layer due to the decreased heat conduction through the substrate. Moreover, the temperature gradient reduced in the upper layers because of heat accumulation. Therefore, the ratio, G/R, which defines the stability of solidification front, decreased as new layers were deposited [23]. In the case of uncontrolled sample, after certain number of layers the heat saturation happened and a significant decrease in temperature gradient were observed that typically results in larger window in solidification map as shown in Fig. 4.12. In contrast, smaller variation of G in controlled sample resulted in smaller window that can be seen in Fig. 4.12. The variations in G/R determined the morphology preference in the final solidification. That is, the transition from cellular in the first several layers to columnar dendritic in the last layers of the sample with constant laser power (Fig. 4.10). The cooling rate, GR, was also diminished as the layer number increased. The reduction in cooling rate resulted in enlargement of grains; i.e., the increase in cell size from the bottom toward top layers. Therefore, based on the microstructural observations, it can be concluded that the sample

with controlled laser power would have experienced smaller variations in G/R and GR during the solidification.

The grain size was measured across transverse cross sections of both samples, i.e. the sample with constant laser power and the sample with controlled laser power. The measurements were repeated three times in each area in order to increase the accuracy of data. The mean intercept method was utilized to measure the grain size [24]. The average grain size is calculated by dividing the length of set of lines (randomly drawn) by the number of intersected grain boundaries in the optical micrographs. Fig. 4.11(c) shows the schematic sketch for measuring grain size by the mean intercept method. The result of the grain size measurements is displayed in Fig. 4.13(a). The effect of the closed loop control system is obvious in Fig. 4.13. Although there was a slight increase in grain size, the sample with controlled laser power generally showed more homogeneous and relatively finer microstructure than the sample with constant laser power. In order to calculate the cooling rate, a well-known empirical equation that relates the cooling rate, $\dot{T}$, and grain size, λ, for 316 stainless steel was used [25].

$$\lambda = 80\dot{T}^{-0.33} \tag{4.7}$$

Eq. (4.7) could provide an approximation of cooling rates at different locations of buildup. The results are illustrated in Fig. 4.13 (b). In the first 20 layers, the error bar shows a larger variation of cooling rates in each layer. As the process continues, more stability in the system leads to small variations as can be seen in Fig. 4.13(b).

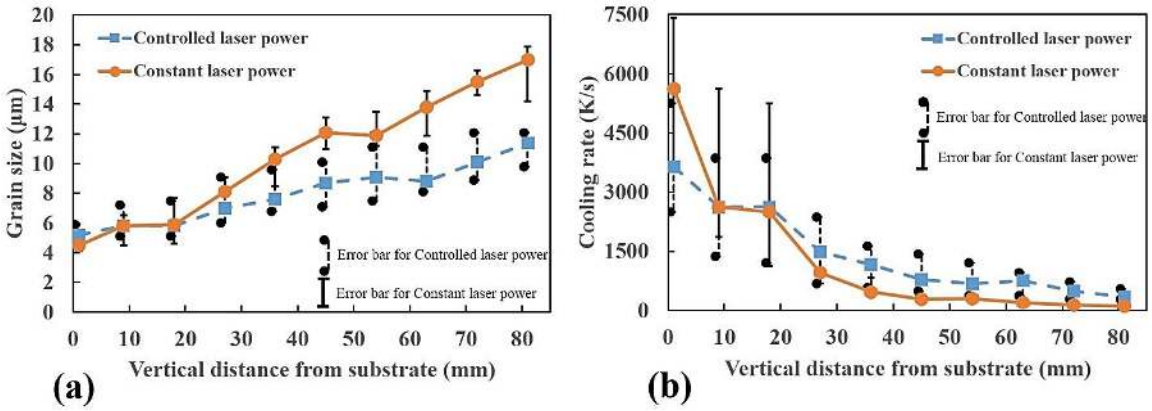

Figure 4.13 The variations in (a) grain size and (b) cooling rate as a function of layer number

Fig. 4.13(b) also demonstrates that the sample with a constant laser power experienced a larger variation in cooling rate across vertical distance as compared to the laser power controlled sample. The result indicated that the closed loop controller in this study that was designed based on the vision system could be used to control, to some extent, the cooling rate and microstructural properties of the buildups. In a similar study by Hofmeister et al. [26], it was found that in the laser powder deposition process, the cooling rate at the liquid/solid interface had a reverse relation to the square of the melt pool length. Therefore, in a feedback control system, the length of the melt pool can be maintained by online adjustment of laser power, leading to a tailored microstructural properties of the buildup. Akbari et al. [27] also used a camera-based monitoring system to measure the melt pool area in the laser wire metal deposition process. They were able to correlate the cooling rate with the melt pool area. They proposed an empirical relation and suggested that the system could be used in the closed loop process in order to adjust the cooling rate in real time.

4.5 Conclusions

A process monitoring control system based on an infrared image of the melt pool was developed and evaluated by deposition of thin wall samples. The main conclusions from the results are as follows:

- The robotized laser power directed energy deposition is a non-linear process. Fixed controller gains could not guarantee a good performance of the control system, because the dynamic response between melt pool width and laser power changed during the first 10 layers of deposition.

- An adaptable PI-controller that corresponded to the different responses of the system in different layers was developed based on the data from step tests.

- The results of real-time measurement showed that by adjusting the laser power the controller could successfully ensure a constant size of melt pool width through the entire build.

- Microstructural analysis revealed a small increase in the grain size of the sample with controlled laser power, while in the process without control, there was a larger increase in grain size and in some locations a cellular-to-columnar dendritic transition occurred in the morphology. Also, a lower variation of cooling rate was achieved when the controller was applied in the system.

REFERENCES

[1] Williams, S.W., Martina, F., Addison, A.C., Ding, J., Pardal, G. and Colegrove, P., 2016. Wire+ arc additive manufacturing. Materials Science and Technology, 32(7), pp.641-647.

[2] Uriondo, A., Esperon-Miguez, M. and Perinpanayagam, S., 2015. The present and future of additive manufacturing in the aerospace sector: A review of important aspects. Proceedings of the Institution of Mechanical Engineers, Part G: Journal of Aerospace Engineering, 229(11), pp.2132-2147.

[3] Additive Manufacturing—General Principles—Terminology; ISO/ASTM 52900; International Organization for Standardization: Geneva, Switzerland, 2015.

[4] Fotovvati, B., Etesami, S.A. and Asadi, E., 2019. Process-property-geometry correlations for additively-manufactured Ti–6Al–4V sheets. Materials Science and Engineering: A.

[5] Hu, D. and Kovacevic, R., 2003. Sensing, modeling and control for laser-based additive manufacturing. International Journal of Machine Tools and Manufacture, 43(1), pp.51-60.

[6] Wilson, J.M., Piya, C., Shin, Y.C., Zhao, F. and Ramani, K., 2014. Remanufacturing of turbine blades by laser direct deposition with its energy and environmental impact analysis. Journal of Cleaner Production, 80, pp.170-178.

[7] Ding, Y., Akbari, M., Gao, X.L., Ai, L. and Kovacevic, R., 2018. 3 Use of Powder-Feed Metal Additive Manufacturing System for Fabricating Metallic Metamaterials. In Manufacturing Techniques for Materials: Engineering and Engineered (pp. 51-65). CRC Press.

[8] Liu, W., Wei, H., Huang, C., Yuan, F. and Zhang, Y., 2019. Energy efficiency evaluation of metal laser direct deposition based on process characteristics and empirical modeling. The International Journal of Advanced Manufacturing Technology, 102(1-4), pp.901-913.

[9] Bi, G., Gasser, A., Wissenbach, K., Drenker, A. and Poprawe, R., 2006. Characterization of the process control for the direct laser metallic powder deposition. Surface and Coatings Technology, 201(6), pp.2676-2683.

[10] Farshidianfar, M.H., Khajepour, A. and Gerlich, A.P., 2016. Effect of real-time cooling rate on microstructure in Laser Additive Manufacturing. Journal of Materials Processing Technology, 231, pp.468-478.

[11] Ding, Y., Warton, J. and Kovacevic, R., 2016. Development of sensing and control system for robotized laser-based direct metal addition system. Additive Manufacturing, 10, pp.24-35.

[12] Hofman, J.T., Pathiraj, B., Van Dijk, J., De Lange, D.F. and Meijer, J., 2012. A camera based feedback control strategy for the laser cladding process. Journal of Materials Processing Technology, 212(11), pp.2455-2462.

[13] Heralić, A., Christiansson, A.K., Ottosson, M. and Lennartson, B., 2010. Increased stability in laser metal wire deposition through feedback from optical measurements. Optics and Lasers in Engineering, 48(4), pp.478-485.

[14] Kovacevic, R., Valant, M.E., (2006), Powder delivery system and method, US7045738B1

[15] Mazumder, J., Schifferer, A. and Choi, J., 1999. Direct materials deposition: designed macro and microstructure. Material Research Innovations, 3(3), pp.118-131.

[16] Goodwin, G.C., Graebe, S.F. and Salgado, M.E., 2001. Control system design. Upper Saddle River, NJ: Prentice Hall.

[17] Fotovvati, B., Wayne, S.F., Lewis, G. and Asadi, E., 2018. A review on melt-pool characteristics in laser welding of metals. Advances in Materials Science and Engineering, 2018.

[18] Liu, Z., Li, T., Ning, F., Cong, W., Kim, H., Jiang, Q. and Zhang, H., 2019. Effects of deposition variables on molten pool temperature during laser engineered net shaping of Inconel 718 superalloy. The International Journal of Advanced Manufacturing Technology, 102(1-4), pp.969-976.

[19] Zheng, B., Zhou, Y., Smugeresky, J.E., Schoenung, J.M. and Lavernia, E.J., 2008. Thermal behavior and microstructure evolution during laser deposition with laser-engineered net shaping: part II. Experimental investigation and discussion. Metallurgical and materials transactions A, 39(9), pp.2237-2245.

[20] Gäumann, M., Henry, S., Cleton, F., Wagniere, J.D. and Kurz, W., 1999. Epitaxial laser metal forming: analysis of microstructure formation. Materials Science and Engineering: A, 271(1-2), pp.232-241.

[21] Kurz, W.1., Giovanola, B. and Trivedi, R., 1986. Theory of microstructural development during rapid solidification. Acta metallurgica, 34(5), pp.823-830.

[22] Kou, S., Welding metallurgy, John Wiley & Sons. 2003

[23] Manvatkar, V., De, A. and DebRoy, T., 2014. Heat transfer and material flow during laser assisted multi-layer additive manufacturing. Journal of Applied Physics, 116(12), p.124905.

[24] ASTM E112-13, Standard Test Methods for Determining Average Grain Size, ASTM International, West Conshohocken, PA, 2013, www.astm.org

[25] Elmer, J.W., Allen, S.M. and Eagar, T.W., 1989. Microstructural development during solidification of stainless steel alloys. Metallurgical transactions A, 20(10), pp.2117-2131.

[26] Hofmeister, W. and Griffith, M., 2001. Solidification in direct metal deposition by LENS processing. Jom, 53(9), pp.30-34.

[27] Akbari, M. and Kovacevic, R., 2018. An investigation on mechanical and microstructural properties of 316LSi parts fabricated by a robotized laser/wire direct metal deposition system. Additive Manufacturing, 23, pp.487-497.

Chapter 5

SUMMARY AND FUTURE WORK

5.1 Summary

In this thesis, several challenges involved in robotized laser directed energy deposition process have been addressed. Inhomogeneity and anisotropy in mechanical and microstructural properties of the as-built parts, existence of defects such as porosity and lack-of-fusion could significantly reduce the quality of parts. Also, the DED is suffering from lack of freedom in designing complex overhang parts. Further, we have shown that in order to make a consistent and homogenous part, a process monitoring and closed loop control is essential to the process. Based on the obtained results the following conclusions can be made:

1- In order to characterize the mechanical and microstructural properties of 316LSi parts, two coupon types, thin-walled and block, were considered. It was found that columnar dendritic was the dominant grain morphology in microstructure of both coupons. The shorter inter-layer time interval in thin-walled coupon caused a decrease in cooling rate, resulting in a coarser grain size and lower UTS. It was also found that the size of the grains were increased from bottom to top of each layer due to an increase in the cooling rates. Block sample showed relatively finer and more uniform microstructure because of the more uniform thermal history. Further,

an empirical relationship correlating the cooling rate to the melt pool area was established. The relation suggested that cooling rate inversely scales with the power of 4 of melt pool area in both coupon types. That is, by applying a real-time monitoring of melt pool and a closed loop control system, one can control the solidification microstructure of the buildup. In addition, the tensile results indicated that the samples parallel to the deposition direction had higher UTS and elongation to failure in both coupon types compared to those in normal direction. The results of micro-hardness test also showed the higher values for block coupon. The porosity analysis also revealed that the main source of imperfection was lack-of-fusion existing mostly in the first layers of deposition.

2- In order to increase the flexibility of DED process to be able to fabricate overhang sections, an autogenous laser welding was applied to join the thin-walled DED elements. This hybrid system showed the capability of fabricating complex geometries that are difficult to build by using DED process. Microstructural analysis revealed sound welds with almost no HAZ. The dominant grain morphology either in the weld zone or DED parts was found to be columnar dendritic, since autogenous laser welding and laser directed energy deposition processes have identical solidification behavior. The alloying elements distribution showed a uniform chemical composition in the weld and DED parts with minimum segregation. Also, the mechanical test results showed no significant difference between the welded DED parts and DED parts without weld, in terms of UTS and elongation to failure. However, the tensile specimens taken from normal direction relative to the deposition direction indicated lower UTS and elongation, revealing

the anisotropic mechanical behavior of DED parts. Micro-hardness distribution results showed no noticeable difference between the fusion zone and DED parts, owing to the close size of the grains in these two areas. Eventually, this study demonstrated that some limitations in DED process such as fabricating parts with overhang sections could be solved by part segmentation and then joining the elements back together by an autogenous laser welding. Therefore, product design in DED process could obtain more flexibility.

3- As there always exists the disturbances such as change in heat conduction mode in the laser DED process, applying a process monitoring and closed loop system is essential in real-time. A monitoring control system based on infrared image of melt pool was developed for laser powder DED process. Two types of thin wall samples, with and without control system, were fabricated. Generally, it was found that the robotized laser power directed energy deposition is a non-linear process. Fixed controller gains could not guarantee a good performance of the control system, because the dynamic response between melt pool width and laser power changed during the first 10 layers of deposition of thin wall sample. An adaptable PI-controller that corresponded to the different responses of the system in different layers was developed based on the data from step tests. The results of real-time measurement showed that by adjusting the laser power, the controller could successfully ensure a constant size of melt pool width through the entire build. Moreover, microstructural analysis revealed a small increase in the grain size of the sample with controlled laser power, while in the process without control, there was a larger increase in grain size and in some locations a cellular-to-columnar dendritic

transition occurred in the morphology. Also, a lower variation of cooling rate was achieved when the controller was applied in the system

5.2 Future work

The followings are the suggestions as the future works:

- Fabrication of large structure parts by using robotized laser wire DED process. Heat accumulation, residual stress and distortion, and generation of geometrical and dimensional error between buildup and pre-defined path planning are the issues associated with large scale printing. Addressing these issues are necessary for laser DED process.
- Utilization of both wire and powder feedstock simultaneously in robotized laser DED process in order to fabricate compositionally graded materials and also to increase the wear and corrosion resistance of the clad layers. Cored wire could be also used in laser DED process. Cored wire contains additive elements. These elements could be alloying elements to produce coating with high alloying level and/or hard particles, such as WC to produce wear-resistant coatings.

5.3 Publications

[1] **Akbari, Meysam**, and Radovan Kovacevic. "Closed loop control of melt pool width in robotized laser powder–directed energy deposition process." The International Journal of Advanced Manufacturing Technology (2019): 1-12.

[2] **Akbari, Meysam,** and Radovan Kovacevic. "Joining of elements fabricated by a robotized laser/wire directed energy deposition process by using an autogenous laser welding." The International Journal of Advanced Manufacturing Technology 100.9-12 (2019): 2971-2980.

[3] **Akbari, Meysam**, and Radovan Kovacevic. "An investigation on mechanical and microstructural properties of 316LSi parts fabricated by a robotized laser/wire direct metal deposition system." Additive Manufacturing 23 (2018): 487-497.

[4] **Akbari, Meysam**, Yaoyu Ding, and Radovan Kovacevic. "Process development for a robotized laser wire additive manufacturing." ASME 2017 12th International Manufacturing Science and Engineering Conference collocated with the JSME/ASME 2017 6th International Conference on Materials and Processing. American Society of Mechanical Engineers, 2017.

[5] Ding, Yaoyu, **Meysam Akbari**, and Radovan Kovacevic. "Process planning for laser wire-feed metal additive manufacturing system." The International Journal of Advanced Manufacturing Technology 95.1-4 (2018): 355-365.

[6] Ding, Yaoyu, **Meysam Akbari**, Xin-Lin Gao, Li Ai, and Radovan Kovacevic. "3 Use of Powder-Feed Metal Additive Manufacturing System for Fabricating Metallic

Metamaterials." Manufacturing Techniques for Materials: Engineering and Engineered. CRC Press, 2018. 51-65.